

**MICRO/NANO TECHNOLOGIES FOR ACHIEVING SUSTAINABLE  
MICROBIAL ELECTROCHEMICAL CELL SYSTEMS**

A Dissertation

by

**CELAL ERBAY**

Submitted to the Office of Graduate and Professional Studies of  
Texas A&M University  
in partial fulfillment of the requirements for the degree of

**DOCTOR OF PHILOSOPHY**

Chair of Committee,	Arum Han
Committee Members,	Choongho Yu
	Edgar Sanchez-Sinencio
	Jim Ji
Head of Department,	Miroslav M. Begovic

August 2016

Major Subject: Electrical Engineering

Copyright 2016 Celal Erbay

## ABSTRACT

Microbial electrochemical cell systems (MECSs), such as microbial fuel cells (MFCs) and microbial electrolysis cells (MECs), are promising clean and renewable energy sources. MFCs employ exoelectrogenic bacteria to convert organic matter in wastewater into electricity, and biogas (hydrogen, methane) is generated from organic matter by applying electricity in MECs. This emerging technology requires better performance by decreasing the material cost to bring it into practical application. Therefore, the main focuses of this research are fabricating nanomaterial based anode to improve the power production and developing micro devices to analyze real-time performance of MECSs.

Physical and electrochemical interactions between microbes and anode are critical to performance. Systematic studies on how different lengths, packing densities, and surface conditions of carbon nanotubes (CNTs) affect MFC power output revealed that long and loosely packed CNTs without any amorphous carbon show the highest power production performance. Furthermore, fabricated 3D sponges composed of interconnected CNTs showed better performance compared to commercially available carbon felt anode.

Due to the configuration, monitoring of biofilm development is hard in macro-sized MFCs. Microfluidic laminar flow MFC with interdigitated anode was fabricated to monitor the real-time optical and electrochemical activity of *Shewanella oneidensis* MR-1 *in situ*. Power density and impedance were measured to understand the relation between biofilm development and power production of biofilm over time.

Expensive and labor intensive equipment such as gas chromatography is commonly used to analyze the biogas produced in MECs. A ZnO nanowires based gas sensor was fabricated to measure H<sub>2</sub> concentration in real-time without using any other expensive equipment.

Low power and low voltage output of MFCs do not allow them to power most electrical applications. Proposed power management systems (PMSs) can overcome this limitation by boosting the MFC output voltage and managing the power for maximum efficiency, regardless of the power and voltage fluctuations from MFCs over time.

Overall, the limitations of the MECSs technology have been identified and possible solutions have been proposed to improve the overall performance of this sustainable renewable energy source.

*To my parents, my grandparents, my wife and my daughter Zahide Hanife  
for their endless love, support, patience and encouragement*

## ACKNOWLEDGEMENTS

First and foremost, I would like to express my sincerest gratitude to my advisor, Dr. Arum Han. This thesis would not have been possible without his continual support, considerable guidance, insight, and encouragement, which not only helped me to finish the doctoral study, but also will benefit my professional development.

I gratefully acknowledge the Ministry of National Education of the Republic of Turkey for financial support.

My sincere thanks to Dr. Choongho Yu and Dr. Edgar Sanchez-Sinencio and their lab members for their great guidance and tremendous help during several stages of this research. I would like to thank Dr. Jim Ji for serving on my committee and for his helpful comments.

I would like to acknowledge all group members in the NanoBio Systems lab for their help. I especially thank Dr. Huijie Hou for the initial studies on the microbial fuel cells.

I am grateful to have wonderful friends: Dr. Ali Riza Ekti, Abdulkadir Bostanci, Sinan Yigit, Osman Safa Ciftci, Dr. Sungman Kim, Fatih Ayyildiz, and any others I did not list. Thank you for all the great memories and amazing friendships.

Most importantly, I would like to thank my family. I could not ask for a better family and thank them for their unconditional love and endless support. My parents have always been a guiding and inspirational influence on me. Thank you for being there whenever I needed it, and even when I thought I didn't need it. I would especially like to

acknowledge and give thanks for the support and patience of my wife, Michelle. No matter if I had a difficult day, I only need to get home to see your smile so that all problems go away. I love you so much my beloved daughter.

## TABLE OF CONTENTS

	Page
ABSTRACT .....	ii
DEDICATION .....	iv
ACKNOWLEDGEMENTS .....	v
TABLE OF CONTENTS .....	vii
LIST OF FIGURES.....	x
LIST OF TABLES .....	xv
1. INTRODUCTION.....	1
1.1. Global water and energy demand.....	1
1.2. Bioenergy .....	2
2. MICROBIAL ELECTROCHEMICAL CELL SYSTEMS.....	3
2.1. History .....	3
2.2. Components and materials .....	3
2.2.1. Electron transfer mechanism .....	3
2.2.2. Anode materials.....	4
2.2.3. Cathode materials and electron acceptors .....	5
2.2.4. Membrane.....	6
2.3. Microbial electrochemical cell system design .....	7
2.3.1. Two chamber MFCs .....	7
2.3.2. Single chamber MFCs .....	9
2.3.3. Stacked MFCs .....	9
2.3.4. Micro scale MFCs .....	10
2.4. Application of microbial electrochemical cell system .....	12
2.4.1. Wastewater treatment and energy generation .....	12
2.4.2. Hydrogen production.....	12
2.4.3. Desalination.....	13
2.5. Thesis scope and outline .....	15
3. CONTROL OF GEOMETRICAL PROPERTIES OF CARBON NANOTUBE ELECTRODES TOWARDS HIGH-PERFORMANCE MICROBIAL FUEL CELLS ..	17

3.1. Introduction .....	17
3.2. Experimental .....	19
3.2.1. Synthesis of CNT electrodes .....	19
3.2.2. MFC setup and operation .....	20
3.2.3. Two-chamber MFC (100 mL) construction and operation .....	23
3.3. The properties and the performance of CNT-SS anodes.....	27
3.3.1. Effect of CNT lengths on MFC performance.....	27
3.3.2. Effect of CNT packing density on MFC power .....	30
3.3.3. Effect of amorphous carbon on CNTs.....	32
3.3.4. Long-term performance of L-LD in 100 mL MFC .....	34
3.4. Discussion .....	36
3.5. Conclusion.....	37
4. THREE-DIMENSIONAL POROUS CARBON NANOTUBE SPONGES FOR HIGH PERFORMANCE ANODES OF MICROBIAL FUEL CELLS .....	39
4.1. Introduction .....	39
4.2. Experimental .....	41
4.2.1. Preparation and characterization of CNT sponge electrode .....	41
4.2.2. MFC setup and operation .....	41
4.2.3. Biofilm characterization .....	42
4.3. CNT sponge as the anode in MFC .....	43
4.4. Discussion .....	47
4.5. Conclusion.....	52
5. LAMINAR FLOW MICROFLUIDIC MICROBIAL FUEL CELL FOR OPTICAL AND ELECTROCHEMICAL MONITORING OF <i>SHEWANELLA</i> <i>ONEIDENSIS</i> MR-1 BIOFILM .....	53
5.1. Introduction .....	53
5.2. Materials and methods .....	55
5.2.1. Cell culture .....	55
5.2.2. Laminar flow MFC design .....	56
5.2.3. Device fabrication and assembly.....	58
5.2.4. Inoculation and device operation .....	60
5.2.5. Biofilm imaging .....	60
5.2.6. Impedance measurement .....	62
5.3. Results .....	62
5.3.1. Laminar flow characterization.....	62
5.3.2. Open circuit voltage and power generation from laminar flow MFC .....	65
5.3.3. Biofilm development on anode in laminar flow MFC .....	70
5.3.4. Impedance measurement of biofilm on interdigitated anode .....	72
5.4. Discussion .....	78
5.5. Conclusion.....	81



6. REAL-TIME H <sub>2</sub> /CH <sub>4</sub> MONITORING FROM MICROBIAL ELECTROLYSIS CELL WITH ZNO NANOWIRES BASED GAS SENSOR.....	82
6.1. Motivation .....	82
6.2. Hydrogen sensing mechanism.....	82
6.3. Device fabrication and nanowire alignment.....	83
6.4. Hydrogen gas calibration and measurement from MEC .....	85
6.5. Conclusions and future work.....	89
7. HIGH PERFORMANCE MONOLITHIC POWER MANAGEMENT SYSTEM WITH DYNAMIC MAXIMUM POWER POINT TRACKING FOR MICROBIAL FUEL CELLS.....	90
7.1. Introduction .....	90
7.2. Materials and methods .....	93
7.2.1. Power management system (PMS).....	93
7.2.2. PMS system efficiency .....	93
7.2.3. Using the PMS-controlled MFC to power a wireless temperature sensor .....	94
7.2.4. MFC construction and operation .....	95
7.3. Results .....	97
7.3.1. PMS correctly determines maximum power point (MPP) of the MFC .....	97
7.3.2. Overall system efficiency of the PMS.....	98
7.3.3. Demonstration with wireless sensor applications .....	101
7.4. Discussions.....	103
7.5. Conclusion.....	106
8. OVERALL REVIEW AND CONCLUSIONS .....	108
8.1. Improving MFC performance with CNT modified anodes.....	108
8.2. Real-time biofilm development analytical device.....	109
8.3. Biogas monitoring device.....	109
8.4. Efficient energy harvesting from MFC with PMS .....	110
REFERENCES.....	111
APPENDIX A .....	134
APPENDIX B .....	140
APPENDIX C .....	145

## LIST OF FIGURES

	Page
Figure 2.1. Two chamber MFC including anode and cathode chambers separated by PEM. ....	8
Figure 2.2. Illustration showing the configurations and working principles of a) microbial fuel cell (MFC), b) microbial electrolysis cell (MEC), and c) microbial desalination cell (MDC). ....	14
Figure 2.3. Limitations and proposed solutions on this thesis. ....	16
Figure 3.1. The 24-well MFC array. (a) The anode electrode/chamber layer of the 24-well MFC array loaded with CNT-SS mesh electrodes. (b) Components of the 24-well MFC array device before assembly. (c) The assembled 24-well MFC array was composed of resistors and dip switches to obtain polarization curves from each of the 24 wells. ....	22
Figure 3.2. As-synthesized CNT-SS mesh electrodes: CNTs were directly grown in the radial direction from the cylindrical wires of SS meshes. (a) A bare SS mesh without CNTs for reference. (b) CNTs on a SS mesh partially scratched off to expose both the SS mesh and CNTs to show the physical contacts between them. The average lengths of CNTs for S-LD (c), M-LD (d), and L-LD (e) were respectively short (~8 $\mu\text{m}$ ), intermediate (~13 $\mu\text{m}$ ), and long (~19 $\mu\text{m}$ ). The length of the CNTs were measured based on the size of the open area between the SS mesh wires (see the decreasing rectangular open areas between the mesh wires in (c–e) compared to the bare SS mesh in (a). The holes of the SS mesh in L-LD were almost filled by CNTs, compared to ~38 $\mu\text{m}$ square opening without CNTs in (a). (f) L-LD showing aligned and densely packed CNTs compared to the other CNTs. (g) M-LD-AC showing amorphous carbon layers intentionally deposited to alter the electrical contacts between CNTs and microbes. (h) The diameter of CNTs with amorphous carbon layers in M-LD-AC is larger than that of S-LD shown in the inset of (c). Scale bars of (a) and (c–g) indicate 20 $\mu\text{m}$ ; (b) 2 $\mu\text{m}$ ; and the inset of (c) and (h) 200 nm. ....	26
Figure 3.3. Power performance and CNT-SS mesh electrodes with different CNT lengths after MFC runs. (a) Power densities against current density of S-LD, M-LD, L-LD, and a bare SS mesh elucidate the effect of the CNT length. (b) Illustration of the interactions between microbes and the CNT-SS mesh electrodes. For a bare mesh, the number of microbes responsible for transferring electrons is limited (upper left pane). Even the electrode with relatively short CNTs (lower left pane) has more microbes than the bare SS	

mesh electrode. For the electrode with long CNTs, a large number of microbes can interact with CNTs along the stem of CNTs (right pane). This was confirmed by a SEM (c), showing microbes captured by CNTs like tentacles. A row of CNTs were scratched off along the axis of the mesh wire for visualization. An enlarged view from a different angle (d) shows that microbes were entangled in CNTs, providing excellent conduits for transferring electrons. (e) In comparison to the CNT-SS mesh electrodes, a bare mesh with microbes laying on the surface of the mesh wire is shown. S-LD, M-LD, and L-LD after testing are respectively shown in (f), (g), and (h). The scale bars in (c), (d), and the inset of (e) indicate 2  $\mu\text{m}$  and those in (e-h) indicate 20  $\mu\text{m}$ .....29

Figure 3.4. Characteristics of aligned and densely packed CNT-SS mesh electrode. (a) Microbes are difficult to get into the CNT forest, making microbes sit on the tip of CNTs. (b) A top view of L-HD after testing, showing microbes only on the top surface of the CNT electrode but not inside the CNT forest, as can be seen through the cracks of the biofilm. The scale bar indicates 2  $\mu\text{m}$ . (c) The power density of L-HD in comparison to that of L-LD whose CNT lengths were similar.....31

Figure 3.5. Characteristics of CNT-SS mesh electrode with amorphous carbon coating. (a) The power density of M-LD-AC (amorphous carbon coating layer) in comparison to that of M-LD, whose CNT lengths were similar. (b) Amorphous carbon coating layers were clearly observed from M-LD-AC outside of the CNT. The arrows mark an individual MWCNT. (c) L-LD had only graphitic carbons.....33

Figure 3.6. Long-term performance of L-LD in a two-chamber MFC device (100 mL). (a) Voltage generation over time showing a sharp increase in voltage after acetate inoculation (arrow marks) and short start-up time (4-5 days). (b) Polarization curves of L-LD and bare carbon cloth (control) showing the maximum power densities achieved with wastewater and acetate and the maximum power density generated by the L-LD anode is 7.4 times that of the bare carbon cloth (3360  $\text{mW m}^{-2}$  vs 456  $\text{mW m}^{-2}$ ). (c) Nyquist curves for the microbial fuel cells equipped with the L-LD and bare carbon cloth. Full curves are shown in an inset graph. (d) SEM image of the microbial growth, where cross section of the L-LD after 3 months of operation shows microbial colonization inside of the CNT forest. The scale bar indicates 10  $\mu\text{m}$ . .....35

Figure 4.1. Performance of the SMFCs equipped with different anode electrode materials (CNT sponge and carbon felt). (a) Voltage output over time of the MFCs with a 1  $\text{k}\Omega$  load resistor. Arrows indicate media replenishment. (b) Polarization curve comparing the volumetric power density (based on anode

chamber volume, 0.5 ml) of the MFC with CNT sponge anode compared to that with carbon felt anode. ....	45
Figure 4.2. (a) Performance of the MMFC (20 ml anode chamber volume) with CNT sponge anode operating in batch mode with a 1 k $\Omega$ load resistor. The arrows indicate the replenishment of the media (acetate). (b) Polarization curves of the CNT sponge anode MMFC compared to that of the carbon felt anode MMFC. The volumetric power densities were calculated based on the volume of anode chamber (20 mL). (c, d) SEM images of the biofilm grown on the CNT sponge anode at low and high resolutions. (e, f) SEM images of the biofilm grown on the carbon felt anode at low and high resolutions. ....	46
Figure 4.3. Performance comparison of the CNT sponge anode loaded in MFCs having three different anode chamber volumes. (a) Volumetric power densities normalized to the anode volume (0.3 cm <sup>3</sup> ). (b) Volumetric power densities normalized to the volume of the anode chamber. ....	48
Figure 5.1. Microfluidic laminar flow MFC device specifications. a) Top view of the device. b) Interdigitated anode specifications. c) Cross sectional view of the microfluidic channel. ....	57
Figure 5.2. Microfluidic laminar flow MFC fabrication process. a) Photolithography and etching techniques were employed for fabrication of the gold electrodes. b) The microfluidic channel was fabricated using conventional soft lithography techniques. c) Photographic picture of the assembled device. ....	59
Figure 5.3. Entire experimental setup a) Open circuit measurement b) Impedance measurements. ....	61
Figure 5.4. Diffusion width and Reynolds number values based the different flow rates. ....	64
Figure 5.5. a) Open circuit voltage and b) Power density over time. Arrows indicated the measurement time points. ....	66
Figure 5.6. Power performance of the laminar flow MFC over time. The power density increased slowly until ~60 hours, then it doubled and continue to increase sharply. ....	68
Figure 5.7. Open circuit voltage generation from different resistors at 110 hour. After each change, the voltage production was stable. ....	69

Figure 5.8. a) In situ biofilm development on anode over time. It gets thicker and larger after ~60 hours. b) Flow streams changing by the growth of biofilm in laminar flow MFC. ....	71
Figure 5.9. Electrical equivalent circuit of the biofilm impedance. ....	74
Figure 5.10. a) Impedance values between the frequency range of 100 Hz and 100 kHz. b) Impedance decreases over time by the growth of biofilm on interdigitated anode. ....	75
Figure 5.11. a) Phase values between the frequency range of 100 Hz and 100 kHz. b) Phase decreases over time. ....	76
Figure 5.12. a) Correlation between power density and impedance for different frequencies (5, 10, 25, 50 kHz) b) Correlation between power density and phase for different frequencies. ....	77
Figure 6.1. a) Photolithography and etching processes for fabrication of the gold electrodes. b) Top view of the gas sensor. ....	84
Figure 6.2. Sensor alignment processes. a) 10 $\mu$ L drop was applied, b) DEP method was used for nanowire alignment, c) Annealing process for strong connection between nanowires and gold electrode, d-e) aligned nanowires. ....	86
Figure 6.3. a) Gas calibration chamber. b) Resistor values of nanowires on the sensors with different hydrogen concentration. c) Equation and R-squared values of the sensors on linear trendline. d) Average percentage resistor change of the sensors. ....	87
Figure 6.4. a) Experimental setup, b) Hydrogen production measure by gas chromatography (SRI 8610C). ....	88
Figure 7.1. Proposed PMS for managing MFC power composed of a DC-DC boost converter block and a MPPT block. The circuit is designed by Salvador Carreon from Prof. Edgar Sanchez-Sinencio's research group at Texas A&M University [95]. ....	96
Figure 7.2. (A) Polarization curve obtained from the low-power MFC (LPMFC), showing power output of 328 $\mu$ W and voltage output of 360 mV at MPP. (B) MPP voltage of 360 mV was successfully detected by the PMS when connected to the LPMFC having an open circuit voltage of 720 mV. (C) Polarization curve obtained from high-power MFC (HPMFC), showing power output of 512 $\mu$ W and voltage output of 400 mV at MPP. (D) MPP voltage (400 mV) was detected by the PMS when connected to the HPMFC having an open circuit voltage of 800 mV. ....	99

Figure 7.3. (A) The overall system efficiency of the PMS determined by the ratio of energy of the MFC and the energy stored in the super-capacitor (100 mF) when connected to a high-power MFC. Measurements were taken over the duration of the initial charging of the super-capacitor and periodic operating of the wireless temperature sensor. (B) System efficiency, energy from MFC, and energy stored in the super-capacitor during the initial charging stage of the super-capacitor when connected to a low-power MFC..... 100

Figure 7.4. (A) The MPP voltage detected by the PMS and the super-capacitor voltage being charged to 2.5 V to directly power the wireless temperature sensor, when using the high-power MFC. (B) Wirelessly transmitted temperature data when using the high-power MFC. (C) Using the PMS with the low-power MFC. (D) Wireless temperature result when using the low-power MFC..... 102

## LIST OF TABLES

	Page
Table 1. A list of CNT-SS mesh electrodes developed to understand how different attributes of CNTs affect MFC power performances. ....	25
Table 2. Performance summary of 3D nanomaterial anodes in MFCs. ....	51
Table 3. Performance summary of previously reported laminar flow MFC works. ....	80
Table 4. Comparison of properties and efficiencies of different PMSs. ....	104

# 1. INTRODUCTION

## 1.1. Global water and energy demand

Water and energy are closely interrelated and are basic components of life. Energy and water demand will rise as the population rises. The world's population is estimated to double over the next 40 years and reach nine billion people in 2040. [1] Therefore, it has been pointed as a major challenge to meet people's increasing energy and water demands in the coming decades. Energy demand for all fuels will continually increase through 2040. Global oil, coal, and natural gas demand will grow by around 15, 10, and 47%, respectively. Electricity demand will also continue to increase by more than 70% by 2040. [1]

Water is a very valuable resource that is essential for life, and only 2.5% of the world's water is freshwater; less than 1% of that is accessible. It is mainly used in agriculture (70%), industrial (19%), and municipal (11%) applications. Global water demand is projected to increase 55% by 2050. [2] Water is required in order to produce energy. It is needed for all processes of fossil fuel production, including extraction and transportation. It is also used in thermal power plants (nuclear, solar) for cooling and to generate electricity from hydropower.

The demand for both energy and water will continue to grow, and almost 75% of the fuel will be produced from fossil fuels (oil, coal, and natural gas) by 2040.[1] Therefore, burning fossil fuels will continue to impact the environment, including air and water pollution, public health and global warming emissions. Since renewable energy



resources (wind, solar, hydroelectric, biomass) have less impact on our environment, it is ideal to increase their usage to generate energy.

## **1.2. Bioenergy**

Bioenergy, also called biomass energy, is renewable energy produced from organic matters, including wood, manure, sugarcane, and municipal and industrial waste. Bioenergy power generation increases every year, and three times more will be produced in 2020 compared to 2006. [3] However, biomass conversion—especially into biofuels such as bioethanol and biodiesel—creates environmental problems from plants, similar to burning fossil fuels. Moreover, a critical factor of this process is how it affects the supplies of food (corn and sugarcane are used to produce bioethanol) and water (a high amount of water is required to grow feedstock). Therefore, microbial electrochemical cell system—another form of bioenergy—has developed great interest. It is able to convert organic waste into electricity by using the electrochemical activity of micro-organisms. Furthermore, it has the potential to reduce greenhouse gas emissions, so it is advantageous compared to biomass conversion and burning fossil fuels.

## **2. MICROBIAL ELECTROCHEMICAL CELL SYSTEMS**

### **2.1. History**

The idea of producing electricity from bacteria (*Escherichia coli*) was discovered in 1911 by M. C. Potter.[4] B. Cohen created microbial half fuel cells in 1931 and generated 2 mA by connecting the half cells in series.[5] Bennetto et al. developed the original microbial fuel cell design and also studied to understand electron transfer mechanism.[6, 7] The most important improvement in microbial fuel cell technology was discovered by Kim et al. who developed mediator-less microbial fuel cells by eliminating expensive mediator molecules used to transport electrons to the anode.[8] Electrochemically active bacteria is able to create a biofilm on an anode by enhancing the power production in microbial fuel cells. Currently, researchers focus on optimizing electrode materials, different types of electrochemical cell systems, scaling up, and electron transfer mechanisms in this promising bioenergy technology. Although the idea of energy harvesting from bacteria was started almost 100 years ago, it has just recently begun to bring out its potential.

### **2.2. Components and materials**

#### **2.2.1. Electron transfer mechanism**

Electrochemically active bacteria oxidize organic compounds and transfer electrons to the anode.[9] Two different electron transfer mechanisms were proposed, which are direct and mediated.[10] Direct electron transfer happens through the outer surface of bacteria

membrane and biofilm with conductive pili where they physically adhere to the anode. Such biofilms are permeable and allow the diffusion of reactants and products, which facilitates the transfer of electrons.[11] The second electron transfer mechanism (mediated) works with an electron shuttle, which is produced by bacteria and carries electrons to the anode. Bacteria are known to produce a range of electron-shuttle compounds, such as melanin, phenazines, riboflavins and quinones.[12]

### **2.2.2. Anode materials**

Anode material is an important component for electron transfer from bacteria and conductive biofilm formation, which determines the effectiveness and efficiency of electricity generation. Therefore, it must be highly conductive, biocompatible, chemically stable and non-corrosive.[13] Conventional carbon based materials, including carbon cloth, carbon paper, carbon felt, graphite rod, and reticulated vitreous carbon (RVC), are most commonly used as an anode in MFCs.[14, 15] Carbon paper is fragile and both carbon felt and RVC have high resistance. Even though graphite rod is a hard material that has lower resistance as well as good electrical conductivity, it is difficult to increase the surface area for bacteria to release the electrons. Carbon cloth has an advantage over them with large porosity for microbial growth. Three dimensional (3D) carbon electrodes—in the form of electrospun carbon fiber electrodes [14] or graphite brush [16] electrodes—are also used in MFCs, as their 3D structures can provide large surface areas for microbial attachment. Logan et al in 2007 reported that MFC with a graphite brush anode produced a  $2400 \text{ mW m}^{-2}$ , which was 2.2 fold higher than that of MFC with a carbon cloth anode

(1070 mW m<sup>-2</sup>).[16] Nanomaterials offer exceptionally large surface to volume ratios as well as unique electrochemical properties such as strong charge interactions with organic matter. Recently, various nanomaterials such as metal nanoparticles [17, 18], graphene [19-21], carbon nanotubes (CNTs) [22-27], and polymer composites with embedded nanoscale carbon materials [28-30] have been used as additives to MFC anodes.

### **2.2.3. Cathode materials and electron acceptors**

Platinum-based catalysts have been regarded as optimal for electrochemical reactions because they support the four-electron pathway and display low overpotential. However, the prohibitively high price of platinum prevents their use in large-scale applications.[31, 32] Thus, it is essential to develop low-cost ORR catalysts without sacrificing the performance of Pt-based catalysts. Recently, CNT-hybrid cathodes containing Pt [33, 34], MnO<sub>2</sub> [35] have displayed promising properties such as low cost and improved ORR activities, mainly due to the large surface area and good conductivity of CNTs. Moreover, their high mechanical strength and excellent chemical stability have contributed to the development of durable cathodes.[36]

The electrons released by bacteria move through an external circuit to the cathode where the electron acceptors are reduced.[37] Various electron acceptors such as ferricyanide and permanganate have been used in the cathode to improve the power generation, but they are not considered to be ideal cathode reactants due to their toxicity, non-sustainability, and cost issues.[38] Oxygen is a cost-effective, sustainable, nature-friendly, and scalable electron acceptor for practical applications. However, the slow rate

and high overpotential of the oxygen reduction reaction (ORR) are the two critical issues [39] that limit the performance of MFCs. There are two different chemical pathways (two-electron and four-electron) through which oxygen is reduced to hydrogen peroxide or water. The two-electron pathway exhibits a high overpotential for ORR, which is less efficient than the four-electron pathway normally observed with precious-metal based catalysts.[36, 39, 40]

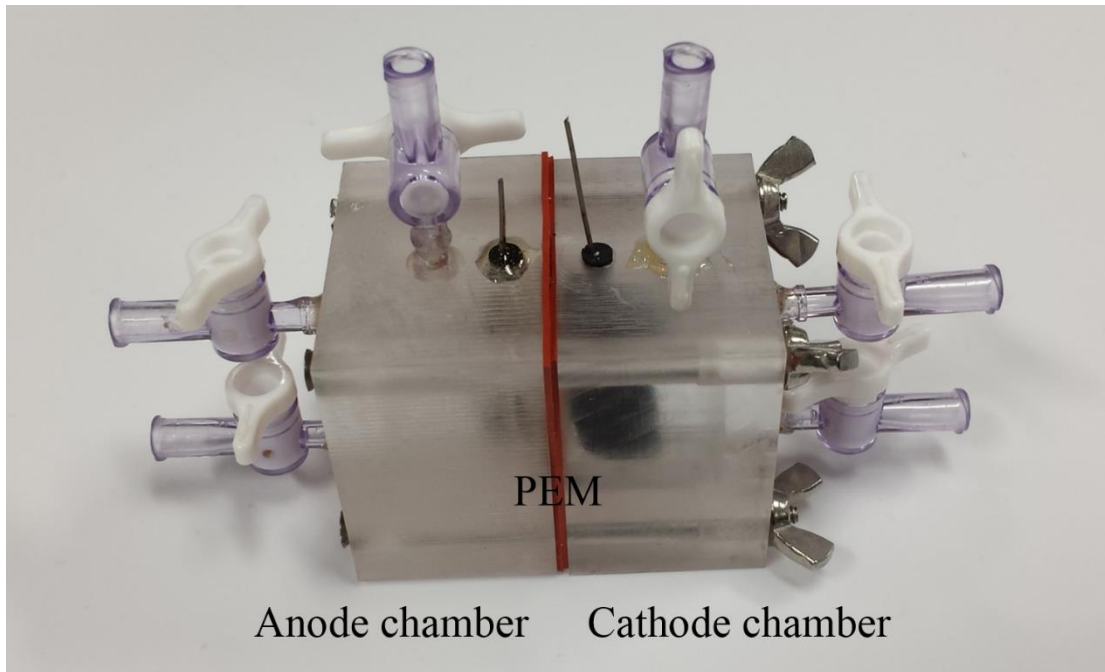
#### **2.2.4. Membrane**

A proton exchange membrane (PEM) is used in two-chamber MFCs to prevent the liquid from mixing and in some single chamber microbial fuel cells (MFCs) to stop leaks.[13] It also helps with passing protons, which are released during the process of organic compounds oxidizing by bacteria, from anode chamber to cathode chamber. Nafion is the most commonly used membrane in MFCs, and more specifically it provides conductivity for protons which directly affect the performance.[41] The main drawback of using nafion is the cost, which is almost half of the total cost. Moreover, high internal resistance results in lower efficiency and performance of MFCs. Ultrex, which is called a cation exchange membrane (CEM), is also sometimes used in MFCs. Although it is cheaper than nafion, the internal resistance is higher. Anion exchange membrane is also another alternative which allows proton transfer via phosphate anions.[42, 43]

## **2.3. Microbial electrochemical cell system design**

### **2.3.1. Two chamber MFCs**

Different design configurations are possible for MFCs. Conventional MFCs consist of two compartments which employ an anode and a cathode separated by an ion exchange membrane such as PEM, CEM, or AEM. The most commonly used two chamber system is an H-type MFC, including two bottles connected by a tube containing PEM to keep liquids separated. The active size of the PEM is limited in an H-type MFC.[44] A cube-shape MFC (Figure 2.1), which is composed from two plastic chambers screwed into each other, can eliminate the limitation of PEM size. The power generation in a two chamber MFC is limited due to high internal resistance. However, they are useful with their simple configuration and they can be conducted to examine the power production from different electrode or separator materials, and microbial communities.



**Figure 2.1.** Two chamber MFC including anode and cathode chambers separated by PEM.

### **2.3.2. Single chamber MFCs**

An anode and one side of a cathode is placed inside of the electrolyte in a single chamber air-cathode MFC where the other side of the cathode is exposed to ambient air.[45] PEM is optional in this configuration. When it exists, it prevents a liquid leak, but power density is limited due to the usage of PEM that increases the internal resistance. Logan and Liu et al found that power density improved almost four times with wastewater when PEM was removed.[45] However, the coulombic efficiency decreased because of oxygen diffusion into electrolytes. Cheng et al used hydrophobic PTFE layers on the air side of the cathode to overcome the diffusion problem. Both power density and coulombic efficiency increased when four PTFE layers were applied on the cathode.[46]

Electricity can be also generated by placing an anode into sediment (in a river, lake, sea) that is rich with bacteria and organic substrates, and connecting it to a cathode in the overlying aerobic water. This kind of configuration is called a sediment microbial fuel cell.[47, 48] It is more practical to self-generate power compared to lab scale MFCs.

### **2.3.3. Stacked MFCs**

Connecting small MFCs to form a larger stack may be more efficient way to scale up MFC systems compared to increasing the size of an individual MFC.[49] Higher voltage or current production can be obtained by stacking MFCs in a series or parallel. Aelterman 2006 et al. stacked six individual MFC units in a series to produce 2 V.[50] Ladezma et al. connected 40 identical 20 mL MFCs together in series and parallel which produced 13.03 V.[51] Wu et al. constructed 72 L stacked MFC which consisted of three anode and



cathode chambers. They obtained the power density of  $\sim 51 \text{ W/m}^3$  in parallel connection of MFCs.[52] Although low voltage limitations can be overcome by connecting MFCs in a series, it is not a long-term solution due to the voltage reversal issue. Since voltage production varies in each MFC, reverse polarity happens after connecting them over a long-term period, and it decreased the overall performance.[53]

#### **2.3.4. Micro scale MFCs**

Micro scale MFCs are advantageous with their easy and flexible configuration for fundamental MFC studies such as screening environmental strains or developing new materials.[23, 27, 54-61] Although they are limited by low power due to their high internal resistance, they offer unique features such as large surface area to volume ratio, short electrode distance and fast response time as well as real time analysis of biofilm under the microscope.[62] Qian et al. developed a two-chamber microfluidic MFC that consisted from  $1.5 \mu\text{L}$  anode and  $4 \mu\text{L}$  cathode chambers. They inoculated the anode chamber with *Shewanella oneidensis* MR1 and power density of  $15 \text{ W/m}^3$  was obtained. Uniform biofilm growth on gold anode was observed which suggested better biofilm/anode interaction in small volume of the chamber.[60] A  $5 \mu\text{L}$  MFC device was also fabricated by employing carbon cloth electrodes to enhance power density ( $62.5 \text{ W/m}^3$ ).[61] Mink et al. developed anode containing carbon nanotubes which provided large surface to volume ratio for microbial interaction in a  $1.25 \mu\text{L}$  chamber to improve the MFC performance.[27] They also developed single chamber air cathode MFCs by eliminating

membrane with the volume of 25  $\mu\text{l}$  and 75  $\mu\text{L}$  which maximum power density of 8  $\text{mW}/\text{m}^2$  and 19  $\text{mW}/\text{m}^2$ , respectively.[58, 59]

Using engineering optimized microbes and improving cultivation practices for microbial species are important strategies for improving MFC performance. Very limited number of microbial strains have been studied for use in MFCs so far. Testing electrochemical and power performance of different microbial strains is not feasible with conventional MFCs. Therefore, microscale microfluidic MFC array which composed from 24 wells was introduced to analyze different bacteria's growth and their power production at the same time. Each well worked as a two-chamber MFC and catholyte was able to be replenished for all of them.[55] Also, air cathode 24-well MFC array was fabricated by eliminating catholyte.[56] In both configuration, the anolyte was lack of replenishment when the substrate was depleted by the bacteria which prevented long term analysis. Therefore, same group designed new version of MFC array which both anolyte and catholyte were replenishable microfluidic access for a more long-term and efficient analysis.[57] MFC array devices were not only used to analyze different bacterial growth performance but also anode materials to show how different carbon nanotube properties affect the anode/biofilm interaction and MFC performance. [23]

## **2.4. Application of microbial electrochemical cell system**

### **2.4.1. Wastewater treatment and energy generation**

Electrochemically active bacteria (EAB) has been shown to be capable of releasing and transferring electrons to electrodes. Microbial fuel cell is the environmentally friendly green technology that converts chemical energy into electrical energy by breaking down organic substrates through the catalytic activation of bacteria.[13] The idea of electricity production by treating free wastewater makes this technology ideal compared to traditional activated sludge systems; however, low voltage and power production as well as the high cost of the materials limited them for practical usage.[13, 63, 64] Finding new electrode materials and removing separators (membrane-less air cathode MFC) have decreased costs and also improved the power generation performance recently. Also, developing power management systems has been proposed as promising technology to increase the voltage.[65] Moreover, inorganic matters that caused environmental pollution such as sulfide and ammonia compounds are rich in brewery, swine, and domestic wastewater.[66-68] They can be removed by bacteria in MFC during wastewater treatment (Figure 2.2.a).

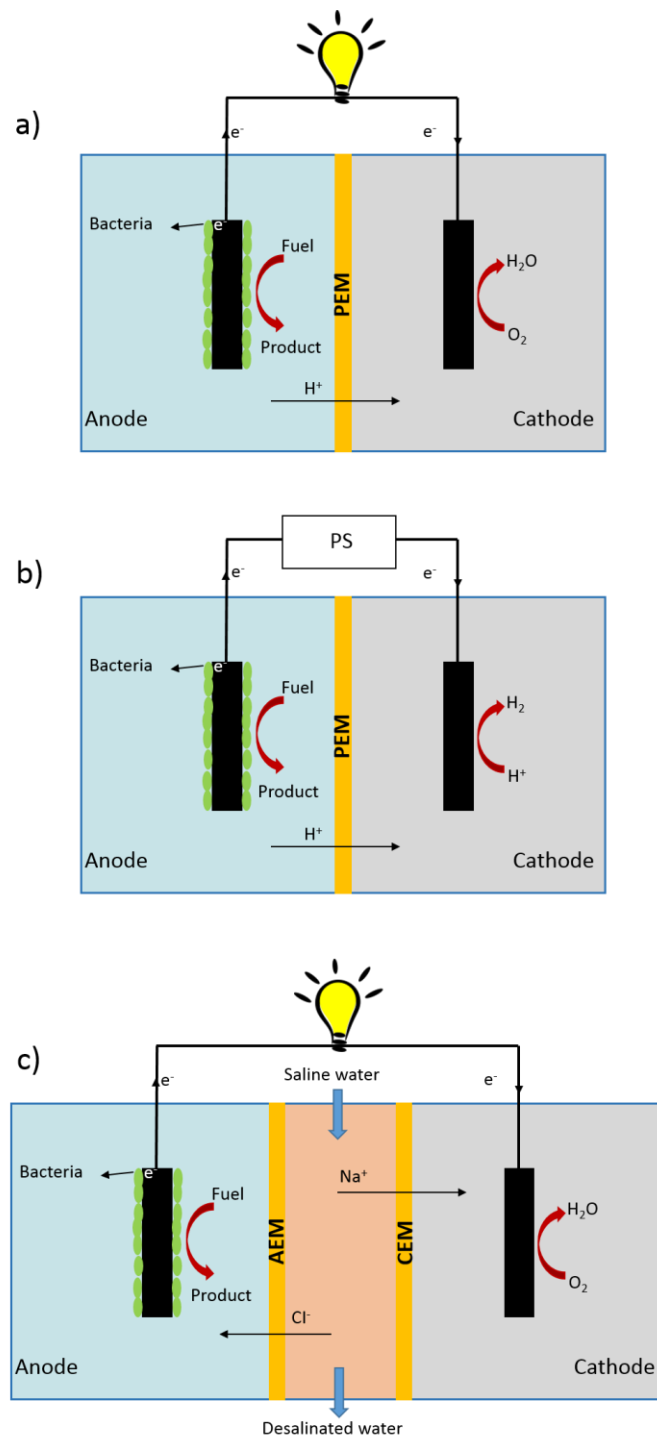
### **2.4.2. Hydrogen production**

Hydrogen has great potential as a renewable energy source since burning hydrogen does not contribute to greenhouse gas emissions that cause global warming. Microbial electrolysis cell (MEC) is a promising new technology for hydrogen production from

bacteria that oxidizes organic substrates and generates CO<sub>2</sub>, electrons and protons in anode.[69-71] Different than MFC, electrons don't flow to the cathode spontaneously. Therefore, MECs require an external power supply to produce hydrogen in the cathode. MECs also require relatively low energy input (0.2–0.8 V) compared to typical water electrolysis (1.23–1.8 V).[72] Therefore, MECs provide an alternative method for hydrogen production. A schematic diagram of a two-chamber MEC is shown in Figure 2.2.b.

#### **2.4.3. Desalination**

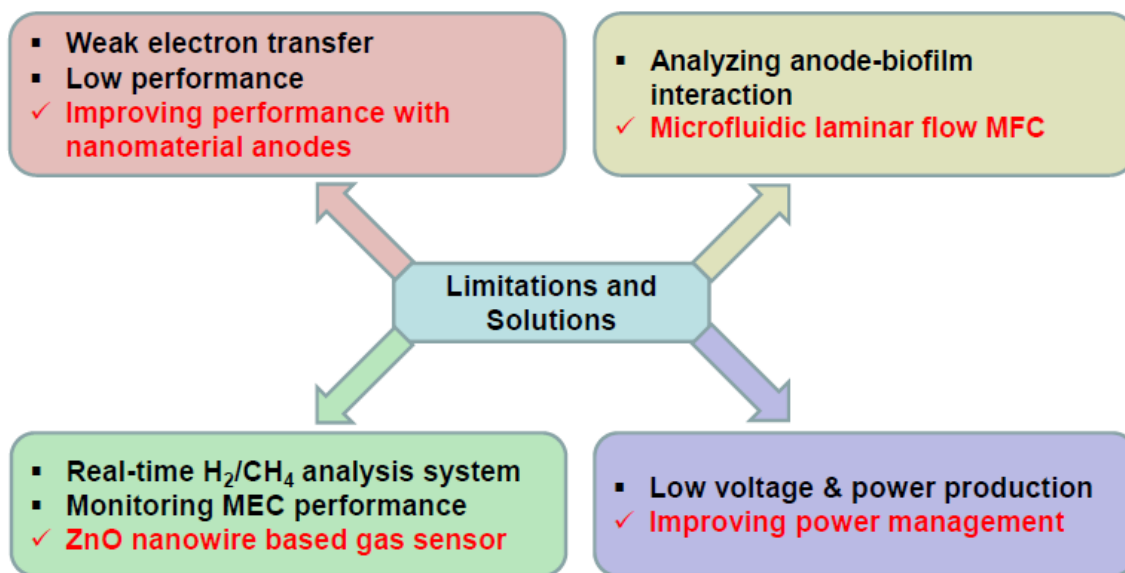
Current seawater desalination technologies such as reverse osmosis, electro-dialysis, and distillation are costly and energy intensive processes.[73] A modified microbial fuel cell configuration, referred to as a microbial desalination cell, can be used to remove dissolved salts from seawater without any external power source. It has an additional chamber filled with seawater between the anode and cathode chambers separated respectively by an anion exchange membrane (AEM) and a cation exchange membrane (CEM). (Figure 2.2.c) AEM keeps positively charged species in the anode chamber. Negatively and positively charged species move from the middle chamber to the anode and cathode, respectively, to maintain the charge balance.[73, 74] In that way, the salt ionic species are removed from the seawater.



**Figure 2.2.** Illustration showing the configurations and working principles of a) microbial fuel cell (MFC), b) microbial electrolysis cell (MEC), and c) microbial desalination cell (MDC).

## **2.5. Thesis scope and outline**

The overall goal of this research is to enhance the microbial electrochemical cell systems by using micro/nano technologies. For this aspect, four different limitations were stated and solutions for the limitations were proposed as shown in Figure 2.3. Weak electron transfer from bacteria to anode results in low performance. Nanomaterial anodes such as CNT grown stainless steel mesh (Chapter 3) and three dimensional CNT sponge (Chapter 4) improve the performance. Analyzing real-time biofilm development and its electrochemical performance is not possible in macro-scale MFCs due to its size. Membrane-less microfluidic laminar flow micro-scale MFC was developed to study SO-MR1 biofilm development and its impedance as well as power production in situ (Chapter 5). Biogas production from MEC can be analyzed through gas chromatography. However, its high cost and labor intensive usage limits them to be practical measurement equipment. Low cost hydrogen gas sensor based on ZnO nanowires was fabricated to measure real-time hydrogen production from MEC (Chapter 6). Low voltage (~400 mV) and power production from MFC limits to run small electronic applications. Power management systems can solve these limitations by boosting low voltage to required voltage and sufficient energy can be stored in super-capacitor which is connected to power management systems. Power management system (Chapter 7) run the wireless temperature sensor which required 2.5 V and ~85 mW to transmit reading data to computer. Lastly, overall research review and conclusions were discussed (Chapter 8).



**Figure 2.3.** Limitations and proposed solutions on this thesis.

### 3. CONTROL OF GEOMETRICAL PROPERTIES OF CARBON NANOTUBE ELECTRODES TOWARDS HIGH-PERFORMANCE MICROBIAL FUEL CELLS\*

#### 3.1. Introduction

Carbon cloth is a common electrode material for MFCs because of its relatively low cost and biocompatibility [8]. Three-dimensional (3D) carbon electrodes, in the form of electrospun carbon fiber electrodes [9] or carbon brush [10] electrodes are also used in MFCs, as their 3D structures can provide large surface areas for microbial attachment. However, these conventional electrodes have limited surface areas when compared to nanomaterial-based electrodes. Nanomaterials offer exceptionally large surface-to-volume ratios as well as unique electrochemical properties such as strong charge interactions with organic matter. Recently, various nanomaterials such as metal nanoparticles [17], carbon nanotubes (CNTs) [26, 27, 75-78], and CNT composites [24, 79] have been used as additives to MFC anodes. For example, multi-wall (MW) CNTs were attached to carbon cloth, papers, or textiles by using simple dipping methods in CNT solutions to increase the electrical conductivity and surface area of electrodes, resulting in 20~150% enhancement in power density [26, 75, 77]. The observed improvements in power generation with these electrodes were thought to arise as a consequence of better

---

\* Reprinted with permission from “Control of geometrical properties of carbon nanotube electrodes towards high-performance microbial fuel cells” by Celal Erbay, Xiong Pu, Woongchul Choi, Mi-Jin Choi, Yeontack Ryu, Huijie Hou, Furong Lin, Paul de Figueiredo, Choongho Yu, Arum Han, 2015. *Journal of Power Sources*, 280, 347-354, Copyright [2015] by Elsevier.



interactions between EABs and electrodes mainly due to improved electrical conductivity and increased surface areas. Nevertheless, the influence of the physical and geometrical properties of these nanomaterials on power output has not been systematically studied. This analysis is of high importance as nanomaterials can have wide varieties of different physical and geometrical properties depending on their synthesis conditions, including those of CNT-based electrodes.

Notwithstanding large surface-to-volume ratios of CNTs, the aforementioned relatively low power improvement is likely to come from non-optimal use of nanomaterials. For instance, the dipping method makes CNTs lie on the surface of carbon cloth rather than stand erect on this substrate [26]. This configuration significantly impairs the full utilization of large surface-to-volume ratio of CNTs. In cases where CNTs are embedded in polymer composites, CNT surfaces are not fully exposed for charge interactions. These electrode designs also require electrically insulating (or poorly conducting) matrices (e.g., polymer binders) and/or surfactants for CNT dispersions. Thus, electrical contacts between CNTs themselves as well as between CNTs and host electrodes are often poor due to the presence of the intervening insulating organic matter.

Here, we attempt to investigate how different lengths, packing densities, and surface conditions of CNTs used as anodes affect MFC power output, as well as propose a CNT-decorated anode configuration that maximizes electron transfer. We expect that this systematic study will result in design principles for developing next-generation nanomaterial electrodes.

## 3.2. Experimental

### 3.2.1. Synthesis of CNT electrodes

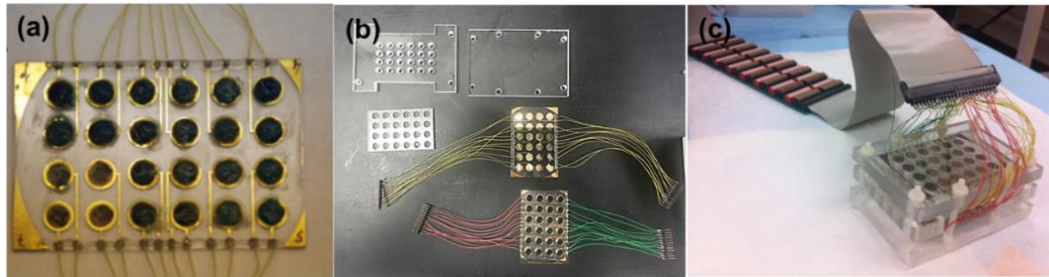
MWCNTs were grown on stainless steel (SS) meshes by using a water-assisted chemical vapor deposition (CVD) method. SS 304 and 316 meshes with 400×400 mesh size (opening width ~38 μm) and ~25 μm wire diameter (McMaster-Carr) were used as base electrodes. In order to control the physical properties of CNTs, different catalyst layers were prepared to have five different physical attributes of CNTs (Table 1). For samples S-LD, M-LD, and L-LD, a 10 nm thick Al film followed by a ~6 nm thick Fe film were deposited on SS 304 meshes by using electron-beam deposition. For sample L-HD, the thickness of Fe film was reduced to ~5 nm. For sample M-LD-AC, the surface of SS 316 meshes was roughened by immersing the meshes in 12.4 M HCl for 30 min. This pretreatment was performed in order to control the morphology of CNTs. For typical CVD processes, the prepared SS meshes (1 inch by 2 inch) were placed at the center of an 1 inch diameter furnace tube. The temperature of a tube furnace was then ramped up to 800 °C in 10 min with 800-sccm dry Ar. The SS mesh was annealed at 800 °C with 80-sccm wet Ar and 100-sccm dry Ar for 10, 16, 20, 13, and 5 min respectively for samples S-LD, M-LD, and L-LD, L-HD, and M-LD-AC. The wet Ar was prepared by passing pure Ar (99.999%) through a bubbler containing deionized water. After the annealing process, 200 sccm H<sub>2</sub> (99.999%) and 100 sccm C<sub>2</sub>H<sub>4</sub> (99.999%) were added to grow CNTs at 800 °C for 30, 30, 60, 30, and 60 min respectively for samples S-LD, M-LD, and L-LD, L-

HD, and M-LD-AC. All CNT anodes were fabricated by Dr. Yu's research group in Materials Science and Engineering department at Texas A&M University [23].

### **3.2.2. MFC setup and operation**

Microfabricated 24-well MFC arrays (Figure 3.1) were used for testing the CNT-SS mesh electrodes in parallel. The MFC arrays with 24 independent cells were developed to compare different microbial electrochemical activities. The device was prepared with at least three replicas for each electrode, and their power densities were averaged with standard deviations. The CNT-SS mesh electrodes were punched and attached to gold-deposited anode-side pads using silver epoxy (MG Chemicals). Platinum-loaded carbon paper ( $0.5 \text{ mg cm}^{-2}$ , ElectroChem, Inc) electrodes were also bonded to the cathode-side pads with the same method. Subsequently, the epoxy was cured in an oven for 15 min at  $60 \text{ }^{\circ}\text{C}$  to maximize its conductivity and bond strength. Figure 3.1.a shows a 24-well anode electrode/chamber layer with the CNT-SS mesh electrodes. The cathode chambers were filled with potassium ferricyanide (100 mM) and the anode chambers were inoculated with *Shewanella Oneidensis* (SO) MR-1. SO MR-1 was used as electrochemically active bacteria after incubation in tryptic soy broth (TSB). Cells were stored in TSB supplemented with 15% glycerol at  $-80 \text{ }^{\circ}\text{C}$ . Cells were streaked onto a TSB agar plate from storage upon use. The resultant colonies was inoculated into 5 ml of TSB liquid medium and then cultured for 48 h at  $30 \text{ }^{\circ}\text{C}$  with agitation (180 rpm). The optical densities ( $\text{OD}_{600}$ ) for SO-MR1 was measured and adjusted to 1.0. Finally, all components (Figure 3.1.b) were assembled into a system (Figure 3.1.c). All parts were sterilized with 70%

ethanol right before assembling the device. The assembled device was connected to a printed circuit board (PCB) that has a series of 8 different resistors for each of the 24 units on the device and controlled by multi-position dip switches (Figure 3.1.c). The switch box module was connected to a digital multimeter through a multiplexer (National Instruments) for continuous voltage measurements across the different resistors monitored via a LabView™ (National Instruments) interface. The measured voltage was converted to current using the Ohm's law, and power output was calculated by multiplying voltage and current. This allowed measurement of power outputs from each of the 24 wells continuously at various load resistances, generating polarization curves for each of the 24 wells as a function of time.



**Figure 3.1.** The 24-well MFC array. (a) The anode electrode/chamber layer of the 24-well MFC array loaded with CNT-SS mesh electrodes. (b) Components of the 24-well MFC array device before assembly. (c) The assembled 24-well MFC array was composed of resistors and dip switches to obtain polarization curves from each of the 24 wells.

### 3.2.3. Two-chamber MFC (100 mL) construction and operation

The two-chamber MFC was constructed from two 50 ml acrylic chambers separated with a proton exchange membrane (PEM) (Nafion 117<sup>TM</sup>, Ion Power Inc.) that was placed between silicon rubber gaskets to prevent liquid leak. The PEM was pretreated by boiling in H<sub>2</sub>O<sub>2</sub> (30%) and deionized (DI) water followed by 0.5 M H<sub>2</sub>SO<sub>4</sub> and DI water, each for 1 hour, and then stored in DI water prior to being used. The L-LD was used as an anode electrode with projected surface area of 1 cm<sup>2</sup>. The cathode (3.5 × 3.5 cm) was carbon cloth that has one side catalyst layer (10wt% Pt/C, 0.5 mg Pt cm<sup>-2</sup>, ElectroChem, Inc). One-way plastic valves (Cole-Parmer) were connected to chambers with epoxy glue to replenish the solution. The anode and the cathode electrodes (1 cm distance) were connected to titanium wire with silver epoxy (MG Chemicals) to provide strong and better connection. The anode chamber was filled with an autoclaved nutrient mineral buffer (NMB, pH 7.0) solution containing: NH<sub>4</sub>Cl (530 mg L<sup>-1</sup>), CaCl<sub>2</sub> (150 mg L<sup>-1</sup>), MgCl<sub>2</sub>·6H<sub>2</sub>O (200 mg L<sup>-1</sup>), NaH<sub>2</sub>PO<sub>4</sub> (6 g L<sup>-1</sup>), KH<sub>2</sub>PO<sub>4</sub> (140 mg L<sup>-1</sup>), CoCl<sub>2</sub>·6H<sub>2</sub>O (2.5 mg L<sup>-1</sup>), NaMoO<sub>3</sub>·2H<sub>2</sub>O (0.05 mg L<sup>-1</sup>), FeCl<sub>2</sub>·4H<sub>2</sub>O (20 mg L<sup>-1</sup>), NiCl<sub>2</sub>·4H<sub>2</sub>O (0.25 mg L<sup>-1</sup>), MnCl<sub>2</sub>·4H<sub>2</sub>O (0.5 mg L<sup>-1</sup>), Na<sub>2</sub>SeO<sub>4</sub> (0.25 mg L<sup>-1</sup>), NaVO<sub>3</sub>·4H<sub>2</sub>O (0.05 mg L<sup>-1</sup>), ZnCl<sub>2</sub> (0.25 mg L<sup>-1</sup>), and CuCl<sub>2</sub> (0.15 mg L<sup>-1</sup>) in deionized water [80]. Anaerobic activated sludge was obtained from Austin Wastewater Plant under an oxygen-free condition at 30 °C and used as the inoculum in the anode chamber with acetate (1 g L<sup>-1</sup>) as an electron donor. Additional acetate (0.5 g for 50 ml anolyte) was fed intermittently when the voltage is ~50 mV (batch-type MFC). Nitrogen was purged after each replenishment for 10 minutes to remove the oxygen from anode chamber. The anolyte were mixed by using a magnetic

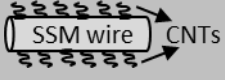
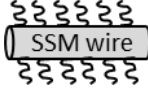
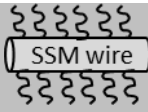

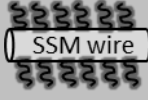
stirrer (400 rpm). The cathode chamber was filled with the ferricyanide solution (100 mM) to minimize the cathode limitation. The anode and cathode were connected with an external resistor (3 k $\Omega$ ), and the voltage across the resistor was monitored. All experiments were conducted at room temperature (~24 °C). The device was connected to a PCB that has a series of different resistors and controlled by multi-position dip switches (Figure 3.1.c). The switch box module was connected to a digital multimeter through a multiplexer (National Instruments) for continuous voltage measurements across the different resistors monitored via a LabView™ (National Instruments) interface. For evaluating power outputs from MFC, the measured voltage was converted to current using the Ohm's law, and power output was calculated based on the equation 3.1 and 3.2:

$$I = V / R \quad (3.1)$$

$$P = I^2 \times R \quad (3.2)$$

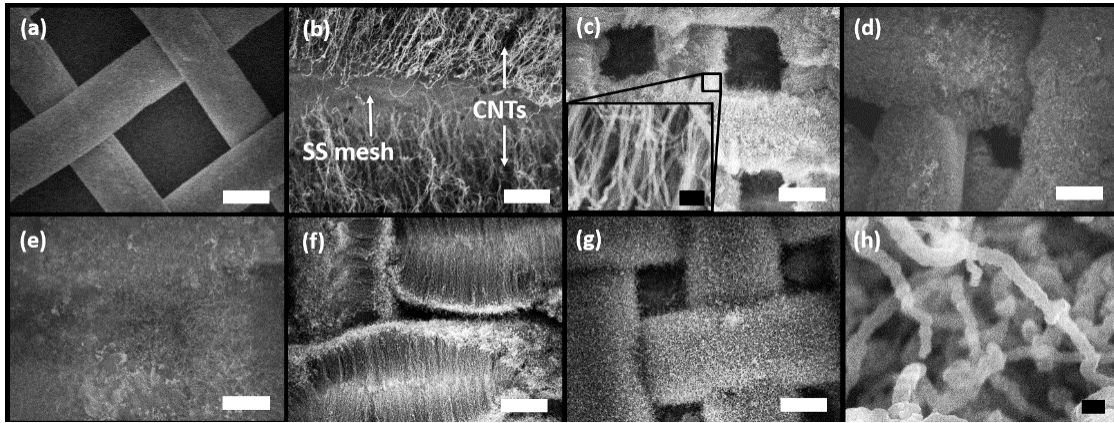
Polarization curve experiment was performed to determine the maximum power production generated from MFC. When the voltage output became stable, polarization curve was obtained by varying the resistance (100  $\Omega$ -20 k $\Omega$ ) between the electrodes.

**Table 1.** A list of CNT-SS mesh electrodes developed to understand how different attributes of CNTs affect MFC power performances.

Sample <sup>a)</sup>	CNT length [ $\mu\text{m}$ ] <sup>b)</sup>	Packing density	Surface condition
S-LD 	~8	Low (loosely packed)	-
M-LD 	~13	Low (loosely packed)	-
L-LD 	~19	Low (loosely packed)	-
L-HD 	~19	High (aligned)	-
M-LD-AC 	~10	Low (loosely packed)	Amorphous carbon layer on CNT surface

<sup>a)</sup> Sample name nomenclature: (length; S = short, M = medium, L = long) - (density; LD = low density (loosely packed), HD = high density and aligned) - (surface condition; none = pure CNT, AC = CNTs covered with amorphous carbon); <sup>b)</sup> CNT lengths were estimated by measuring the straight distance from the surface of mesh wires to the tip of CNTs. Actual lengths of the CNTs are likely to be longer than the numbers shown in this table due to the wavy morphology of CNTs.





**Figure 3.2.** As-synthesized CNT-SS mesh electrodes: CNTs were directly grown in the radial direction from the cylindrical wires of SS meshes. (a) A bare SS mesh without CNTs for reference. (b) CNTs on a SS mesh partially scratched off to expose both the SS mesh and CNTs to show the physical contacts between them. The average lengths of CNTs for S-LD (c), M-LD (d), and L-LD (e) were respectively short ( $\sim 8 \mu\text{m}$ ), intermediate ( $\sim 13 \mu\text{m}$ ), and long ( $\sim 19 \mu\text{m}$ ). The length of the CNTs were measured based on the size of the open area between the SS mesh wires (see the decreasing rectangular open areas between the mesh wires in (c–e) compared to the bare SS mesh in (a). The holes of the SS mesh in L-LD were almost filled by CNTs, compared to  $\sim 38 \mu\text{m}$  square opening without CNTs in (a). (f) L-HD showing aligned and densely packed CNTs compared to the other CNTs. (g) M-LD-AC showing amorphous carbon layers intentionally deposited to alter the electrical contacts between CNTs and microbes. (h) The diameter of CNTs with amorphous carbon layers in M-LD-AC is larger than that of S-LD shown in the inset of (c). Scale bars of (a) and (c–g) indicate  $20 \mu\text{m}$ ; (b)  $2 \mu\text{m}$ ; and the inset of (c) and (h)  $200 \text{nm}$ .

### **3.3. The properties and the performance of CNT-SS anodes**

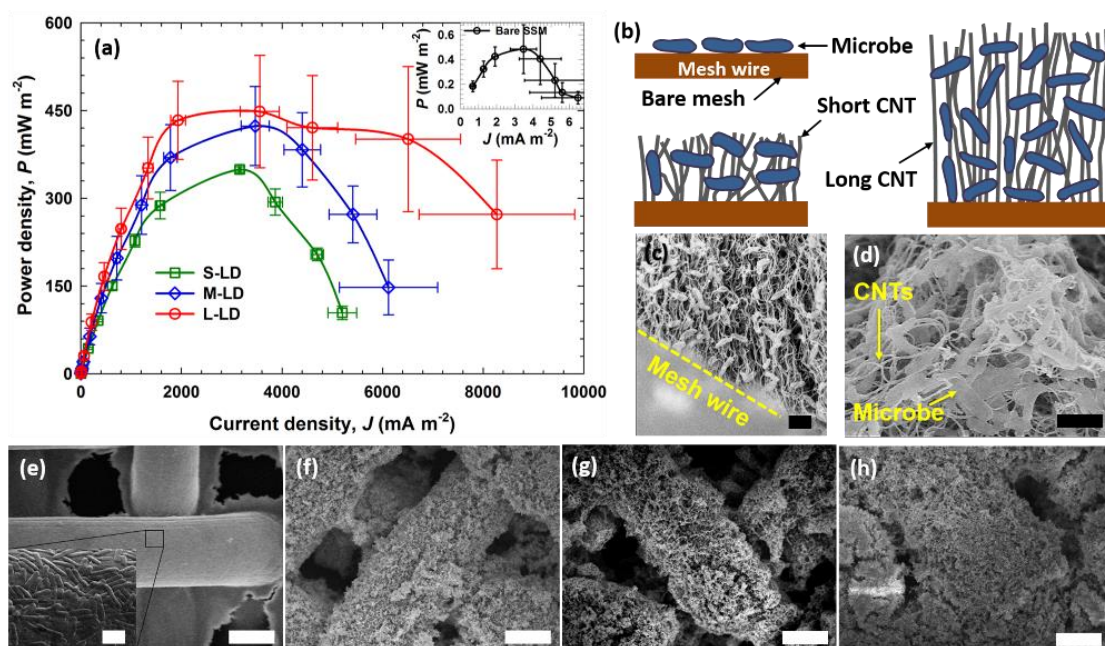
The SS mesh was selected to serve as a backbone of the 3D electrode material. CNTs grown in the radial direction from the wires of the meshes can provide extremely large surface areas and thus have the potential to maximize contact between EABs and the electrodes, facilitating the transfer of electrons from EABs to the anodes. CNTs were directly synthesized on the SS wires to ensure minimal ohmic loss between CNTs and SS meshes compared to attaching CNTs on electrodes with binders as conventionally done. Table 1 lists five different types of CNT SS mesh electrodes developed in this study. Figure 3.2.a shows a bare SS mesh as a reference. Figure 3.2.b shows CNTs grown on a wire of a SS mesh after scratching off a row of CNTs along the axis of the mesh wire, so as to clearly display excellent physical contacts between the SS mesh and CNTs. CNTs of different lengths (8, 13, and 19  $\mu\text{m}$ , Figure 3.2.c, 3.2.d, and 3.2.e, respectively), all being relatively low-density and loosely packed, were synthesized by controlling the catalyst activation time and moisture level.

#### **3.3.1. Effect of CNT lengths on MFC performance**

Comparison of power densities from the electrodes with CNTs of different lengths (Samples S-LD, M-LD, and L-LD) and that from a bare SS mesh (control) showed not only significant improvement, but also significant variations depending on the CNT lengths (Figure 3.3.a). As schematically shown in Figure 3.3.b, with longer CNTs, it is expected that the number of microbes interacting with the CNT electrode increases along the stem of CNTs. Microbial attachment throughout the length of the CNTs like tentacles

capturing microbes was confirmed by SEMs (Figure 3.3.c showing side view; Figure 3.3.d showing top view). On the contrary, only a small number of microbes (cylindrical slender objects shown in the inset of Figure 3.3.e) can be laid on the limited two-dimensional wire surface of a bare SS mesh, resulting in low power output. This reflects the significantly higher (~940% improvement) power density with the longest CNTs (~19  $\mu\text{m}$ ; sample L-LD; ~450  $\text{mW m}^{-2}$  at ~3600  $\text{mA m}^{-2}$ ) compared to that of the bare SS mesh control (~0.48  $\text{mW m}^{-2}$ ).

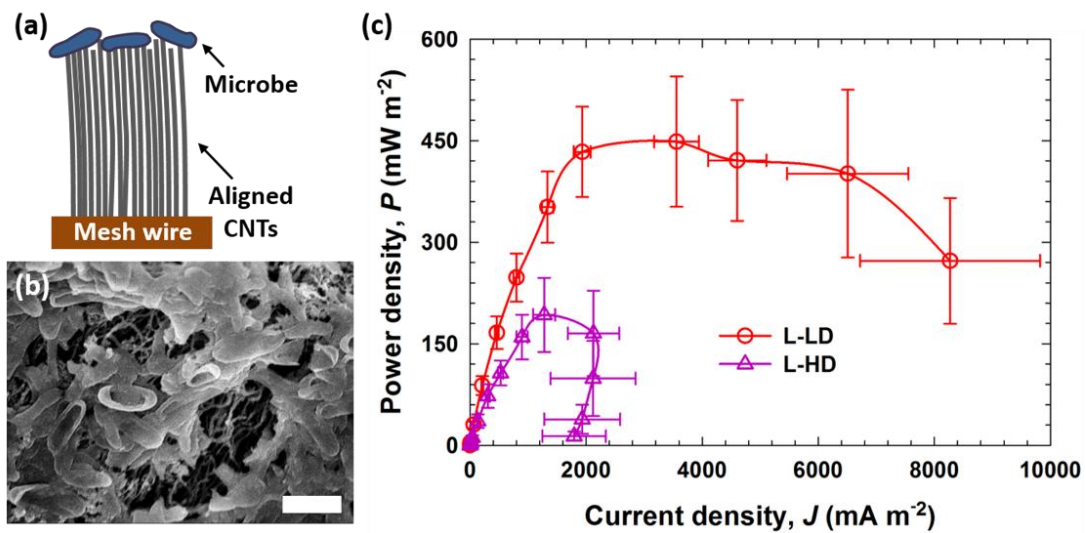
SEM images in Figure 3.3.e, 3.3.f, 3.3.g, and 3.3.h, which respectively depict bare mesh, short, medium and long CNTs (samples S-LD, M-LD, and L-LD) showed significantly more microbes on the electrode with the longest CNTs than their shorter counterparts. This finding correlates well with the significant differences in power densities, as the power density from the long CNTs (L-LD; ~19  $\mu\text{m}$ ; 450  $\text{mW m}^{-2}$ ) was 28% higher than that from the short CNTs (S-LD; ~8  $\mu\text{m}$ ; 350  $\text{mW m}^{-2}$ ). However the power improvement was limited compared to that from the medium-length CNTs (sample L-LD showing only 5% higher power than sample M-LD; ~13  $\mu\text{m}$ ; 425  $\text{mW m}^{-2}$ ). Overall, this result supports the idea that the larger surface areas provided by long CNTs gives higher power output due to the increased numbers of sites for EABs to attach on the electrodes.



**Figure 3.3.** Power performance and CNT-SS mesh electrodes with different CNT lengths after MFC runs. (a) Power densities against current density of S-LD, M-LD, L-LD, and a bare SS mesh elucidate the effect of the CNT length. (b) Illustration of the interactions between microbes and the CNT-SS mesh electrodes. For a bare mesh, the number of microbes responsible for transferring electrons is limited (upper left pane). Even the electrode with relatively short CNTs (lower left pane) has more microbes than the bare SS mesh electrode. For the electrode with long CNTs, a large number of microbes can interact with CNTs along the stem of CNTs (right pane). This was confirmed by a SEM (c), showing microbes captured by CNTs like tentacles. A row of CNTs were scratched off along the axis of the mesh wire for visualization. An enlarged view from a different angle (d) shows that microbes were entangled in CNTs, providing excellent conduits for transferring electrons. (e) In comparison to the CNT-SS mesh electrodes, a bare mesh with microbes laying on the surface of the mesh wire is shown. S-LD, M-LD, and L-LD after testing are respectively shown in (f), (g), and (h). The scale bars in (c), (d), and the inset of (e) indicate  $2 \mu\text{m}$  and those in (e-h) indicate  $20 \mu\text{m}$ .

### 3.3.2. Effect of CNT packing density on MFC power

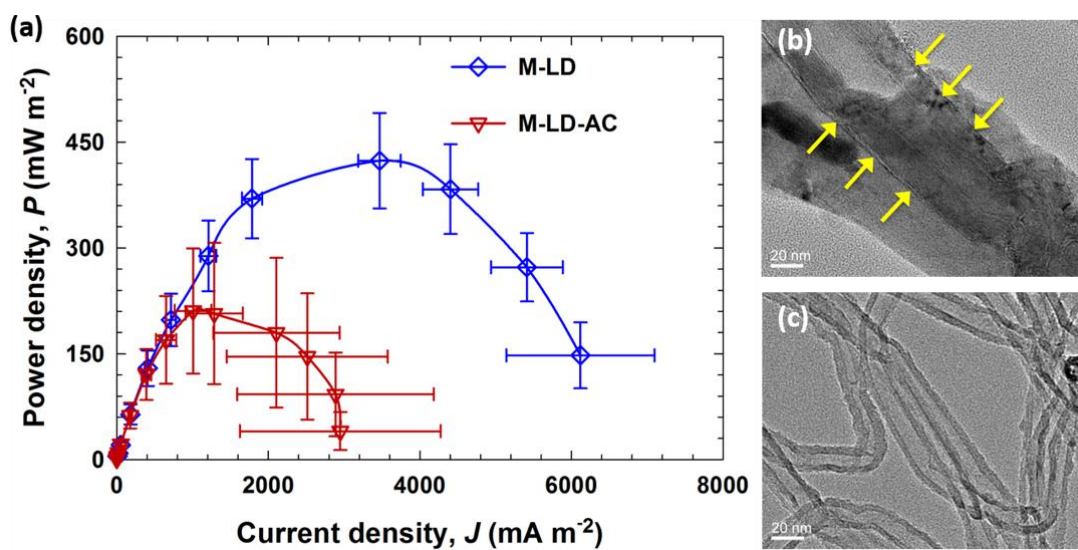
Another key aspect influencing the MFC power output is the accessibility of microbes to the CNT surfaces. To investigate this effect, the packing density of CNTs was varied by depositing a thin catalyst layer ( $< 5$  nm Fe) for the densely packed (aligned) CNTs (sample L-HD), compared to a thick catalyst layer ( $> 5$  nm Fe) used for the loosely packed CNTs (samples S-LD, M-LD, and L-LD). Since thinner layers often result in smaller and more sites for initiating CNT growth, this resulted in high-density highly aligned CNTs (Figure 3.2.f; L-HD). As schematically shown in Figure 3.4.a, when CNTs are highly aligned and densely packed, the limited space between CNTs is expected to prevent microbes from intercalating into the CNT forest. Indeed, microbes were observed mainly at the tips of the CNTs but not associated with the underlining CNTs (Figure 3.4.b), most likely due to the lack of physical space between the CNTs. The reduced number of microbes, in turn, significantly lowered the maximum power density to 43% ( $193 \text{ mW m}^{-2}$  for L-HD) of that from the low-density CNT electrode ( $450 \text{ mW m}^{-2}$  for L-LD) (Figure 3.4.c). Mink et al. also used MWCNTs grown through a plasma enhanced CVD method on Cr/Ni catalysts. However this approach showed a power improvement of only 26% compared to bare carbon cloth, probably because microbial growth inside the CNT forest was limited due to the densely packed CNTs and relatively small surface areas due to the large diameters (200~400 nm) of the CNTs used in their experiments [27]. The microbial colonization of only the top part of the CNTs does not significantly improve the performance, thus the loosely packed CNTs contribute to higher power output than densely packed CNTs.



**Figure 3.4.** Characteristics of aligned and densely packed CNT-SS mesh electrode. (a) Microbes are difficult to get into the CNT forest, making microbes sit on the tip of CNTs. (b) A top view of L-HD after testing, showing microbes only on the top surface of the CNT electrode but not inside the CNT forest, as can be seen through the cracks of the biofilm. The scale bar indicates 2 μm. (c) The power density of L-HD in comparison to that of L-LD whose CNT lengths were similar.

### 3.3.3. Effect of amorphous carbon on CNTs

As non-optimal growth of CNTs can easily result in a layer of amorphous carbon on CNTs, we investigated how electrical contacts between microbes and CNTs influence the MFC power output by preparing a CNT electrode having amorphous carbon layers. The CNT surface condition was altered by etching SS meshes with an aqueous HCl solution. The etching process roughens the surface of SS meshes, revealing relatively large catalytic Fe sites for CNT growth. This resulted in CNTs covered intentionally with a thick layer of amorphous carbon (Figure 3.2.g) that was responsible for the uneven surfaces and larger diameters of CNTs (Figure 3.2.h) as opposed to the other samples (no amorphous carbon layers) displaying smooth surfaces and smaller diameters (inset of Figure 3.2.c). The power density of the amorphous carbon-coated CNT electrode (M-LD-AC) resulted in 50% reduction in power to  $\sim 210 \text{ mW m}^{-2}$ , compared to that of similar length and density containing a negligible amount of amorphous carbon (M-LD;  $\sim 425 \text{ mW m}^{-2}$ ) (Figure 3.5.a). A transmission electron micrograph (TEM) shows that a thick carbon layer wrapped around the CNTs (outer walls of CNTs are marked by arrows in Figure 3.5.b). This coating layer made the overall diameter of these CNTs thicker (100 nm) compared to M-LD samples (30~60 nm; Figure 3.5.c). The graphitic layer of CNTs often makes relatively strong bonding with organic molecules due to dangling bonds and  $\pi$ - $\pi$  interactions [81]. Electrochemically active bacteria can transfer electrons through their microbial nanowires through  $\pi$ - $\pi$  interchain stacking and delocalization of charges [82-85], suggesting intimate interactions between microbial nanowires and CNTs. Therefore, the amorphous carbon layer would result in a weaker bonding and thereby a large ohmic loss.

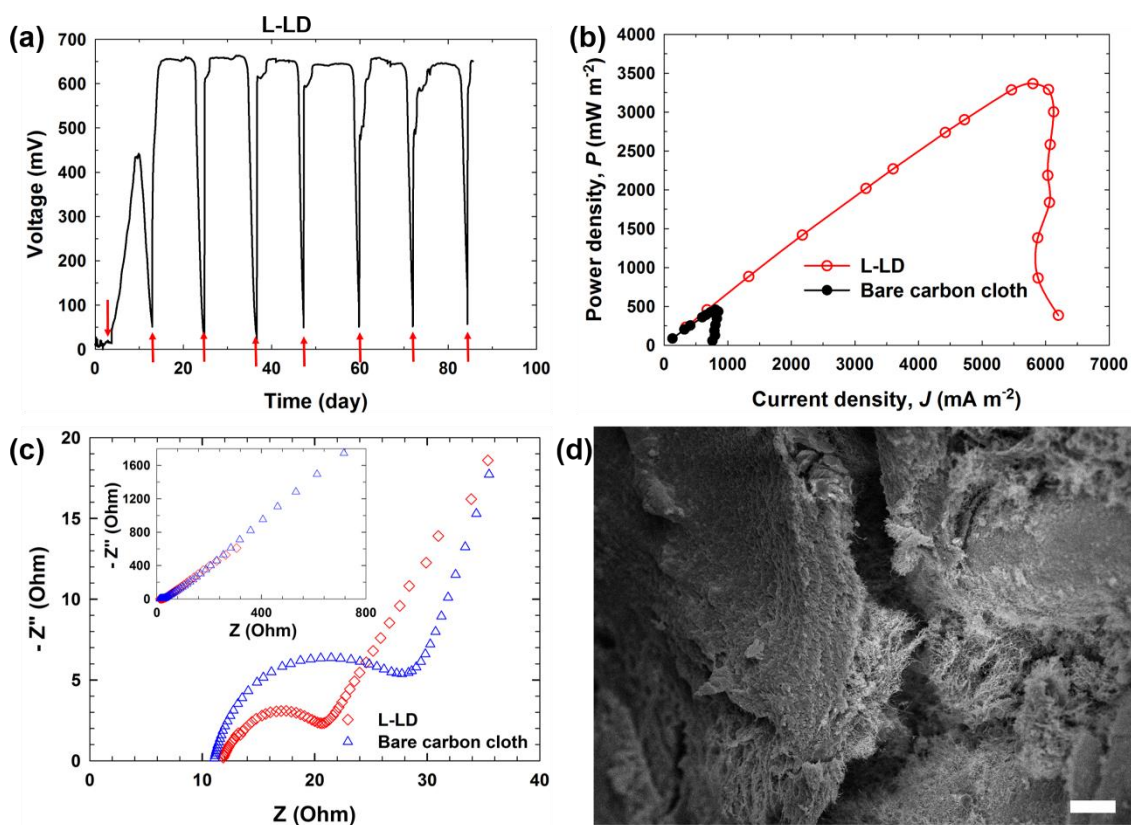


**Figure 3.5.** Characteristics of CNT-SS mesh electrode with amorphous carbon coating. (a) The power density of M-LD-AC (amorphous carbon coating layer) in comparison to that of M-LD, whose CNT lengths were similar. (b) Amorphous carbon coating layers were clearly observed from M-LD-AC outside of the CNT. The arrows mark an individual MWCNT. (c) L-LD had only graphitic carbons.



### **3.3.4. Long-term performance of L-LD in 100 mL MFC**

Based on these systematic studies, the CNT electrode having long, loosely-packed, and low-density CNTs without any amorphous carbon showed the highest power improvement during the short-term studies. Therefore, this electrode was selected for testing its long-term performance in a two-chamber MFC (100 mL). The MFC anode chamber (50 mL) was inoculated with anaerobic wastewater and fed with acetate. After 4-5 days of operation, MFC voltage increased to greater than 0.6 V (Figure 3.6.a). Polarization curves was obtained after the fresh acetate medium addition, and showed maximum power density of 3360 mW m<sup>-2</sup>. This power density is 7.4-times higher than that from a bare carbon cloth electrode (456 mW m<sup>-2</sup>) (Figure 3.6.b), which is the largest percentage increase with CNT-modified anode reported so far, to the best of our knowledge. The absolute power density from this result is also amongst the highest power densities reported so far, however direct comparison of power densities across different MFC platforms and wastewater substrates remains a challenge. Electrochemical impedance spectroscopy (EIS) tests were conducted at open circuit voltage and the Nyquist curves are shown in Figure 3.6.c. The charge transfer resistance of the electrode after microbial biofilm was lower than that of bare carbon cloth, demonstrating that the CNT-grown SS mesh has better performance due to the larger surface area and enhanced biofilm formation which is shown in the SEM image taken after 3 months of MFC operation (Figure 3.6.d).



**Figure 3.6.** Long-term performance of L-LD in a two-chamber MFC device (100 mL). (a) Voltage generation over time showing a sharp increase in voltage after acetate inoculation (arrow marks) and short start-up time (4-5 days). (b) Polarization curves of L-LD and bare carbon cloth (control) showing the maximum power densities achieved with wastewater and acetate and the maximum power density generated by the L-LD anode is 7.4 times that of the bare carbon cloth ( $3360 \text{ mW m}^{-2}$  vs  $456 \text{ mW m}^{-2}$ ). (c) Nyquist curves for the microbial fuel cells equipped with the L-LD and bare carbon cloth. Full curves are shown in an inset graph. (d) SEM image of the microbial growth, where cross section of the L-LD after 3 months of operation shows microbial colonization inside of the CNT forest. The scale bar indicates  $10 \mu\text{m}$ .

### 3.4. Discussion

Overall, the large performance improvement was probably facilitated by the excellent electrical conductivity of CNTs ( $10^5\sim 10^7$  S  $m^{-1}$ ) [33, 86], which provides excellent charge pathways with minimal ohmic loss throughout the multiple layers of microbes. For typical two-dimensional electrodes, thick biofilms generally contribute to higher electricity generation but their electron transfer efficiency is low due to significant ohmic loss caused by the low electrical conductivity of biofilms (e.g., *Geobacter sulfurreducens* biofilms was measured to be  $\sim 5\times 10^{-3}$  S  $cm^{-1}$ ) [84]. In this case, only a few layers of microbes near electrodes have good charge interactions. Several groups utilized CNT dipping methods, including Xie et al. who fabricated the CNT-textile by dipping a piece of non-conductive textile in CNT ink and improved the power density 68% compared to carbon cloth [77]. The dipping method does not provide strong connection between the CNTs and the base material and thus limits the electron transfer from microbes. Similar methods were also used in several other works [27, 75, 76] but the power improvements compared to control electrodes were limited, presumably due to the same reason. The CVD method to directly grow CNTs on the base electrode materials as presented here can increase the efficiency of charge transfer due to the stronger attachment of CNTs. As such, the CVD method used on graphite felt showed 5 times improvement compared to bare electrode [78]. Indeed, the current-voltage sweeping measurements using out electrodes revealed that the contacts between the SS wires and CNTs are ohmic. The stainless steel mesh in our experiment appears to be stable in a short term such as several months. This could be due to direct synthesis of CNTs on SS meshes that coats the meshes with carbon, improving corrosion

resistance. However the long-term stability of more than one year for stainless steel still need to be investigated. The use of SS mesh, which can be several times cheaper than the graphite felt, has thus strong potential towards low-cost high-performance MFC anode materials.

### **3.5. Conclusion**

In summary, we synthesized tentacle-like CNTs directly grown from SS meshes in the radial direction of mesh wires, providing microbes with three-dimensional and large surface areas. CNTs captured microbes like tentacles, resulting in excellent charge transfer characteristics presumably due to  $\pi$ - $\pi$  stacking between the graphitic carbon rings of CNTs and the pili of microbes. Another key feature of our new electrodes is their minimal ohmic loss due to the direct growth of CNTs from SS meshes. The systematic variation of CNT length, density, and surface condition elucidated the contribution of each parameter to the power performance. It was found that the longer CNTs provided more sites for microbes to transfer charge, resulting in higher power output. It was also important to maintain large enough spaces between CNTs for microbes to be intercalated in between. We also found that the graphitic layer of CNTs with minimum amorphous carbon provided an excellent substrate for charge interaction. The CNT-SSM electrode that showed the best performance during short-term testing (long, loosely-packed, and no amorphous carbon) was further tested with wastewater and its long-term performance showed maximum power density of  $3360 \text{ mW m}^{-2}$ , 7.4-times higher than that from carbon cloth, being amongst the highest power improvements in nanomaterial-based MFC anodes. Here, we

fabricated a highly efficient nanomaterial-based electrode that offer great potential for advancing the development of microbial electrochemical systems.

## 4. THREE-DIMENSIONAL POROUS CARBON NANOTUBE SPONGES FOR HIGH PERFORMANCE ANODES OF MICROBIAL FUEL CELLS\*

### 4.1. Introduction

While most commonly used anode materials are carbon cloth, carbon felt, and carbon paper [87, 88], it has been found that 3D carbon brush structures can significantly increase power output by maximizing the contact of EABs to anode, and are now also broadly used [89]. In carbon brushes, straight long carbon fibers whose diameters are 7-10 micrometers are arranged in the radial direction that allows EABs to be attached throughout the brush electrode. This brush design is superior to 2D electrodes (eg. carbon cloth, carbon paper) because of the large surface area per volume. However the large spacing between the carbon fibers (typically in several tens to hundreds of micrometers) and relatively high ohmic resistance of this material leave further room for significant improvement.

Various nanomaterials have been explored to overcome such limitations, such as metal nanoparticles [17], graphene [21, 88, 90-92], carbon nanotubes (CNTs) [22, 23, 25-27, 77, 79], and polymer composites with embedded nanoscale carbon materials [30, 78, 93], all providing orders of magnitude higher surface areas than that of 2D electrodes ( $< 1 \text{ m}^2 \text{ g}^{-1}$ ) and 3D brush electrodes ( $\sim 0.7 \text{ m}^2 \text{ g}^{-1}$ ). However these nanomaterials generally require some sort of 2D or 3D support substrates such as carbon paper [26], carbon cloth

---

\* Reprinted with permission from “Three-dimensional porous carbon nanotube sponges for high-performance anodes of microbial fuel cells” by Celal Erbay, Gang Yang, Paul de Figueiredo, Reza Sadr, Choongho Yu, Arum Han, 2015. *Journal of Power Sources*, 298, 177-183, Copyright [2015] by Elsevier.

[79], textile [77], and stainless steel mesh [23], which contains less conductive materials and/or limits thickness of nanomaterial layers to have 3D structures. Recent development in 3D nanostructures may alleviate such drawbacks. For instance, a graphene coated sponge [91] with stainless steel as a current collector, a graphene modified nickel foam [21], a graphene foam coated with polyaniline (PANI) [93] all have shown high performances by allowing efficient electron transfer and mass transport by combining highly conductive nanomaterials with 3D structures. Nonetheless, most of these high-performance 3D structured electrodes typically require complicated synthesis processes such as carbonization and reoxidation [30, 90]. This complexity significantly increases the cost of the electrodes as well as are difficult to scale-up, which makes these high performance electrodes impractical for most MFC applications.

Here, porous and flexible 3D CNT sponges were synthesized by using a simple and facile one-step process without the need for any substrates or base/sacrificial materials. One-step synthesis that does not require any pre and post processes to make the CNT sponges such as catalyst deposition on substrates or removal of unwanted materials was advantageous to fabricate them in a short time. The spontaneously formed sponge is also scalable, which makes it suitable for low-cost bulk manufacturing. The 3D CNT sponge anodes were tested in various MFC sizes to characterize their power density.

## **4.2. Experimental**

### **4.2.1. Preparation and characterization of CNT sponge electrode**

To synthesize the CNT sponge, a chemical vapor deposition (CVD) method was employed. A three-zone furnace (Lindberg/Blue M STF55346C) equipped with a quartz tube (1 inch in diameter) was used to individually control the temperature of the reaction zones. After a 30-min growth reaction, a CNT sponge with ~10 cm in length and 22 mm in diameter was formed. As-synthesized CNT sponge shows highly porous structure (~98% porosity), and is comprised of randomly oriented and entangled CNTs. The CNT sponges were fabricated by Dr. Yu's research group in Materials Science and Engineering department at Texas A&M University [94].

### **4.2.2. MFC setup and operation**

The synthesized CNT sponge as anode along with carbon felt (Morgan, UK) for comparison was tested in three different sizes of two-chamber MFCs. Three different chamber sizes were used to fully characterize the CNT sponge anode performances at various size scales. Small (SMFC), medium (MMFC), and large MFC (LMFC) have two chambers (anode and cathode chambers) of 0.5, 20, and 120 mL, respectively. The two chambers were separated by a proton exchange membrane (PEM) (Nafion 117<sup>TM</sup>, Ion Power Inc.; 1 cm<sup>2</sup> for SMFC; 7 cm<sup>2</sup> for MMFC; 19.6 cm<sup>2</sup> for LMFC) that was placed between silicon rubber gaskets to prevent liquid leak. CNT sponge anodes (1×1×0.3 cm<sup>3</sup>; same for all MFCs) and carbon cloth cathodes (1×1 cm<sup>2</sup> for SMFC; 2×2 cm<sup>2</sup> for MMFC;



3×4 cm<sup>2</sup> for LMFC) having platinum catalysts on one side (10 wt% Pt/C, 0.5 mg of Pt per cm<sup>2</sup>, ElectroChem, Inc.) were used. Titanium wires were used to hook the electrodes for electrical connection.

The anode chambers were inoculated with anaerobically activated sludge (Austin Wastewater Plant). The anode chambers were fed with a medium containing sodium acetate (1.5 g L<sup>-1</sup>) and autoclaved anaerobic nutrient mineral buffer (NMB, pH 7.0) solution [95]. The MFCs were operated in a batch mode and acetate was inoculated after the voltage dropped below 50 mV. Nitrogen was purged for 15 min to make the chambers anaerobic after each inoculation. The medium was mixed by using a magnetic stirrer at 350 rpm during the experiment (only for the MMFC and LMFC due to the size limitation). The cathode chambers were filled with 100 mM ferricyanide ([Fe(CN)<sub>6</sub>]<sup>3-</sup>).

Cell voltage across a load resistor (1 kΩ) was recorded every 120 sec using a multiplexer (NI PXI-2575, National Instruments) for continuous voltage measurements via a LabView™ (National Instruments) interface [57]. Polarization curves were obtained by varying the load resistor from 10 kΩ to 100 Ω when voltage was stable after several operation cycles. Power ( $P$ ) was calculated by  $P=V^2 R^{-1}$  based on the recorded voltage ( $V$ ) and load resistance ( $R$ ). The current and power densities were normalized by the volume of anode (0.3 mL) or anode chambers (0.5, 20, 120 mL) for each case.

#### **4.2.3. Biofilm characterization**

To inspect the biofilms on the CNT sponge and carbon felt, the anode was first rinsed with phosphate buffered saline (PBS), and then microbes were fixed using 4% glutaraldehyde

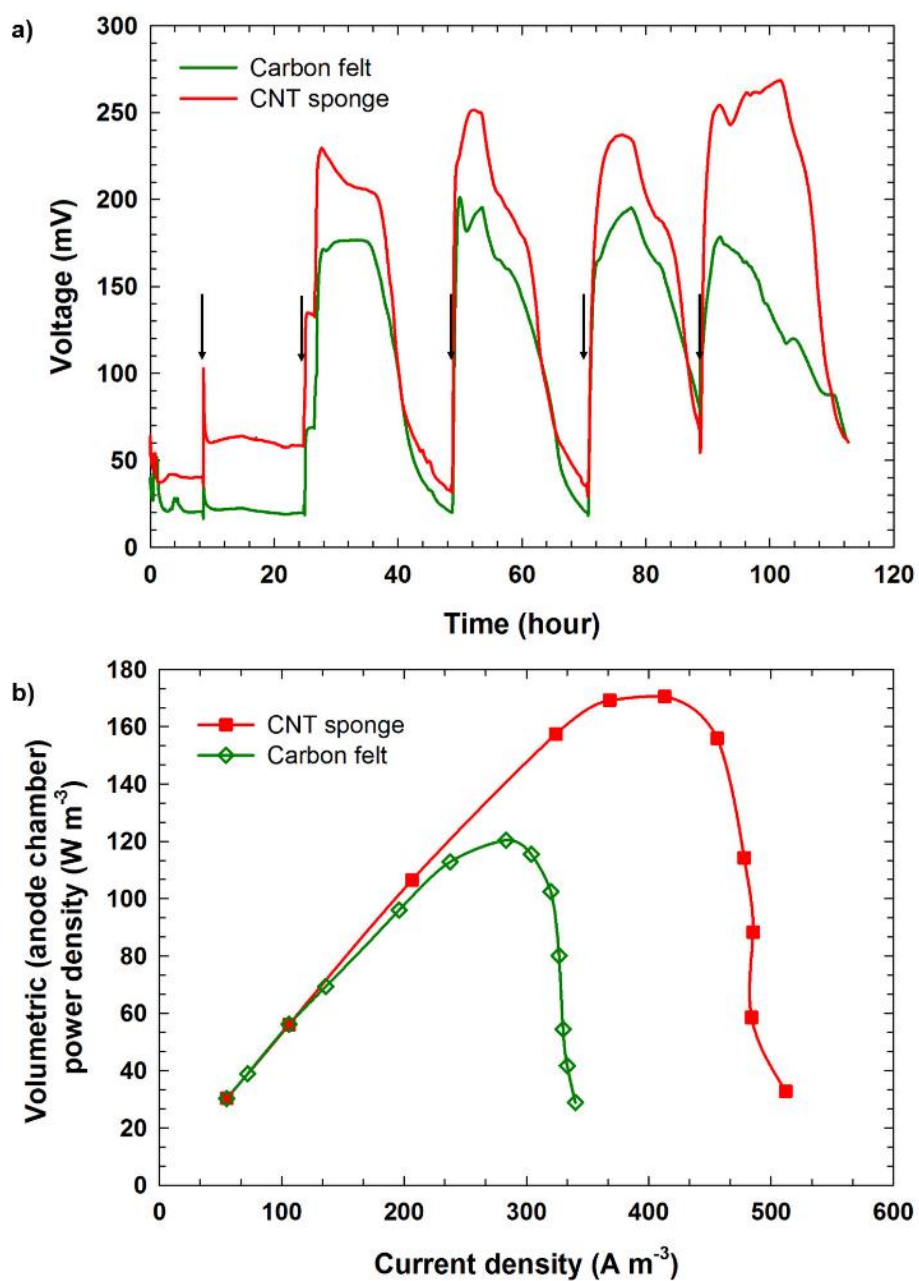
and 4% formaldehyde for 5 hours. The samples were carefully rinsed three times in PBS (pH 7.0) and then once in deionized water, followed by a series of dehydration steps using increasing concentrations of ethanol (25, 50, 75, and 95 wt%; 10 min for each stage with very gentle periodic agitation) and then thorough drying at room temperature overnight. The samples were coated with ~5-nm thick Pt/Pd for inspection under the SEM.

### **4.3. CNT sponge as the anode in MFC**

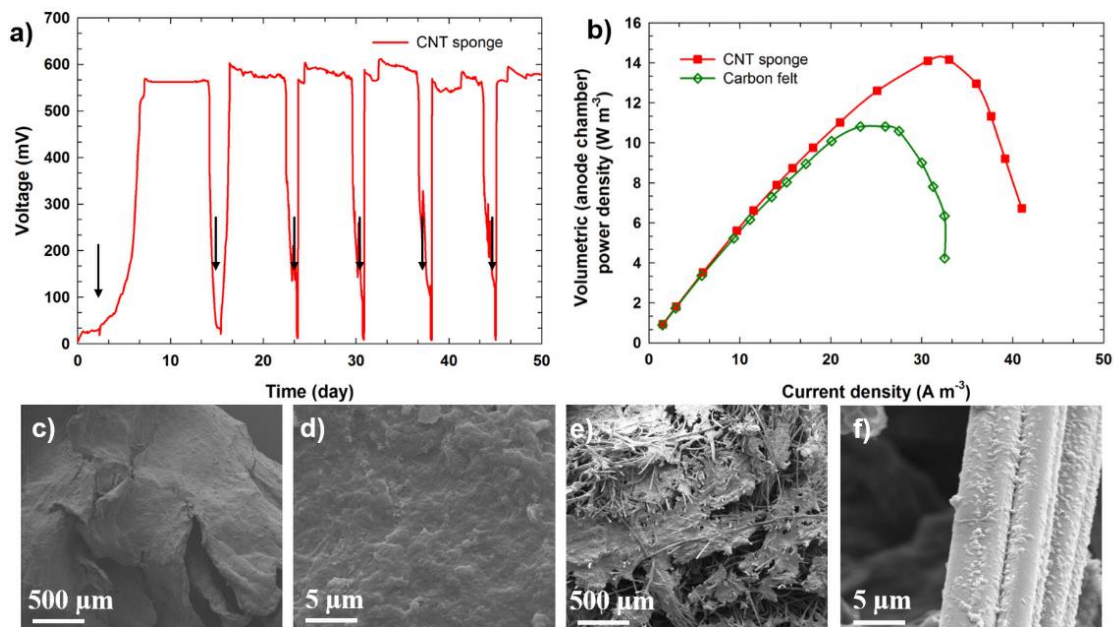
We first tested the CNT anode in SMFC. The voltage increased to ~250 mV over a 1 k $\Omega$  load resistor in about one day, as shown in Figure 4.1.a. Meanwhile carbon felt anode produced a slightly lower voltage of 170 mV. The volumetric maximum power density (normalized to the anode chamber volume of the SMFC) generated by the CNT sponge anode was ~170 W m<sup>-3</sup>, which was approximately 1.4 times higher than that of a commercial carbon felt (~120 W m<sup>-3</sup>), as shown in Figure 4.1.b. Here the CNT sponge and carbon felt electrodes filled approximately 60% of the anode chambers.

In order to evaluate the long-term performance of the CNT sponge anode, MMFC whose anode chamber volume is 40-times larger (20 mL) was used. After 5 days from inoculation with wastewater, voltage over a 1 k $\Omega$  load resistor reached a higher voltage of ~550 mV (Figure 4.2.a), which was maintained for more than 50 days, indicating its high stability. The maximum volumetric power density (normalized to the anode chamber volume) of the MMFC with the CNT sponge anode (14.1 W m<sup>-3</sup>) was 1.3 times higher than that of the MMFC with carbon felt (10.8 W m<sup>-3</sup>), as shown in Figure 4.2.b. This long-term test result shows that porous 3D CNT sponge anode developed here has better

performance compared to commercial carbon felt frequently used as 3D anode materials in MFCs. This improved performance could be attributed to more uniform biofilm growth on the CNT sponge compared to that of the carbon felt, based on the SEM images after 50 days of operation (Figure 4.2.c,d for the CNT sponge anode; Figure 4.2.e,f for the carbon felt). CNTs were not observed in the CNT sponge anode, suggesting that microbes completely and uniformly covered the entire surface of the CNT sponge anode. On the contrary, microbes on the carbon felt were mainly attached to the carbon fibers, resulting in non-uniform and less dense biofilm. This difference suggests a substantially improved contact between the anode and the biofilm in the case of CNT sponge, which can be due to high surface area of the CNT sponge as well as the  $\pi$ - $\pi$  interactions between the graphitic layers of the CNTs and the attached microbes.



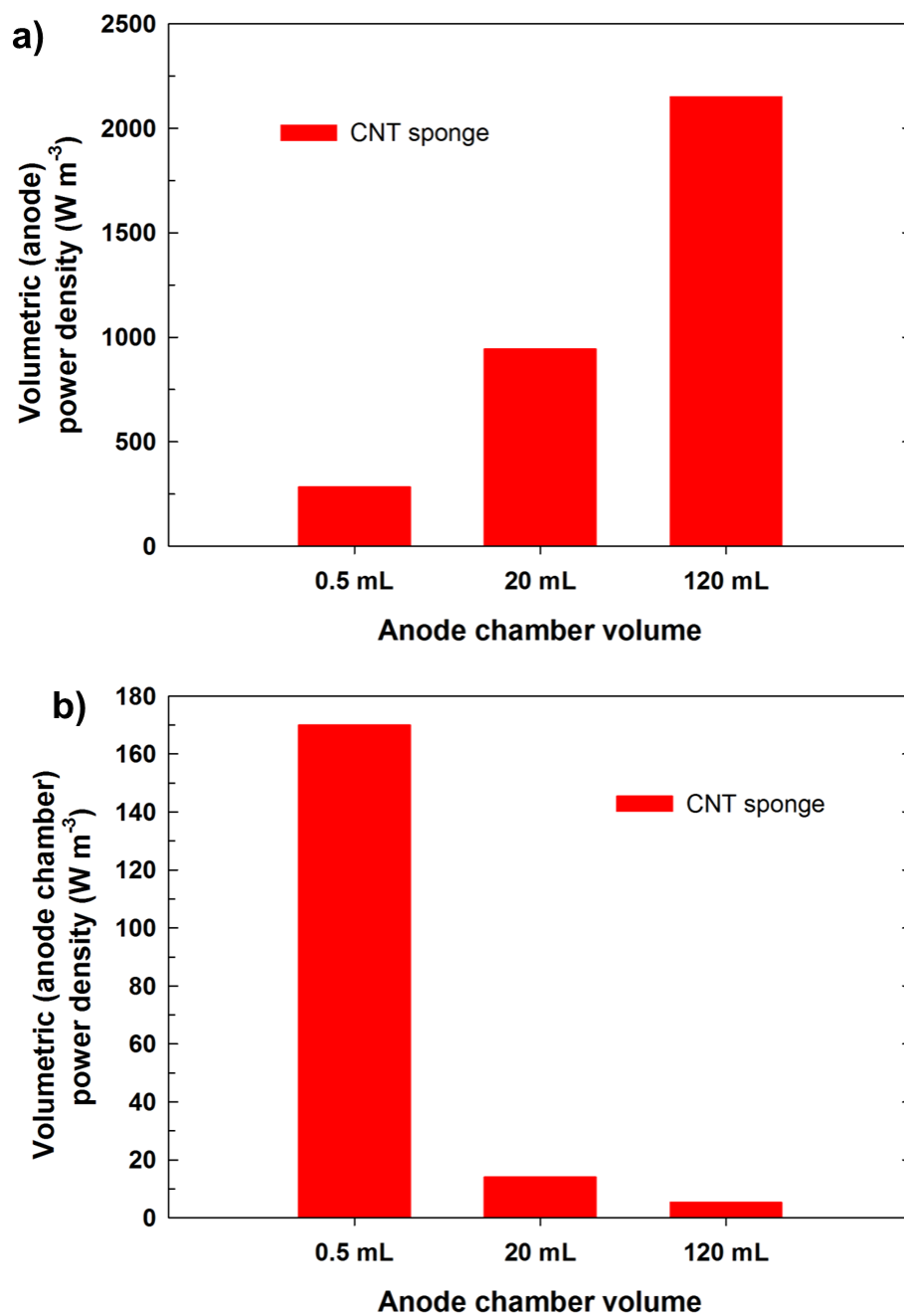
**Figure 4.1.** Performance of the SMFCs equipped with different anode electrode materials (CNT sponge and carbon felt). (a) Voltage output over time of the MFCs with a  $1 \text{ k}\Omega$  load resistor. Arrows indicate media replenishment. (b) Polarization curve comparing the volumetric power density (based on anode chamber volume,  $0.5 \text{ ml}$ ) of the MFC with CNT sponge anode compared to that with carbon felt anode.



**Figure 4.2.** (a) Performance of the MMFC (20 ml anode chamber volume) with CNT sponge anode operating in batch mode with a 1 kΩ load resistor. The arrows indicate the replenishment of the media (acetate). (b) Polarization curves of the CNT sponge anode MMFC compared to that of the carbon felt anode MMFC. The volumetric power densities were calculated based on the volume of anode chamber (20 mL). (c, d) SEM images of the biofilm grown on the CNT sponge anode at low and high resolutions. (e, f) SEM images of the biofilm grown on the carbon felt anode at low and high resolutions.

#### 4.4. Discussion

The CNT sponge anode was also tested in the LMFC having 6 times larger anode volume compared to the MMFC. The power densities of the CNT sponge anodes in the SMFC, MMFC, and LMFC cases were compared by normalizing against the sponge anode volume (Figure 4.3.a) and the anode chamber volume (Figure 4.3.b). Both normalization methods were used to be able to compare to literature, as some report power densities based on the anode chamber volume and some based on the anode volume. It should be noted that the volume of the CNT sponge anode is identical for all experiments in this study. With larger chamber volumes, the power density per volume of the CNT sponge anode was highest, reaching  $2150 \text{ W m}^{-3}$  for LMFC, which is 2.3 and 7.6 times higher than those of the MMFC ( $943 \text{ W m}^{-3}$ ) and of the SMFC ( $283 \text{ W m}^{-3}$ ) (Figure 4.3.a). This increment can be ascribed to more microbes in the larger MFC chamber, suggesting that active surface area of the CNT sponge is sufficiently large as to not saturate the power generation. On the other hand, the power density normalized to the anode chamber volume was highest ( $170 \text{ W m}^{-3}$ ) from the SMFC (Figure 4.3.b), which has a significantly higher volume percentage (60%) of anode chamber occupied by the anode, compared to the cases of MMFC (1.5%) and LMFC (0.25%). These results suggest that it is better to have a large chamber volume to obtain high power generation, at the same time filling a significant portion of the chamber volume with anode will be ideal to effectively utilize the total volume of the cell. We also expect that further study with single-chamber air-cathode MFCs may improve the maximum power density of two-chamber MFCs in this work, which we plan to do as a follow-up study.



**Figure 4.3.** Performance comparison of the CNT sponge anode loaded in MFCs having three different anode chamber volumes. (a) Volumetric power densities normalized to the anode volume ( $0.3 \text{ cm}^3$ ). (b) Volumetric power densities normalized to the volume of the anode chamber.

As shown in Table 2, reported power densities in literature greatly vary not only depending on the MFC configurations (*e.g.*, the number of chambers, the size of electrodes and PEM) and operating conditions (*e.g.*, microorganisms and substrates used), but also depending on the size/volume of electrodes used to calculate the power densities and the volume ratio of the chamber to electrode. Table 2 compares the power density of our CNT sponge anode with previously reported nanomaterial based 3D anodes in MFCs. Among these representative results, our LMFC and SMFC was the best in terms of the power density per anode volume and per anode chamber volume, respectively. For example, when anodes were made of insulating polyurethane sponges decorated with commercially available CNTs [22] or graphene [91] by a dipping method, their power density per chamber volume was, respectively, measured to be only  $0.66 \text{ W m}^{-3}$  and  $1.05 \text{ W m}^{-3}$ , significantly lower than our values presumably due to poor electrical contact between the nanomaterials due to the insulating surfactants and/or binders. Test using the 3D graphene sponge anode tested in a two-chamber MFC [90] resulted in a volumetric power density (per chamber volume) of  $3.41 \text{ W m}^{-3}$ , showing only 8% increase compared to that of carbon felt anode, potentially due to the small pore sizes in the graphene sponge anode.

Overall, most importantly, the synthesis process for the CNT sponges presented here is scalable, simple, facile, and inexpensive, compared to those in literature. For instance, longer and complicated processes such as polymerization and carbonization were necessary to obtain 3D nitrogen-enriched carbon nanoparticle coated anode that resulted from the carbonization of PANI and natural fibrous loofah sponge [30]. Graphene oxide anode required very long (> 2 days) processes with expensive nickel foams as substrates



[21]. Our one-step processing method has a very low production cost about  $\sim\$0.1/\text{g}_{\text{CNT}}$  or  $\sim\$4.7/\text{L}$ , whose density is  $\sim 47 \text{ mg}/\text{cm}^3$ , which is much lower than those of previously reported methods [96-101]. The calculated cost here is based on using 0.3 g of ferrocene ( $\$108/500\text{g}$ ), 2.4 L of  $\text{C}_2\text{H}_4$  ( $\$22$  for  $300 \text{ ft}^3$ ), 7.8 L of  $\text{H}_2$  ( $\$45$  for  $300 \text{ ft}^3$ ), and 2.4 L of Ar ( $\$48$  for  $300 \text{ ft}^3$ ) for the 30min synthesis time. The total cost was then normalized to the current production rate of  $\sim 3.6 \text{ g}/\text{h}$ . This production rate was also orders of magnitude higher ( $\sim 3.6 \text{ g}/\text{h}$ , representing  $20 \text{ cm}/\text{h}$  of a  $2.2 \text{ cm}$  diameter CNT sponge) compared to other nanomaterial-based anode synthesis ( $\sim 0.02 \text{ g}/\text{h}$ ) [96, 97, 99, 100]. The process is also scalable, where the diameter of the CNT sponge is controlled by the diameter of the furnace tube used and the length is controlled by the synthesis time (currently 1 h to obtain a  $20 \text{ cm}$  long and  $2 \text{ cm}$  diameter CNT sponge). Thus simply using a larger-diameter furnace tube and longer synthesis time can easily result in scaled-up production of the presented 3D CNT sponge electrode materials. Here, the presented CNT sponge anode shows not only high power density in MFC applications, but also low cost and scalability, which will have broad applicability in microbial electrochemical cell systems (e.g., MFC, microbial electrolysis cells, and microbial desalination cells) in general.

**Table 2.** Performance summary of 3D nanomaterial anodes in MFCs.

Anode (mL)	Anode chamber (mL)	Power density per anode volume (W/m <sup>3</sup> )	Power density per anode chamber volume (W/m <sup>3</sup> )	Ref.
Graphene-sponge SSM as electron collector (0.4)	150	394	1.05*	[91]
CNT coated sponge (0.2)	150	990*	0.66	[22]
CNT coated sponge (0.2)	0.2	325*	325	[22]
Graphene-sponge (0.8)	100	427	3.41*	[90]
N-enriched carbon nanoparticle modified loofah sponge (1.5)	28	509*	27.2*	[30]
Reduced Graphene Oxide Nickel Foam (1)	25	661	27	[21]
CNT sponge (0.3)	0.5	283	170	This work
CNT sponge (0.3)	20	943	14.1	This work
CNT sponge (0.3)	120	2150	5.3	This work

\*Calculated values based on the reported data.

#### **4.5. Conclusion**

We fabricated a 3D sponge-like anode consisting of self-assembled, interconnected CNTs by using facile and inexpensive one-step CVD method without substrates. The highly porous, flexible, and light-weight sponge anode generated higher power densities of 2150 W m<sup>-3</sup> per anode volume and 170 W m<sup>-3</sup> per anode chamber volume, compared to those in literature. These power densities were also higher than those of commercial carbon felt electrode tested with the same configuration. This improved performance can be attributed to enhanced charge transfer between the CNT sponge anode and microbial biofilm based on the EIS results, in addition to large surface areas and favorable  $\pi$ - $\pi$  interactions between microbial nanowires and CNTs. The low cost simple to fabricate 3D CNT sponge anode presented here provides a new concept for designing MFC anodes as well as promising approach to generate electricity from wastewater in large scale applications at economically viable cost.

## 5. LAMINAR FLOW MICROFLUIDIC MICROBIAL FUEL CELL FOR OPTICAL AND ELECTROCHEMICAL MONITORING OF *SHEWANELLA ONEIDENSIS* MR-1 BIOFILM

### 5.1. Introduction

Microbial fuel cells (MFCs) are promising bioelectricity generation and wastewater treatment technology from organic biomass and waste which are rich with electrochemically active bacteria such as *Shewanella oneidensis*, *Geobacter sulfurreducens*. [13, 102] Biofilm formation and development on anode surface plays important role on the performance of the MFCs. However, the relation between the performance and real-time biofilm growth was not studied before in situ. Macro-scale MFCs are not suitable for analyzing with microscopes due to their large size. Although micro-scale MFCs are mainly considered as a micro power sources [59, 61, 103], developing micro-scale MFCs has great potential to understand the relation between biofilm growth and power production, and electron transfer mechanism between bacteria and electrode. However, high cost, fabrication complexity and moreover elastic properties (bending, swelling) of membrane caused significant issues in micro-scale chamber volume make them challenging with a separator. [62] Therefore, membrane-less laminar flow MFC can be considered as an experimental tool for studying microbial biofilm development in MFCs. In laminar flow MFC configuration, both anolyte and catholyte introduce into a microchannel proceed in parallel due to the laminar nature of the flows prevents turbulent

mixing which create natural boundary between anode and cathode chambers same like PEM.[104, 105]

Here, we developed a microfluidic laminar flow MFC with interdigitated anode to analyze the real time electrochemical activity of *Shewanella oneidensis* MR1. The device allowed us to investigate biofilm behavior and flow streams under the fluorescent microscope. Furthermore, the changes of biofilm growth was studied by the analysis of impedance measured from interdigitated anode. This device provides an excellent real-time analytical tool to understand the correlation between biofilm growth and impedance as well as power production. To best of our knowledge, it is the first study to analyze biofilm impedance in situ in MFCs.

Interdigitated anode are used for growth monitoring of biofilms in laminar flow MFC. In order to understand the impedance monitoring system with interdigitated anode, an equivalent electrical circuit is introduced and fit to the impedance spectrum. This method provides better understanding of meaningful physical parameters of biofilm development such biofilm thickness and biomass rather than conventional electrochemical impedance spectroscopy which provides internal resistances of MFCs. Impedance spectroscopy analysis is a powerful technique for detecting and monitoring bacterial growth based on electrical changes on the interdigitated electrode which was previously used to detect pathogenic bacterias such as *Salmonella thphimurium* [106] and *Escherichia coli* [107].

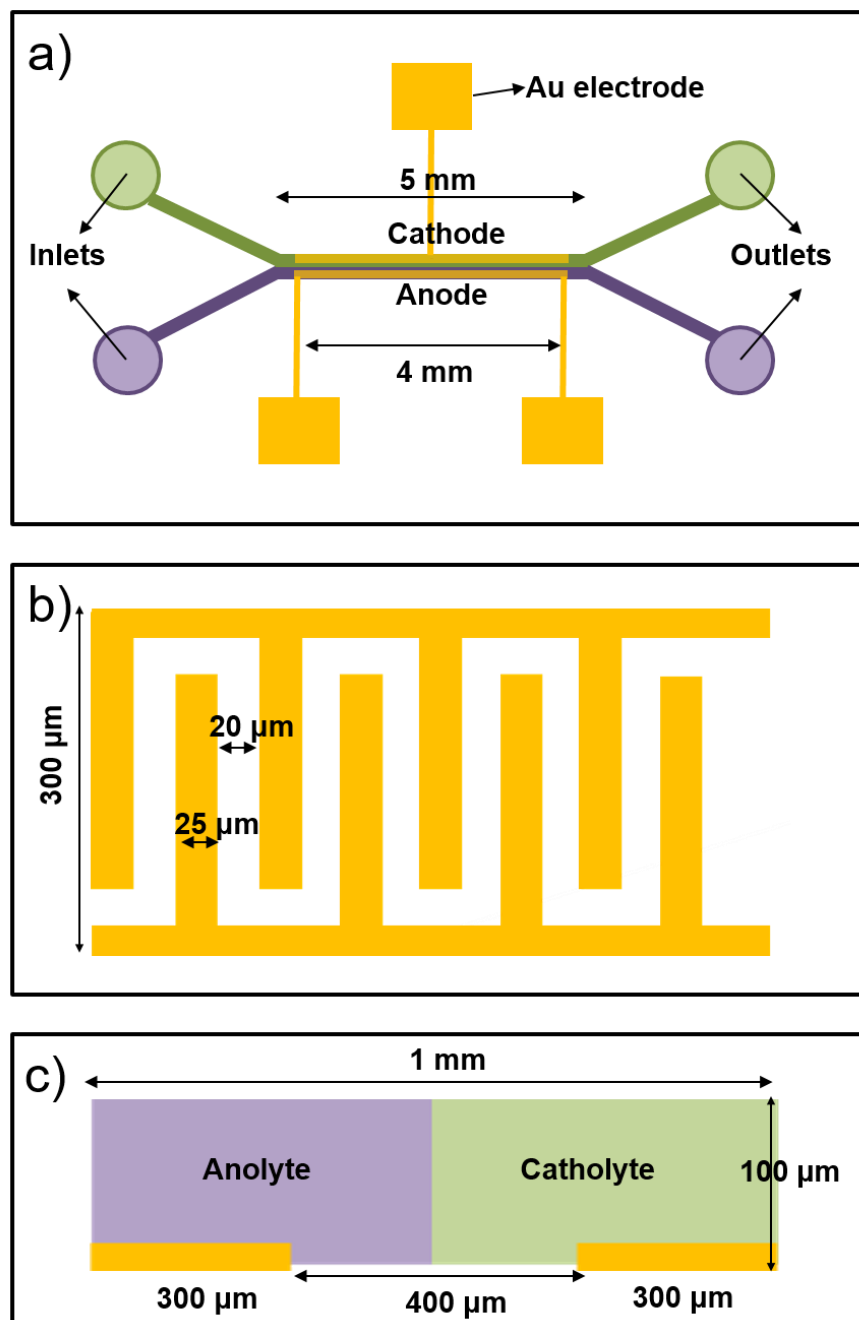
## **5.2. Materials and methods**

### **5.2.1. Cell culture**

*S. oneidensis* MR-1 transformed with plasmid p519ngfp (expressed green fluorescent protein, provided by Dr. M. Y. El-Naggar from University of Southern California) stored in tryptic soy broth (TSB) supplemented with 15% glycerol at -80 °C. Cells were streaked onto a tryptic soy agar (TSA) plate. The resultant colonies were inoculated into 3 ml of TSB liquid medium with 50 µg/mL kanamycin, and then cultured for 24 h at 30°C at 150 rpm in shaker incubator. The optical densities (OD<sub>600</sub>) were measured and adjusted to 1.0 before using in laminar flow MFC.

### **5.2.2. Laminar flow MFC design**

Microsized microfluidic laminar flow MFC device is composed of a microelectrode layer and microchannel layer. Microchannel length is 5 mm and microelectrode length is 4 mm as shown in Figure 5.1.a. It has two inlets (for anolyte and catholyte) and two outputs for effluent. Laminar nature of flows prevents them to mix and create boundary layer between anolyte and catholyte. The boundary layer works as PEM in laminar flow MFC. Microelectrode layer is composed of cathode and anode which is interdigitated electrode. After biofilm grow on interdigitated anode, impedance spectroscopy can be connected to directly on the interdigitated anode to measure its impedance values. It is composed of 50 finger pairs through the microchannel. The gap between fingers on interdigitated anode is 20  $\mu\text{m}$  and the finger width is 25  $\mu\text{m}$  as shown in Figure 5.1.b. The overall width and length of microelectrode is 300  $\mu\text{m}$  and 4000  $\mu\text{m}$ , respectively. The microchannel has 100  $\mu\text{m}$  height which allows biofilm to grow over time (Figure 5.1.c). The width of the microchannel is 1000  $\mu\text{m}$  and the gap between interdigitated anode and cathode is 400  $\mu\text{m}$  where anolyte and catholyte doesn't cause crossover on the electrodes. It is explained in section 5.3.1 in detail.

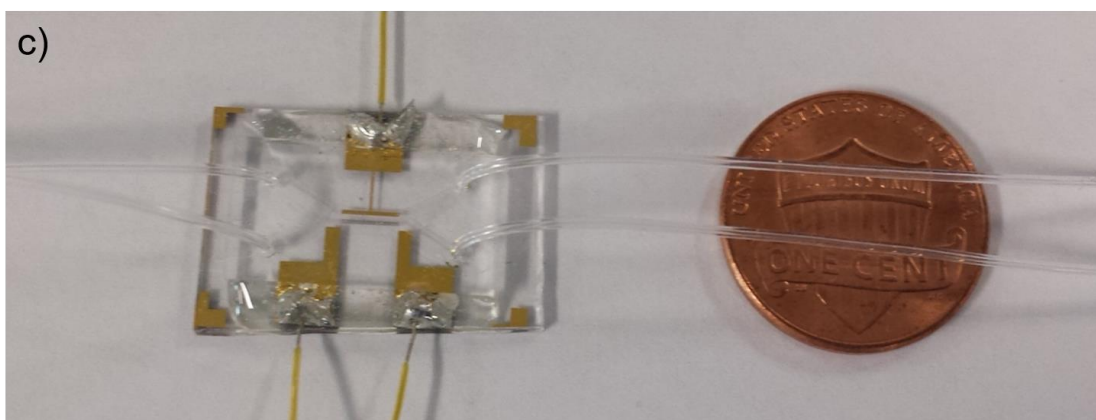
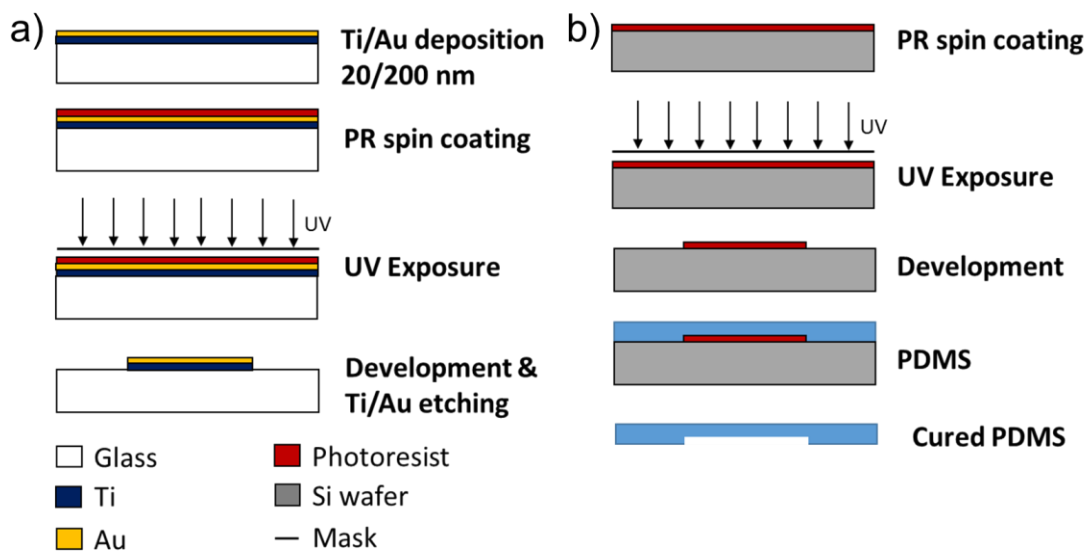


**Figure 5.1.** Microfluidic laminar flow MFC device specifications. a) Top view of the device. b) Interdigitated anode specifications. c) Cross sectional view of the microfluidic channel.



### **5.2.3. Device fabrication and assembly**

Glass substrate was cleaned in piranha solution (1:3 concentrated hydrogen peroxide to sulfuric acid) for 30 min, rinsed with deionized (DI) water and dried with N<sub>2</sub> blow. Titanium (Ti) (20 nm) and gold (Au) (200 nm) were sequentially deposited on clean glass using electron beam evaporation (Lesker PVD 75). Shipley 1818 was spin-coated on Ti/Au coated glass substrate at 3500 rpm, and then baked before exposed to UV light through a patterned photomask using a mask aligner (MA6). After photoresist developing process, the exposed part of the gold and titanium layers were removed in gold etchant and titanium etchant (1:500 concentrated hydrofluoric acid to DI water), respectively. Polydimethylsiloxane (PDMS, 10:1 mixture, Sylgard 184, Dow Corning, Inc.) microchannel was fabricated using the softlithography technique. PDMS was poured onto the silicon master that was first spin-coated with SU-8 2050 (MicroChem) at 3000 rpm and exposed to UV light by using MA6 after baking processes to obtain microchannel pattern. PDMS was then peeled from the silicon master. Schematic fabrication steps for both electrode and microchannel are shown in Figure 5.2. Glass substrate with electrodes and PDMS microchannel layers were aligned and bonded each other after oxygen plasma treatment (Harrick Plasma). For sterilization, assembled device (Figure 5.2.c) was treated with ultra-violet (UV) light for 30 min before bacteria inoculation.



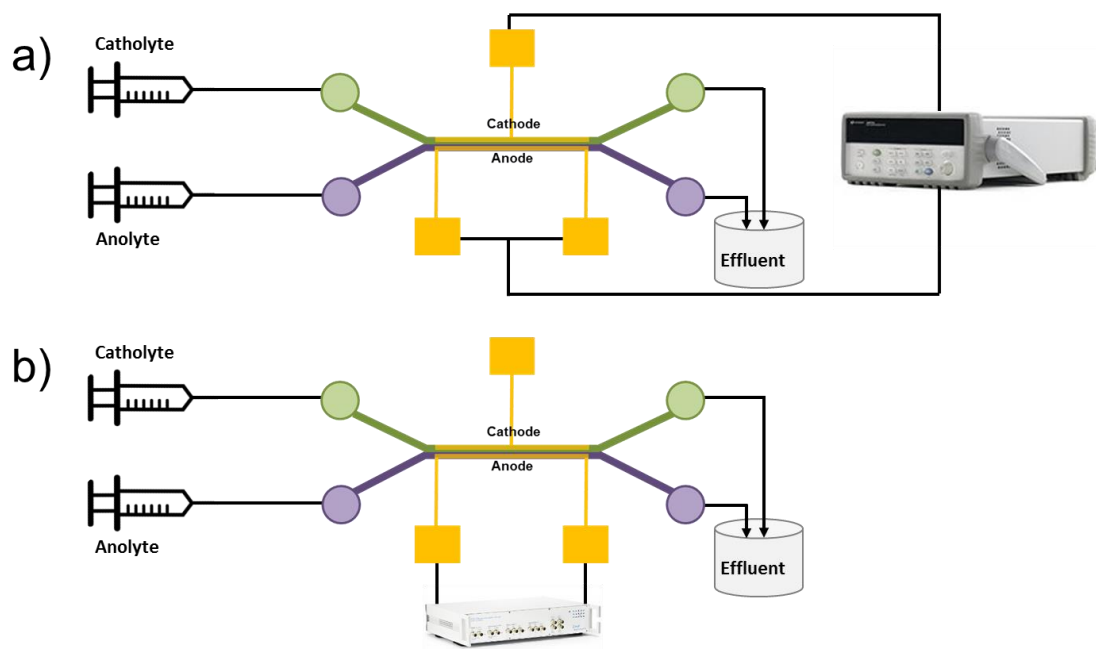
**Figure 5.2.** Microfluidic laminar flow MFC fabrication process. a) Photolithography and etching techniques were employed for fabrication of the gold electrodes. b) The microfluidic channel was fabricated using conventional soft lithography techniques. c) Photographic picture of the assembled device.

#### **5.2.4. Inoculation and device operation**

*S. oneidensis* MR-1 was first inoculated into microchannel and the flow was stopped for 4 hours to allow initial bacterial growth. Then, both anolyte (TSB, autoclaved at 121 °C for 15 min) and catholyte (100 mM ferricyanide in 100 mM phosphate buffer saline) were flowed continuously at a flow rate of 20  $\mu\text{L}/\text{min}$  by a syringe pump (Chemyx Fusion 200). Open circuit voltage (OCV) was measured between anode and cathode using data acquisition equipment (Agilent 34970A). Interdigitated fingers of anode were connected during OCV measurement (Figure 5.3.a) and disconnected during biofilm imaging and impedance measurement (Figure 5.3.b). Polarization curves were obtained by varying the external resistor from 400  $\text{M}\Omega$  to 1  $\text{M}\Omega$ . Power ( $P$ ) was calculated by  $P=V^2 R^{-1}$  (Ohm's law) based on the recorded voltage ( $V$ ) and external resistor ( $R$ ). The current and power densities were normalized by the area of anode (0.8  $\text{mm}^2$ ).

#### **5.2.5. Biofilm imaging**

Biofilm imaging was performed by using Zeiss Axio Observer Z1 inverted microscope equipped with both Hamamatsu (used for GFP fluorescent images) camera.



**Figure 5.3.** Entire experimental setup a) Open circuit measurement b) Impedance measurements.

### 5.2.6. Impedance measurement

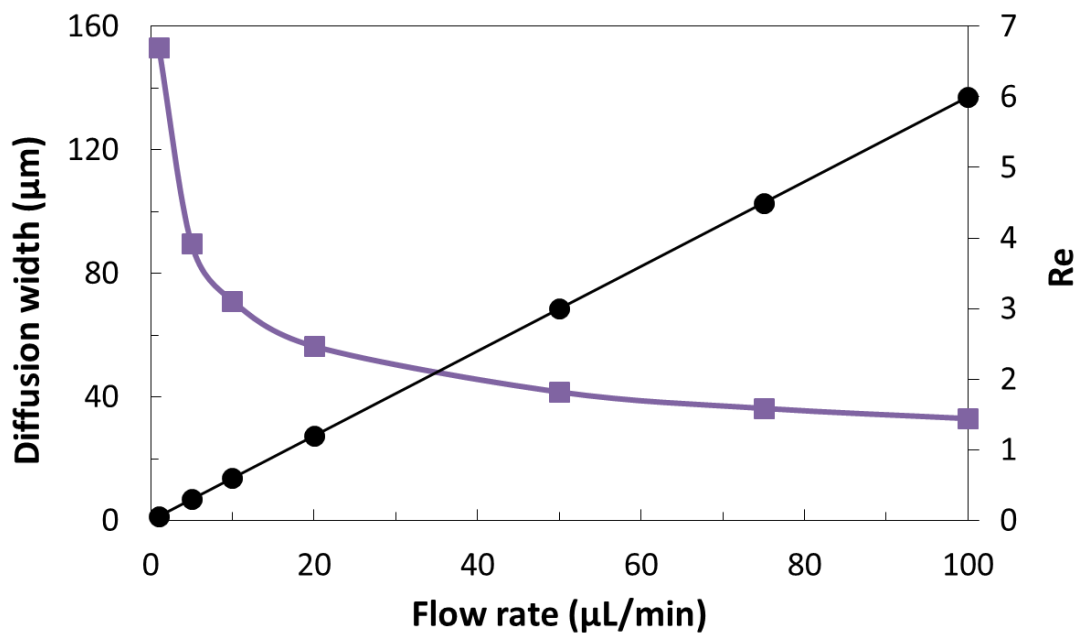
Impedance measurements were recorded using an impedance spectroscopy (HF2IS, Zurich Instruments) equipped with a current amplifier (HF2CA). A sweep frequency between 100 Hz and 100 kHz was applied to biofilm on the interdigitated electrodes with an amplitude of  $\pm 10$  mV. The interdigitated anode had 1 mm width and 4 mm length. It possessed 50 pairs of finger electrodes with 25  $\mu\text{m}$  width and 20  $\mu\text{m}$  space between fingers as seen in Figure 5.2.c. To perform the simulation, proper equivalent circuits were proposed, then data points were automatically selected by the software as inputs to the equivalent circuit to generate a fitting spectrum.

## 5.3. Results

### 5.3.1. Laminar flow characterization

The flow streams must be laminar to prevent turbulent mixing which provided by low Reynolds number ( $Re < 2100$ ),  $Re = \rho v D_h / \mu$ , where  $\rho$  is the density,  $v$  is the velocity,  $D_h$  is the hydraulic diameter of the channel, and  $\mu$  is the dynamic viscosity. Both anolyte and catholyte were maintained at the same flow rate (20  $\mu\text{L}/\text{min}$ ) which resulted low Reynolds number as shown in Figure 5.4 ( $Re = 1.21$ ). This result is well below to guarantee laminar flow in the microfluidic MFC. Observing the diffusion of both streams is also possible based on the flow rate. It can cause crossover mixing on the electrodes that affects biofilm growth on anode adversely. The maximum mixing region width ( $\delta_{\text{mix}}$ ) at the end of the microchannel is defined as  $(DHL/v)^{1/3}$ , where  $D$  is the diffusion coefficient,  $H$  is the height

of the microchannel, and  $L$  is the channel length.[108] Based on the calculation, mixing region width was  $56.4 \mu\text{m}$  in the device. (Figure 5.4) Since the gap between anode and the cathode was  $400 \mu\text{m}$ , the diffusion didn't have an impact on the biofilm growth. Fraiwan et al. design three electrode pairs placed closed to inlet, outlet and middle of the microchannel in laminar flow MFC.[109] Due to catholyte crossover on anode near outlet, the current production was lower than other electrode pairs. The electrode distance must be considered based on the diffusion width to prevent catholyte inhibition and electrolytes crossover.

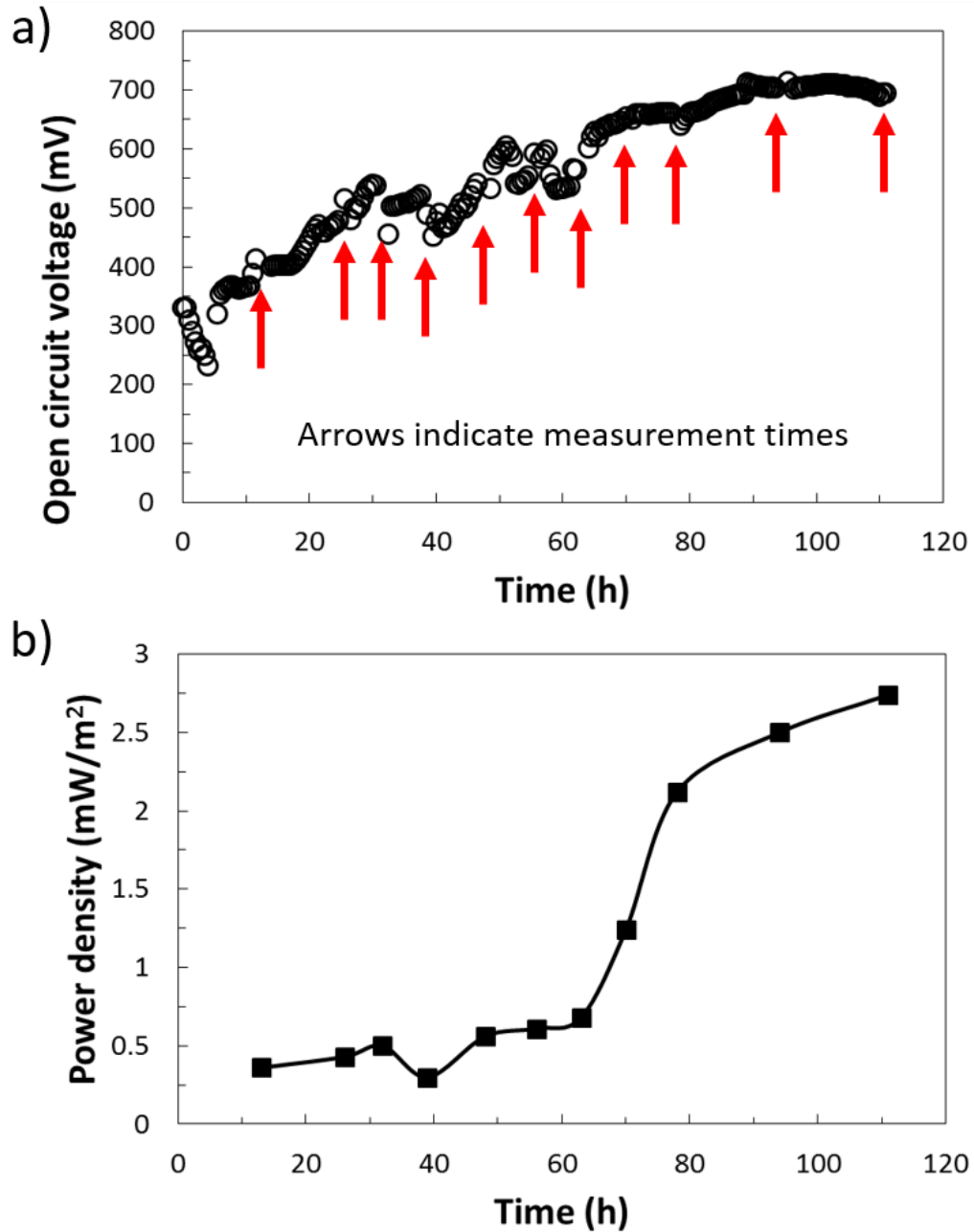


**Figure 5.4.** Diffusion width and Reynolds number values based the different flow rates.

### 5.3.2. Open circuit voltage and power generation from laminar flow MFC

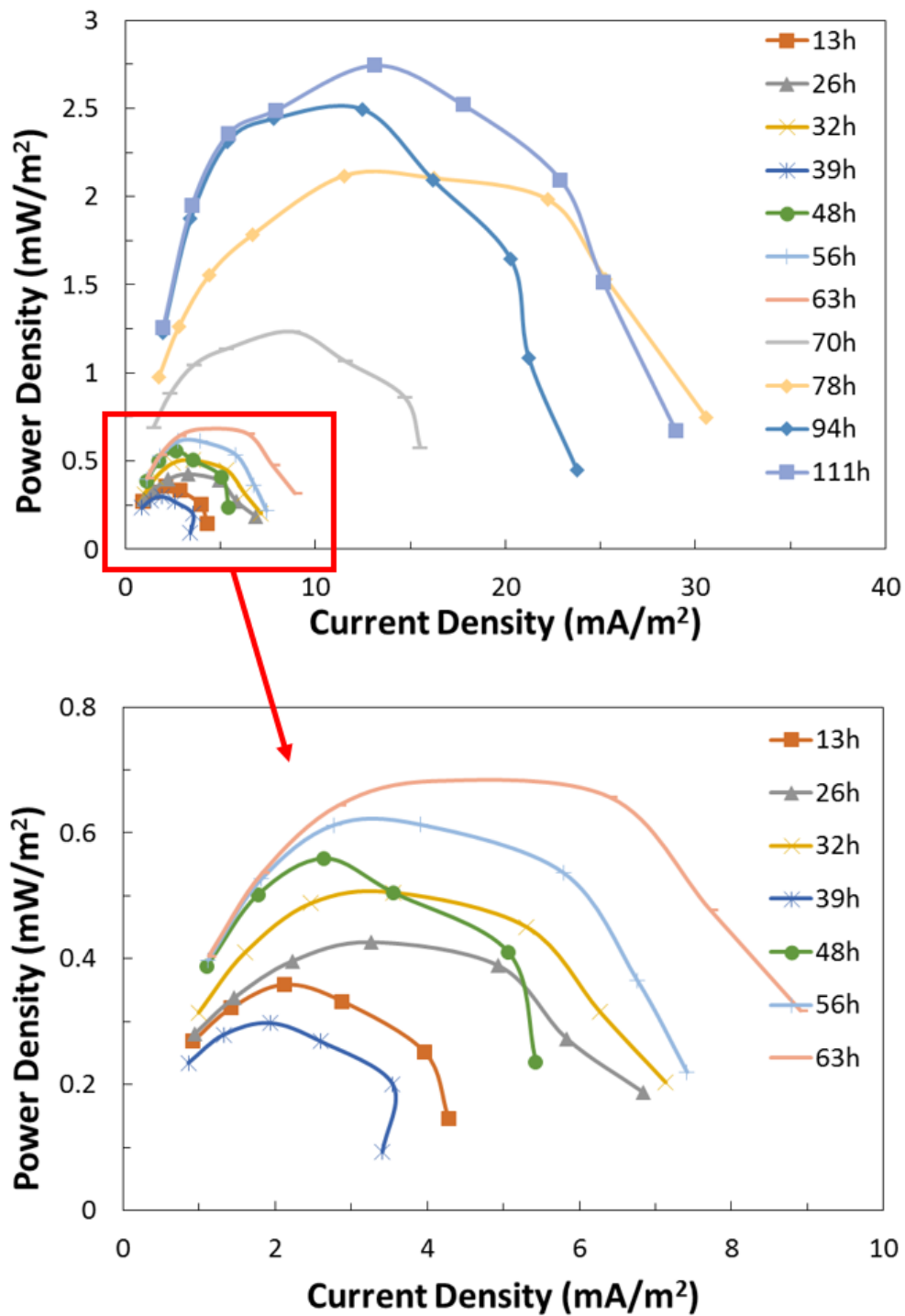
The performance of the laminar flow MFC was evaluated by measuring the open circuit voltage and obtaining the polarization curves at various time points. After initial growth of *S. oneidensis* MR-1 on anode, TSB was started to flow continuously for further biofilm growth and it resulted increasing on both open circuit voltage (Figure 5.5.a) and power density (Figure 5.5.b). The open circuit potential reached maximum around 700 mV in four days. Qian et al. measured it to ~600 mV in dual chamber micro scale MFC with separator in batch mode.[61] Furthermore, Fraiwan et al. obtained the open circuit voltages generated by same strain (*S. oneidensis* MR-1) were around 500 and 600 mV by using microfiber and carbon nanotube anode, respectively.[110] Vigolo et al. reported the highest open circuit potential measured to 770 mV in micro scale MFC (with membrane) that were inoculated with same bacteria.[111] The electrolytes were flowed in continuous mode ( $20 \mu\text{L min}^{-1}$ ) instead of batch-fed mode resulted in high performance. They also performed different flow rates (between  $0.5\text{-}60 \mu\text{L min}^{-1}$ ) to analyze the effect of flow rate on power density. It decreased sharply when the flow rate was higher than  $45 \mu\text{L min}^{-1}$  due to very high shear stress (3 Pa) which is unfavorable for biofilms and cause loosing or dispersing of them.[111, 112]



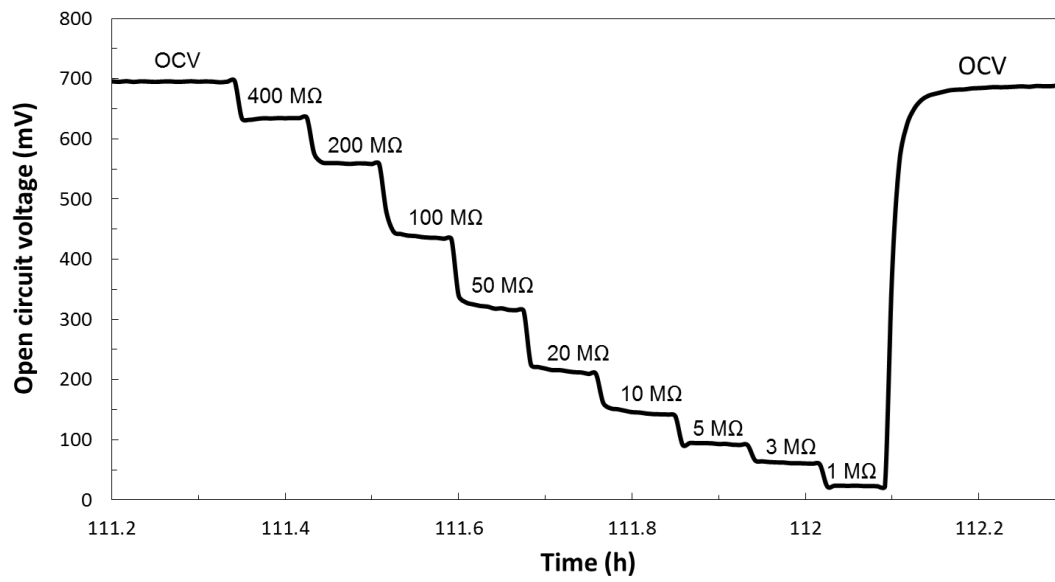


**Figure 5.5.** a) Open circuit voltage and b) Power density over time. Arrows indicated the measurement time points.

The power density in the laminar flow MFC gradually increased until ~60 hours from  $0.36 \text{ mW m}^{-2}$  to  $0.68 \text{ mW m}^{-2}$  then there was sharp increment and it reached to  $2.74 \text{ mW m}^{-2}$  at ~110 hour as shown in Figure 5.6. The voltage across each resistor were recorded after it was stable as shown in Figure 5.7 at ~110 hour. To our best knowledge, the power density was calculated first-time from the laminar flow MFC with gold electrode materials by inoculating single strain bacteria. Gold is the common electrode material in micro scale MFCs due to its biocompatibility, high conductivity properties as well as easy microfabrication processes. The performance of MFC with gold anode is lower than carbon based materials such as carbon cloth, carbon paper which provides better interaction between bacteria and the anode. However, they are not ideal in laminar flow MFC configuration since they have non-uniform shape and it is hard to place them. Qian et al. produced  $1.5 \text{ mW m}^{-2}$  from two chamber micro-sized MFC ( $1.5 \mu\text{L}$  anode volume) by having gold anode.[60] They used the same bacterial strain, anolyte (TSB) and catholyte (ferricyanide) solutions. Although, the power density is two times lower, its actual power generation is much higher than our laminar flow MFC. The power production is limited in laminar flow MFC since gold electrode materials provides high internal resistance. More importantly, oxygen can diffuse into the anode and it prevents efficient electron transfer from bacteria. Li et al. achieved a current density  $25.42 \text{ mA m}^{-2}$  from laminar flow MFC.[113] They didn't report the voltage data to calculate power density but the actual current was calculated to  $35 \text{ nA}$  which is very low compared to all other two chamber micro-sized MFCs.[62] Therefore, the laminar flow MFC is not ideal option for practical on-chip power applications.



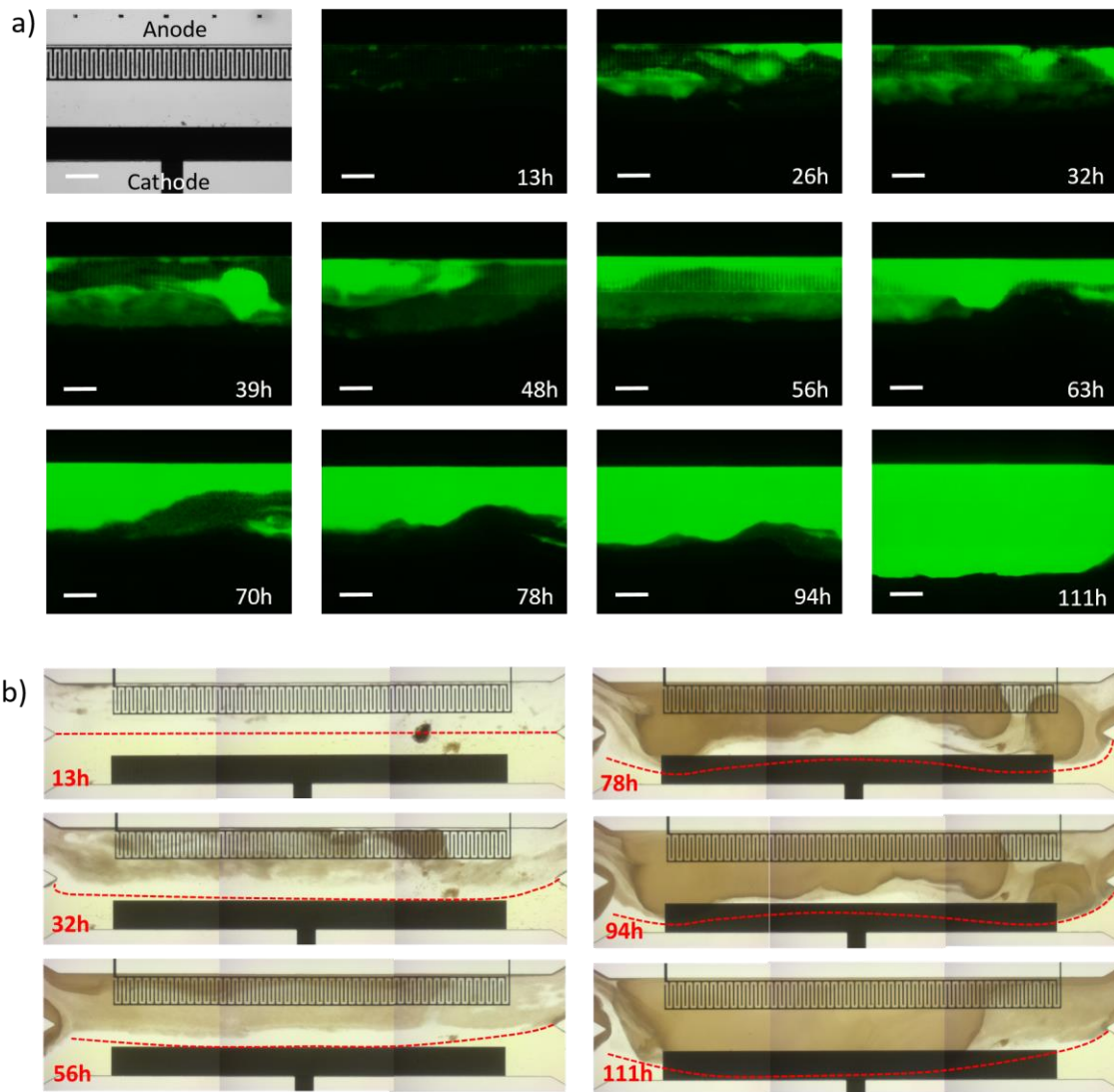
**Figure 5.6.** Power performance of the laminar flow MFC over time. The power density increased slowly until ~60 hours, then it doubled and continue to increase sharply.



**Figure 5.7.** Open circuit voltage generation from different resistors at 110 hour. After each change, the voltage production was stable.

### **5.3.3. Biofilm development on anode in laminar flow MFC**

In order to understand the performance, biofilm formation on anode was investigated under the fluorescence microscope. This experimental approach provided real time fluorescent images of the biofilm to show how it developed during power production which reflected the natural environment for the bacteria without disturbing with staining or taking it out from MFC chamber for imaging. Figure 5.8.a displays representative biofilm formation images in different time points. Attached bacteria and initial phase of the biofilm formation was started to observe around 12 hours. It continuously grew and became very uniform all over the anode by 55 hours. The power density was only increased 1.7-fold between these two time points. After that, the biofilm started to be thicker and larger until 110 hours which resulted in 4.5 and 7.6-fold higher power density compared to 55 and 12 hours, respectively. Biofilm development was previously studied with techniques such as SEM [23, 94], and confocal scanning laser microscopy [114] but it required removing the anode from MFC that resulted loss of viability during the fixing procedures to prepare the biofilm for imaging. The device used here not only produce electricity but also provided great tool to examine biofilm formation and development in situ. Furthermore, the flow streams of the electrolytes were observed with the bright field images. In the beginning of the laminar flow (12 hours), it was clearly seen that boundary layer was in the middle of the microchannel between the electrolytes. However, it started to move the cathode chamber side due to biofilm growth on the anode and the flow streams was not in parallel to each other anymore as shown in Figure 5.8.b. Nevertheless, it didn't affect the power production since the catholyte still flowed on cathode.



**Figure 5.8.** a) In situ biofilm development on anode over time. It gets thicker and larger after ~60 hours. b) Flow streams changing by the growth of biofilm in laminar flow MFC.

#### 5.3.4. Impedance measurement of biofilm on interdigitated anode

Bacterial attachment, and biofilm formation on the anode surface are crucial for the efficient biological transfer of electrons produced by the bacteria. In this study, we also used impedance spectroscopy to analyze the real-time biofilm activities on interdigitated anode and correlated the result with power production. The electrochemical impedance performance of the biofilm development was presented by an equivalent circuit model proposed in Figure 5.9. In this model, two identical double layer capacitance ( $C_{dl}$ ) were connected to the medium resistance ( $R_s$ ) in series, and biofilm capacitance ( $C_b$ ) and resistance ( $R_b$ ) was introduced in parallel with these series components. The total impedance could be expressed with the following equations.[115-117]

$$|Z_s| = \sqrt{R_s^2 + 1/(\pi f C_{dl})^2} \quad (5.1)$$

$$|Z_b| = \sqrt{R_b^2 + 1/(2\pi f C_b)^2} \quad (5.2)$$

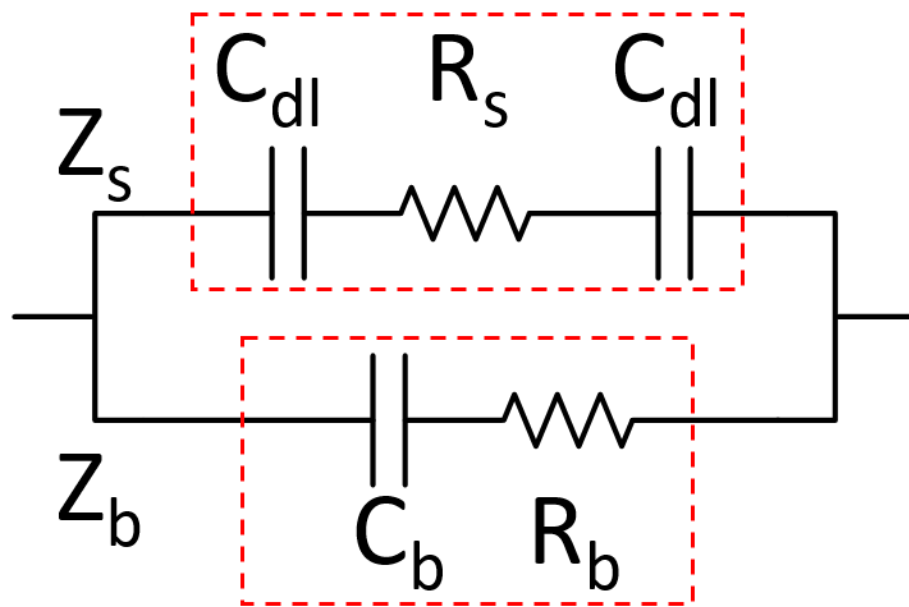
$$1/|Z| = 1/|Z_s| + 1/|Z_b| \quad (5.3)$$

where  $f$  is the frequency in Hz.

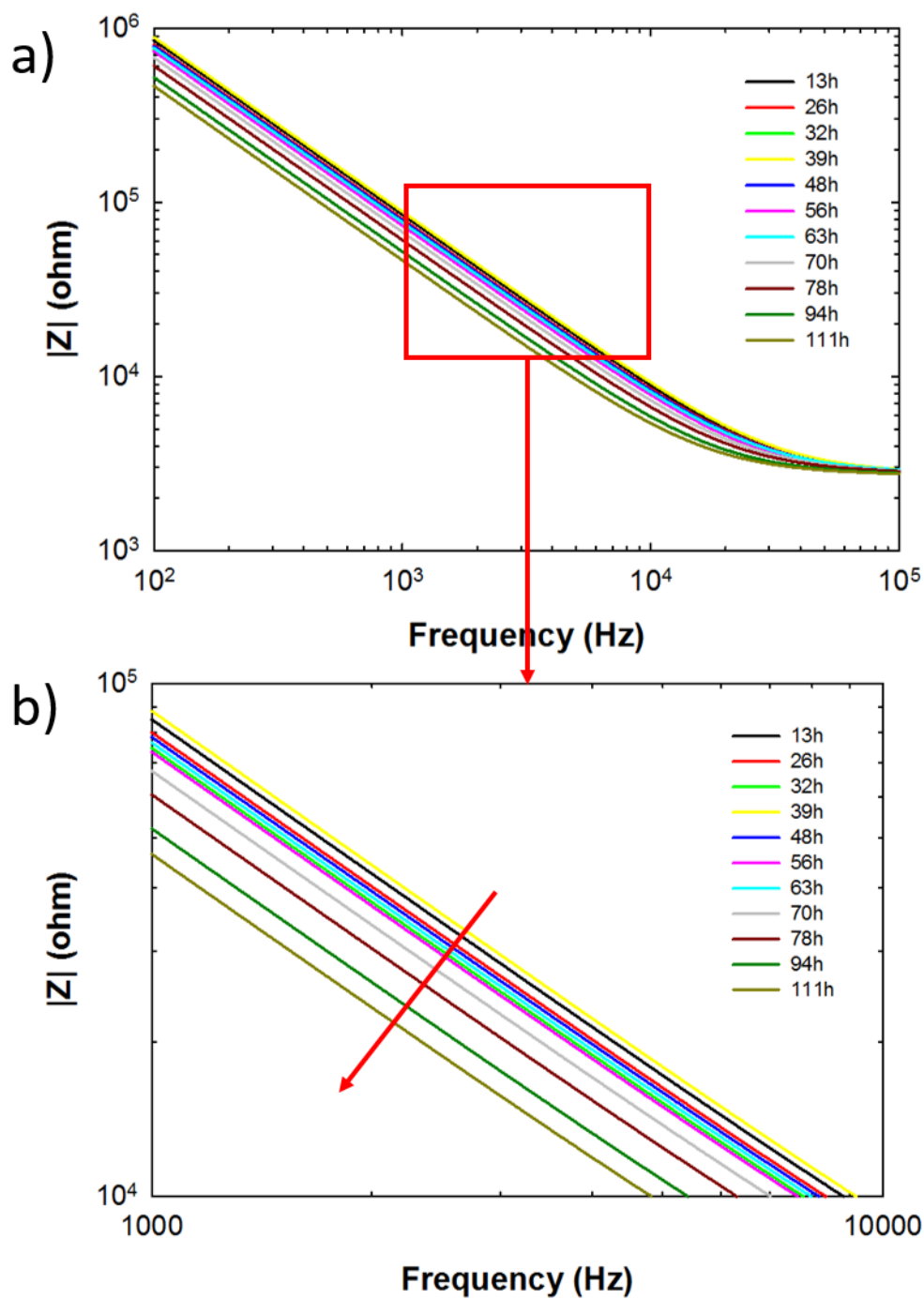
Continuous or repeatable impedance measurement without disturbing the biofilm growth over a period of time is advantageous in laminar flow MFC which allow us to obtain the impedance *in situ*. Figure 5.10.a and Figure 5.11.a shows the Bode plots of the biofilm on the interdigitated anode surface over a period of ~110 hours through the frequency range between 100 Hz and 100 kHz. The most obvious change was observed in the frequency range 3 kHz to 30 kHz, where both capacitance and resistance dominated the impedance response. The impedance magnitude and the phase decreased over time (Figure 5.10.b and 5.11.b). It might be directly related with biofilm development on the

anode surface. Larger and thicker biofilm at 110 h resulted in lower impedance compared to thin biofilm at 13 h. Impedance and power density correlation also showed that highest power density was obtained when the impedance and phase were lowest (Figure 5.11). Four different frequencies (5, 10, 25, 50 kHz) were selected to show how it changed. Both impedance and power density were not changed significantly until ~56 h, then they both changed greatly which was due to thicker biofilm observed at that time under the microscope.

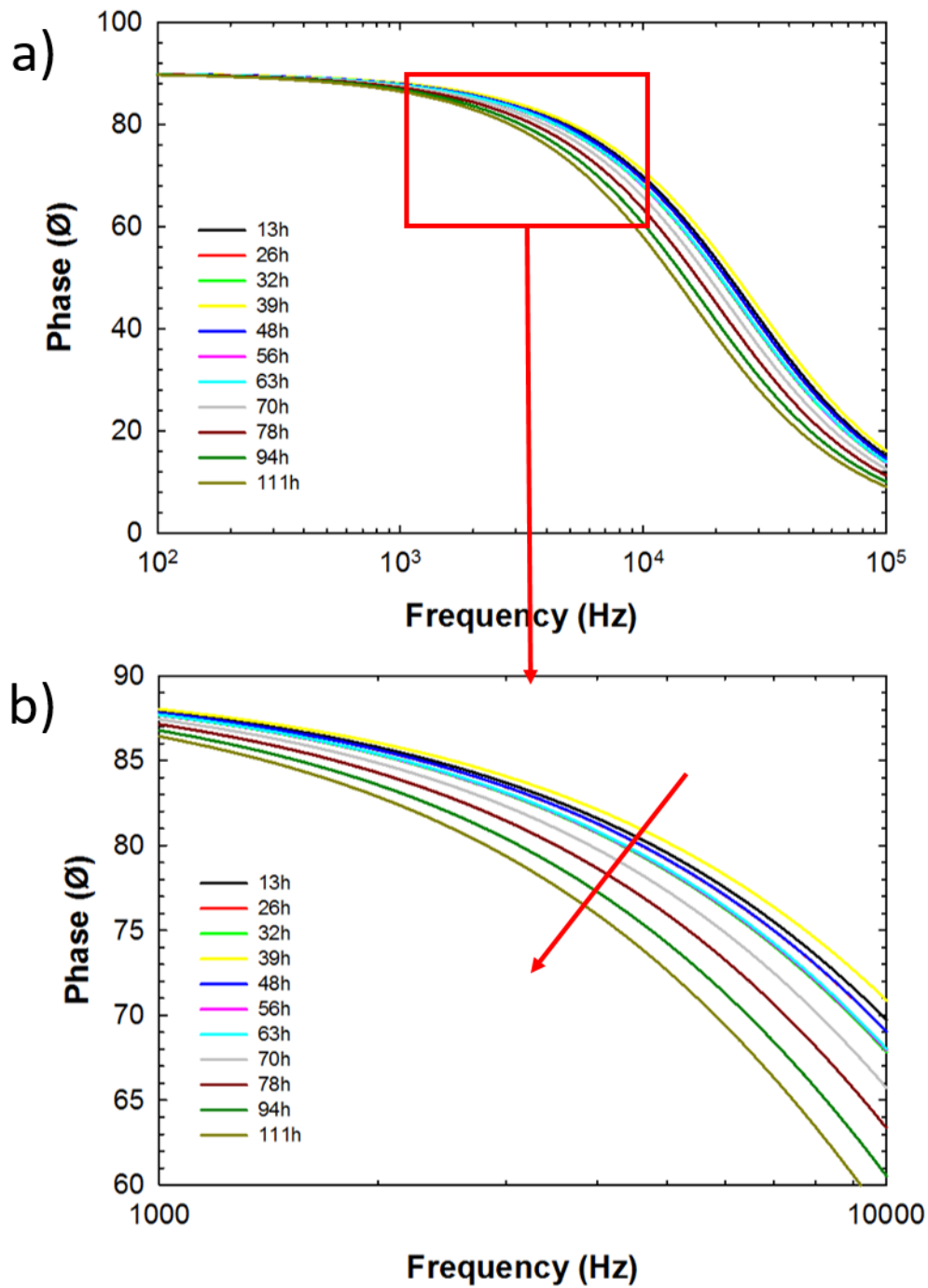




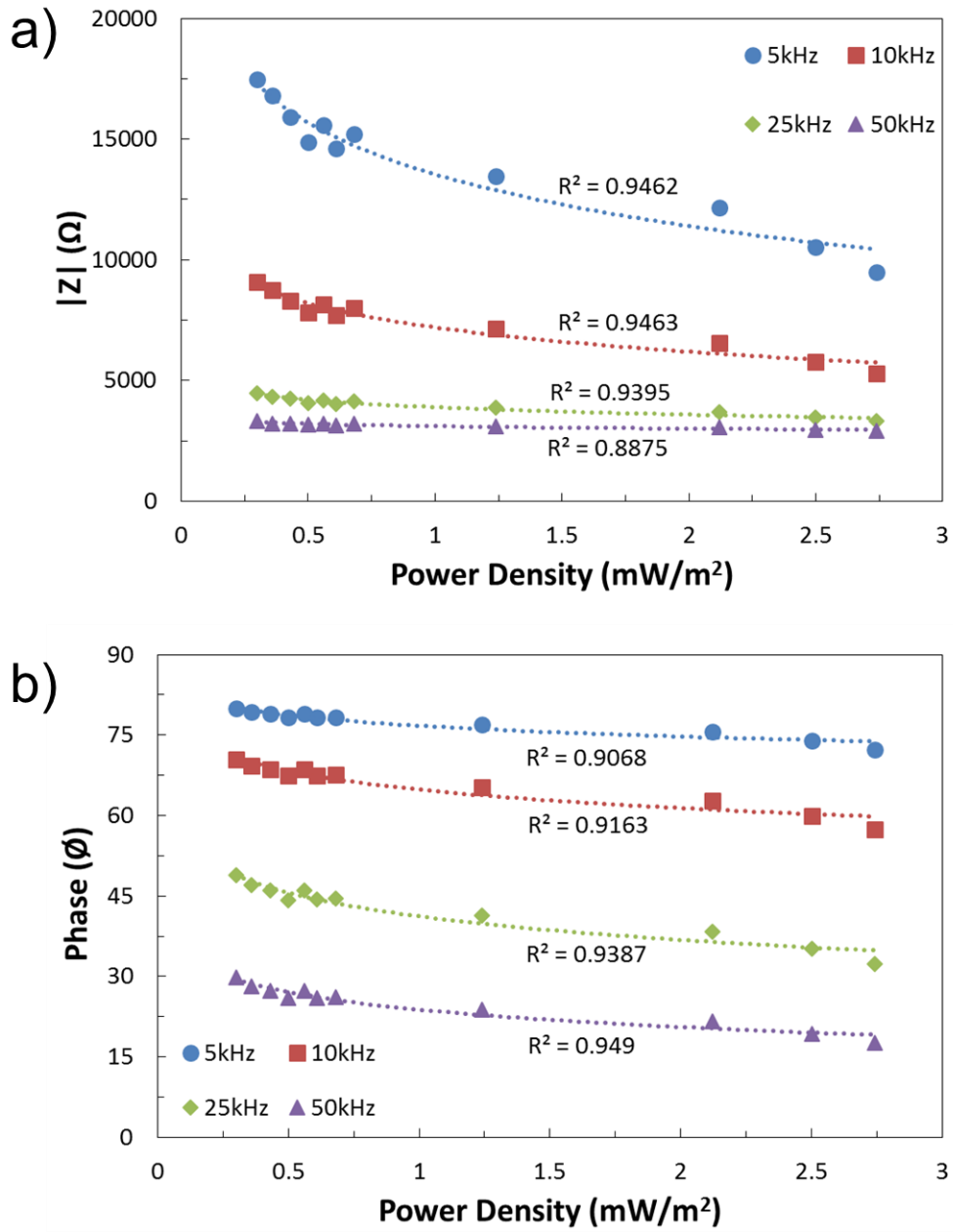
**Figure 5.9.** Electrical equivalent circuit of the biofilm impedance.



**Figure 5.10.** a) Impedance values between the frequency range of 100 Hz and 100 kHz. b) Impedance decreases over time by the growth of biofilm on interdigitated anode.



**Figure 5.11.** a) Phase values between the frequency range of 100 Hz and 100 kHz. b) Phase decreases over time.



**Figure 5.12.** a) Correlation between power density and impedance for different frequencies (5, 10, 25, 50 kHz) b) Correlation between power density and phase for different frequencies.

#### 5.4. Discussion

Developing new tools to understand the electron transfer mechanism in biofilm is essential for micro electrochemical cell systems and real-time biofilm imaging could help to find out relation between power production and biofilm development on anode. However, most studies have been done *ex situ* by taking out the anode to analyze under the microscope due to size of the MFC configuration which doesn't provide real time imaging.

Micro-sized devices could give better option due to their suitable small size for optical microscopes and transparent materials such as PDMS and glass. Franks et al. developed micro MFC for 3D real time imaging of the biofilm to monitor the inhibitory effects of proton accumulation and its effect on current production.[118] They successfully placed the MFC under the confocal scanning laser microscope to visualize biofilm in real time and accurately measured both pH gradients within the biofilm formed by *G. sulfurreducens* and the performance *in situ*. Mclean et al. reported the quantification of electron transfer rates for *S. oneidensis* MR-1 on anode surface in commercially available modified MFC and changes in the potential through the biofilm development stages.[119] Inglesby et al. also developed a photosynthetic MFC platform for fluorescence and electrochemical monitoring of an *Arthrospira maxima* biofilm.[120] The effects of the temperature and light intensity on the performance were demonstrated both optically and electrochemically in real time.

Existence of the membrane and complicated device configuration limited their usage therefore laminar flow MFC could be considered as an ideal device to analyze both power/current production performance and the biofilm development as well as

electrochemical activities simultaneously. The specifications and performance of the laminar flow MFC works reported to date were summarized in Table 3. Li et al. introduced the first laminar flow MFC and the current generation of *G. sulfurreducens* and *S. oneidensis* were compared.[113] SEM images of the anode was presented *ex situ* to show mature biofilm thickness at the end of the experiment. It was mainly considered as biological power device. Angenent et al. demonstrated the laminar flow MFC inoculated with *G. sulfurreducens* to monitor the effect of various chemical stimuli such as anthraquinone disulfide (AQDS), fumarate, riboflavin, pyocyanin on electrical current production and determined that AQDS is a good redox mediator for *G. sulfurreducens*.[104] Gupta et al. flowed anaerobic pathogenic bacteria (*Klebsiella pneumoniae*, Kp6) as anolyte and bacteriophage as catholyte to generate potential with their interaction.[121] Wang et al. obtained 246 mV by flowing microflora as anolyte to prove its electroactivity in laminar flow MFC.[105] They also compared the performance of different flow rates and found the maximum performance at 500  $\mu\text{L}/\text{min}$  where Re was 8.39. Fraiwan et al. used laminar flow MFC for real time visualization of the effects of electrolytes crossover on *G. sulfurreducens* biofilm.[109] They placed three electrode pairs through the microchannel and measured the highest current density from the electrode pair near inlets.

**Table 3.** Performance summary of previously reported laminar flow MFC works.

Inoculation	Anode area (mm <sup>2</sup> )	Total volume (μL)	Catholyte	Re	Flow rate (μL/min)	Performance	Ref.
<i>Geobacter sulfurreducens</i>	1.4	0.3	O <sub>2</sub> saturated PBS	4.62	45	18.4 mA/m <sup>2</sup>	[113]
<i>Shewanella oneidensis</i>	1.4	0.3	O <sub>2</sub> saturated PBS	4.62	45	25.42 mA/m <sup>2</sup>	[113]
<i>Geobacter sulfurreducens</i>	4	0.5	O <sub>2</sub> saturated PBS	0.2-1.1	1-10	2500 mA/m <sup>2</sup> <sup>a</sup>	[104]
<i>Microflora</i>	7.5	0.36	O <sub>2</sub> saturated PBS	8.39	500	246 mV OCV	[105]
<i>Klebsiella pneumoniae</i>	30	45	Phage	0.2-6	20-600	290 mV OCV	[121]
<i>Geobacter sulfurreducens</i>	0.85	0.72	Ferricyanide	3	50	65 mA/m <sup>2</sup>	[109]
<i>Shewanella oneidensis</i>	0.8	0.5	Ferricyanide	1.21	20	2.74 mW/ m <sup>2</sup>	This work

<sup>a</sup> Hydrogen was used as electron donor

## 5.5. Conclusion

A microfluidic laminar flow MFC without membrane was fabricated to monitor *S. oneidensis* MR-1 biofilm development *in situ*. Thick biofilm was started to visualize after 55 hours and the power density was also increased significantly after that time and reached  $2.74 \text{ mW m}^{-2}$  at 110 h. Also, the electrochemical impedance of biofilm was measured on interdigitated anode in real time. The result showed that decrease on impedance resulted in increase on power density. It can be explained with size of the biofilm which expanded by time. Laminar flow MFCs could be able to produce power however it is several fold lower than dual-chamber microscale MFCs. Therefore, it is not practical for on-chip power applications. Real time *in situ* imaging is essential to understand electron transfer mechanism in MFCs and it seems possible to visualize with laminar flow MFC which is ideal analytical tool to analyze both optical and electrochemical monitoring of biofilm development.



## **6. REAL-TIME H<sub>2</sub>/CH<sub>4</sub> MONITORING FROM MICROBIAL ELECTROLYSIS CELL WITH ZNO NANOWIRES BASED GAS SENSOR**

### **6.1. Motivation**

Microbial electrolysis cells are sustainable electrochemical devices that produce bio-hydrogen gas by applying external power [69] as shown in Figure 2.2.b. Produced gas in cathode is collected into gas bag that is connected to glass vial on cathode through needle. Gas chromatography is used for the gas analysis. The H<sub>2</sub> production rate can be reached 17.8 m<sup>3</sup>/d/m<sup>3</sup> in single chamber MECs [122]. The elimination of PEM significantly increase H<sub>2</sub> generation rate, but the produced H<sub>2</sub> is more likely consumed by methanogenesis to generate CH<sub>4</sub>. Real time gas analysis device is needed to detect both H<sub>2</sub> and CH<sub>4</sub> gases. ZnO nanowires are ideal for the gas detection, it responds the both hydrogen and methane gases. They are ideal materials to monitor the gas concentration in real time. Also, they can be easily fabricated with low cost.

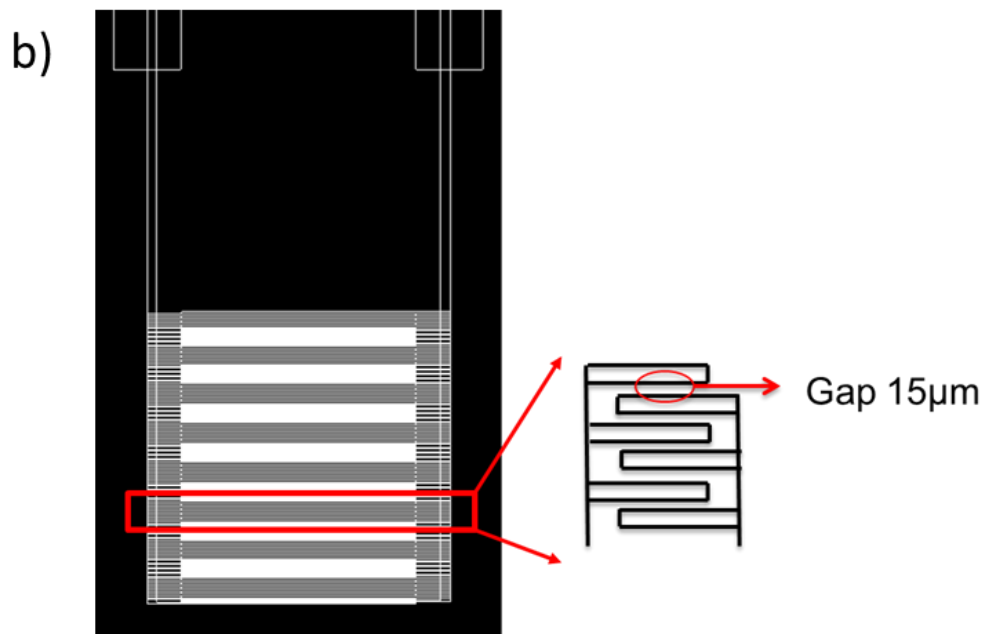
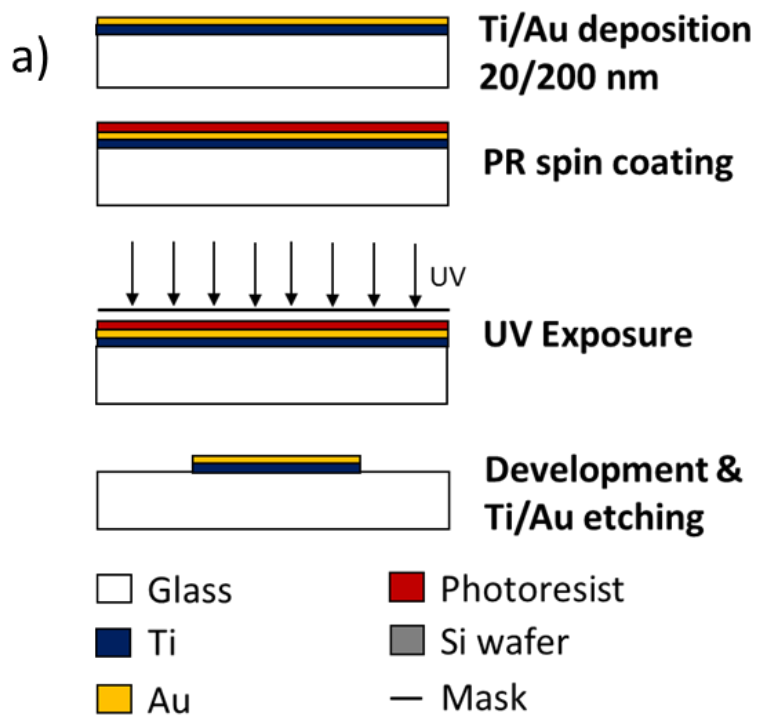
### **6.2. Hydrogen sensing mechanism**

The resistance-based sensing mechanism of ZnO is based on the variation of the surface electron depletion region due to the reaction between hydrogen and the chemisorbed oxygen on the surface [123]. Oxygen molecules in air can get adsorbed on the surface of the ZnO and extracts electrons to form oxygen ions. That creates an electron depletion region, which can greatly increase the resistance. When the sensor is exposed to a hydrogen, its molecules react

with the adsorbed oxygen species by releasing electrons which reduce the thickness of the depletion region, and decrease the resistance of the ZnO. An accumulation layer of electrons is created and results in a metalized region near the surface, which decrease the ZnO resistance.[116]

### **6.3. Device fabrication and nanowire alignment**

The electrode was fabricated with lithography process (Figure 6.1.a). Interdigitated electrode which has 95 fingers in each side as shown in Figure 6.1.b. ZnO nanowires were grown on Zn foil, then it was placed in glass vial having 1 mL IPA solution. The solution including Zn foil was sonicated for five seconds to disperse nanowires from foil. 100  $\mu$ L nanowire suspension was applied to interdigitated device (Figure 6.2.a) and nanowires were aligned by connecting function generator to device. Dielectrophoresis (DEP) method creates force on nanowires to align between each electrode fingers (Figure 6.2.b) [124]. Then the device was placed into furnace and strong connection between nanowires and electrode was achieved (Figure 6.2.c). Aligned nanowires can be seen in Figure 6.2.d and e.

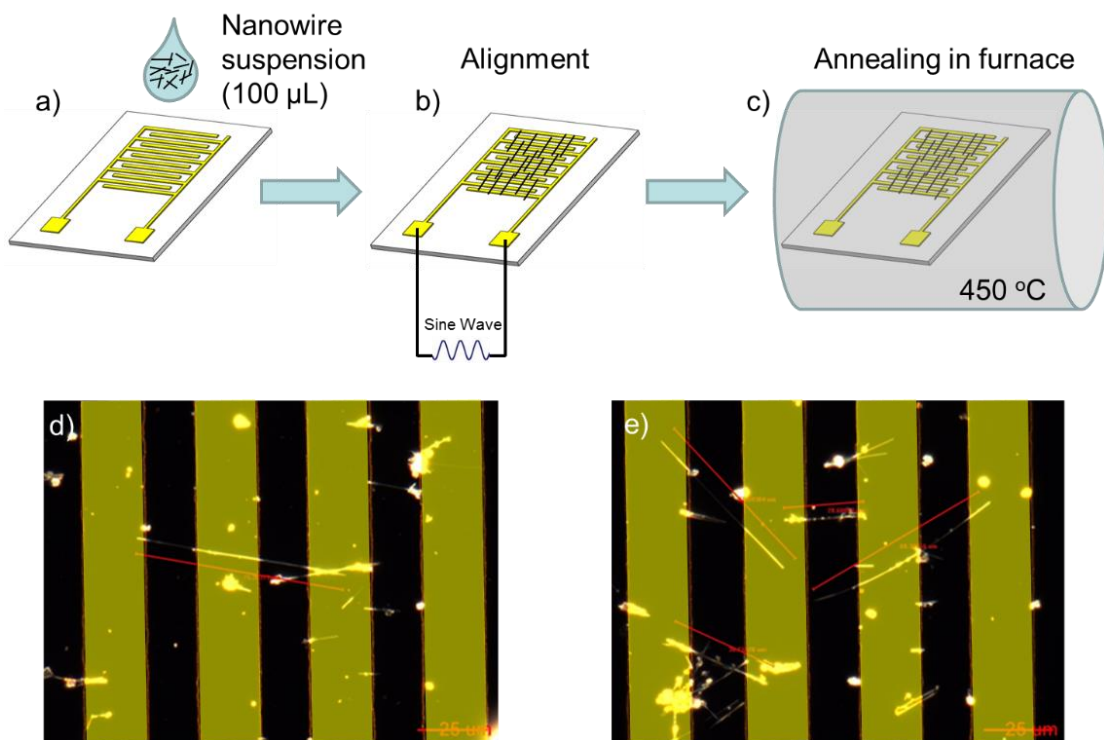


**Figure 6.1.** a) Photolithography and etching processes for fabrication of the gold electrodes. b)

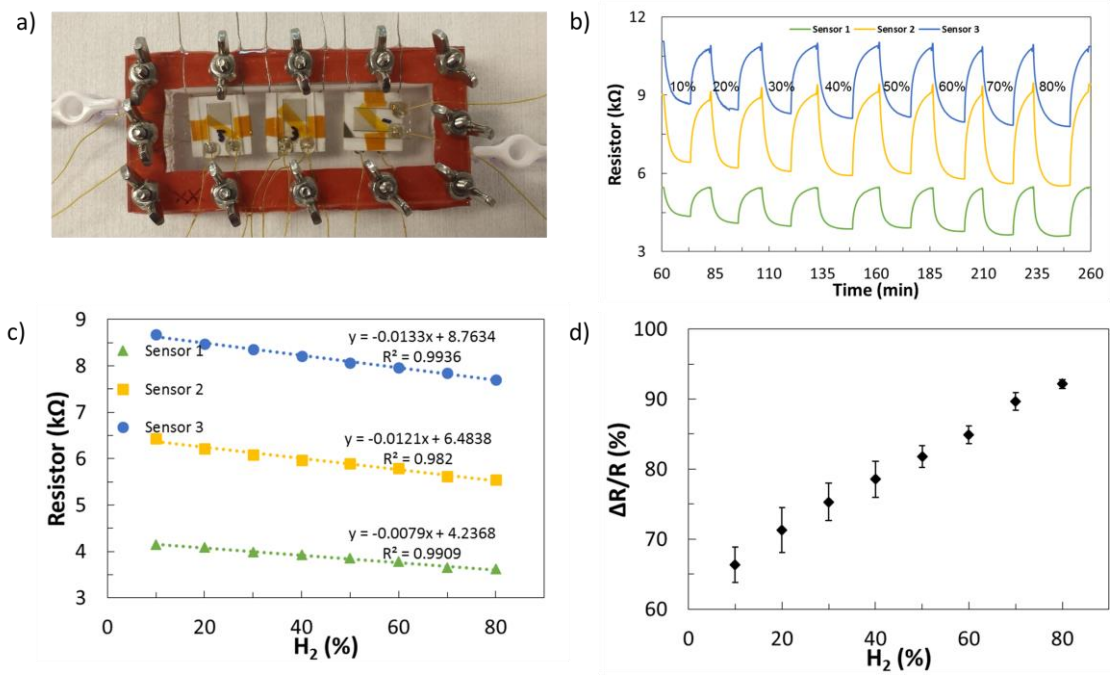
Top view of the gas sensor.

#### **6.4. Hydrogen gas calibration and measurement from MEC**

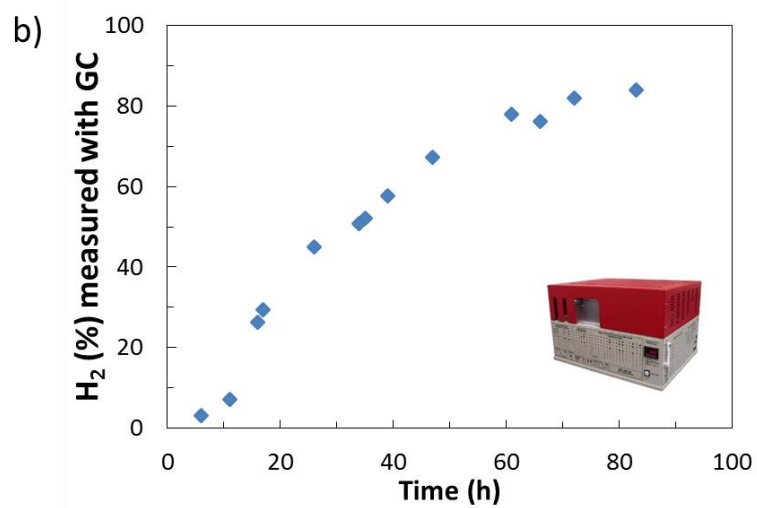
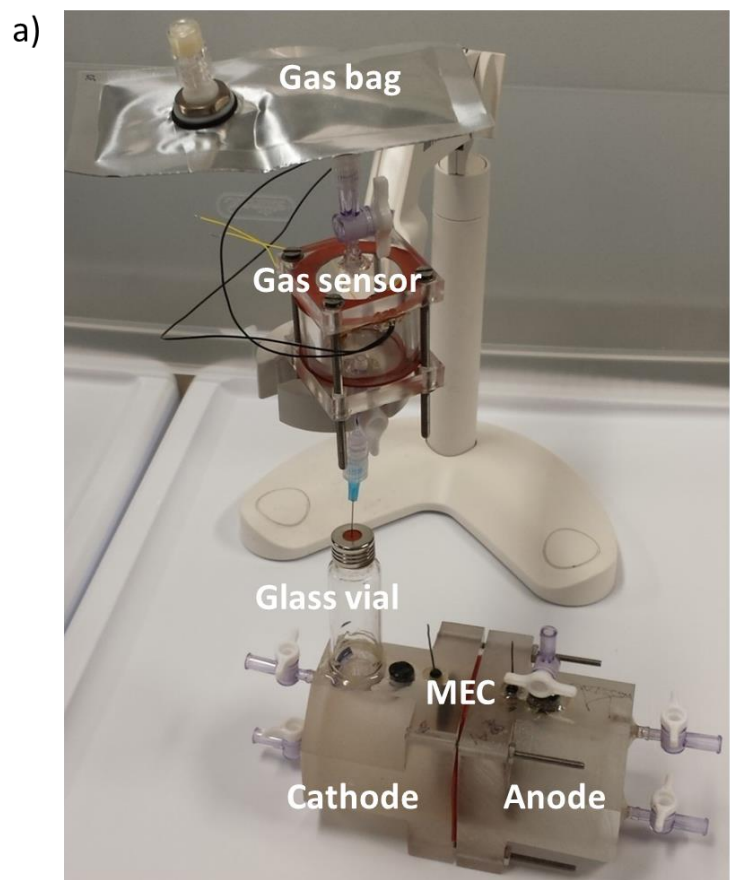
After multiple sensors were fabricated, they were placed into gas tight calibration chamber as shown in Figure 6.3.a. Heaters for the gas sensor were set to 200 °C then hydrogen gas with different concentration (between 10-99%) was connected into chamber to measure the resistor value from gas sensor. After each measurement, hydrogen gas was vacuumed to remove it from the chamber and next hydrogen gas was connected. Figure 6.3.b and Figure 6.3.c shows how the resistor value of the nanowires aligned on gas sensors change with different hydrogen gas concentration. Average percentage resistor change on sensors was shown in Figure 6.3.d. The resistor value of the sensors was linearly decreased with higher hydrogen concentration. The experimental setup was shown in Figure 6.4.a. First of all, hydrogen concentration was measured by using conventional method. The gas bag was connected to the MEC and hydrogen gas was accumulated in the bag. The hydrogen gas concentration was measured through gas chromatography (SRI 8610C) during ~80 hours as seen in Figure 6.4.b. It increased to ~80 % at the end of the cycle (substrate for bacteria in anode was depleted).



**Figure 6.2.** Sensor alignment processes. a) 10  $\mu\text{L}$  drop was applied, b) DEP method was used for nanowire alignment, c) Annealing process for strong connection between nanowires and gold electrode, d-e) aligned nanowires.



**Figure 6.3.** a) Gas calibration chamber. b) Resistor values of nanowires on the sensors with different hydrogen concentration. c) Equation and R-squared values of the sensors on linear trendline. d) Average percentage resistor change of the sensors.



**Figure 6.4.** a) Experimental setup, b) Hydrogen production measure by gas chromatography (SRI 8610C).

## **6.5. Conclusions and future work**

The hydrogen gas sensors were fabricated and calibrated. Hydrogen gas production from MEC over time was obtained with conventional method (using gas chromatography). The gas sensor will be tested with same MEC and it will be placed between MEC and gas bag. The produced gas will be collected in the gas bag and at the same time, the gas concentration value on the gas sensor will be measured to confirm it works same like conventional method.

ZnO nanowires based gas sensor was used to detect hydrogen gas but ZnO nanowires were not sensitive to methane in this work. Therefore, methane gas sensor will be fabricated by employing different nanowires such as SnO<sub>2</sub>, GaN which are sensitive to methane. After sensor fabrication, it will be calibrated by connecting different methane gas concentration to gas calibration chamber. It can be either used in MEC to detect methanogenesis or another type of fuel cell which converts CO<sub>2</sub> to methane.

Nanowire based gas sensors provide real time biogas measurement device which is easy to detect methanogenesis in MEC applications when it starts to occur. It doesn't require any expensive and labor intensive equipment such as gas chromatography. Fabrication cost of the sensor device is only a few dollars which provides low cost gas sensor device. It has great potential with broad applicability to microbial electrochemical cell systems.



## 7. HIGH PERFORMANCE MONOLITHIC POWER MANAGEMENT SYSTEM WITH DYNAMIC MAXIMUM POWER POINT TRACKING FOR MICROBIAL FUEL CELLS\*

### 7.1. Introduction

Microbial fuel cells (MFCs) use electrochemically active bacteria (EAB) to convert organic substrates such as wastewater into electrical energy, and have been considered as a clean and promising renewable energy generation source.[13, 125, 126] However their low power output per anode electrode surface area (100 - 2000 mW/m<sup>2</sup> at maximum power point (MPP)) and low voltage output (300 - 600 mV at MPP) make it difficult to directly power most electrical systems.[87] Fluctuating voltage and power level over time is another challenge for maximizing power extraction from MFCs. Large-scale MFCs can be built to overcome the low-power generation problem, however power output typically do not improve linearly due to scaling up issues[127], and the low-voltage problem still persists. Connecting multiple MFCs in series has been demonstrated to increase the output voltage, however voltage reversal problems over time make such strategy inefficient beyond connecting about 2 - 3 MFCs in series, still limiting the voltage level that can be achieved.[53] Direct connection of capacitors in parallel or series to the MFC has been also tried, but this method does not allow dynamic matching of MFC internal resistance

---

\* Reprinted with permission from “High Performance Monolithic Power Management System with Dynamic Maximum Power Point Tracking for Microbial Fuel Cells” by Celal Erbay, Salvador Carreon-Bautista, Edgar Sanchez-Sinencio, and Arum Han, 2014. *Environmental Science & Technology*, 48 (23), 13992-13999, Copyright [2014] by American Chemical Society.

( $R_{MFC}$ ) and input impedance ( $Z_{in}$ ) for maximum power extraction, and thus is inherently inefficient.[128]

The use of power management systems (PMS) are probably the most promising strategy in extracting maximum power from MFCs, as well as boosting the MFC output voltage level to a directly usable level.[129-137] PMSs are capable of increasing the MFC output voltage to an adequate level typically using DC-DC boost converter circuits [129-134] or charge pump circuits [135-137]. Such PMSs are commonly used in energy harvesting systems that generate low levels of power and voltage, such as for thermoelectric energy harvesting systems [138-140] and vibrational-energy harvesting systems.[141-143] For MFCs, charge pump circuits have been used as a voltage booster.[135-137] However, they require high MFC output voltage ( $\sim 600$  mV) to directly operate the charge pump efficiently due to its current limitation[133], and the charging/discharging times are typically very long (more than 10 times) compared to boost converter.[136, 137] DC-DC boost converters can overcome these limitations, and have been successfully integrated into PMSs managing MFC power.[129-134]

However most PMSs used for MFC power management lack dynamic maximum power point tracking (MPPT) capabilities that allow continuously matching the load impedances of the PMSs to extract maximum power from MFCs, an important feature for MFCs as their power output typically changes over time. Woodward et al. showed that more than 50% of power may be lost across the internal resistance of an MFC if the load impedance is not matched.[144] An MFC can be viewed as a voltage source with internal resistance and capacitance ( $\sim 160$   $\mu$ F). All three parameters (voltages, internal resistance,

and internal capacitance) can change over time due to biofilm growth and fluctuations in operating conditions such as pH, temperature, and carbon substrate concentrations.[145, 146] Thus, dynamically tracking the MPP is an essential scheme in PMSs for MFCs to maximize the power extraction efficiency. Wang et al. has presented an MPPT scheme for MFCs, however their system is composed of multiple external and discrete components that requires external power to operate the PMS itself, resulting in low efficiency.[133] Yang et al. demonstrated an integrated circuit (IC) PMS, however due to the lack of MPPT feature, resulted in low system efficiency (4.29%) and long charging time (~2.3 hours) of the super-capacitor used in the PMS.[133] A super-capacitor, also known as ultra-capacitors or electric double layer capacitors, is an electrochemical capacitor and possesses a much higher capacitance value compared to conventional capacitors. Super-capacitors have much shorter charge/discharge cycles than rechargeable batteries, and can also tolerate more charge/discharge cycles.[147] These features make super-capacitors ideal for energy-harvesting systems, and thus will be used in our application to store energy harvested from MFCs through the PMS.

Here, highly efficient boost converter circuit was presented with an MPPT scheme that can continuously detect the MPP of the MFC and match the load impedance of the PMS without using any external resistors by dynamically modulating the switching frequency of the boost converter and thus minimizing the time and power consumption for MPPT. The PMS circuit was fabricated in 0.5  $\mu\text{m}$  CMOS technology, making this monolithic PMS IC chip system extremely power efficient so that the PMS could be operated using only the power from the MFC itself. Using this PMS and a super- capacitor,

maximum energy was extracted at all times at an elevated voltage of 2.5 V, and was successfully used to periodically run a wireless temperature sensor.

## 7.2. Materials and methods

### 7.2.1. Power management system (PMS)

The PMS implemented here is an integrated synchronous DC-DC boost converter circuit in 0.5  $\mu\text{m}$  CMOS technology, with dynamic MPPT capabilities (Figure 7.1). The boost converter block steps up the input voltage ( $V_{in}$ ) from the MFC to a higher output voltage ( $V_{out}$ , set to 2.5 V here), where the output voltage ( $V_{out}$ ) charges a 100 mF super-capacitor ( $C_{super}$ ) until it has sufficient power to operate a wireless temperature sensor. The MPPT block continuously measures 1/2 of the MFC open circuit voltage ( $1/2 V_{MFC}$ ) and uses this information to control the switching frequency of the boost converter to match the load impedance ( $Z_{in}$ ) of the PMS to be equal to the internal resistance of the MFC ( $R_{MFC}$ ), thus assuring maximum power transfer. Details can be found on our published journal articles. (2 references that we published)

### 7.2.2. PMS system efficiency

The overall system efficiency of the PMS ( $\eta$ ) was calculated based on the ratio of the output energy stored on the super-capacitor ( $E_{out}$ ) and input energy generated by the MFC ( $E_{in}$ ), as shown in the following equations (7.1-7.4):

$$E_{out} = \frac{1}{2} \times C_{super} \times V_C^2 \quad (7.1)$$

$$E_{in} = P_{MFC} \times T_{MFC} \quad (7.2)$$

$$P_{MFC} = V_{MFC}^2 / 4R_{MFC} \quad (7.3)$$

$$\eta = \frac{E_{out}}{E_{in}} \times 100 (\%) \quad (7.4)$$

where  $C_{super}$  is the capacitance of the super-capacitor (a 100 mF super-capacitor was used here),  $V_C$  is the voltage on the super-capacitor,  $P_{MFC}$  is the maximum power from the MFC, and  $T_{MFC}$  is the time duration. The voltage across the super-capacitor ( $V_C$ ) and across the MFCs were recorded using an oscilloscope (DS1104B, Rigol Technologies Inc.).

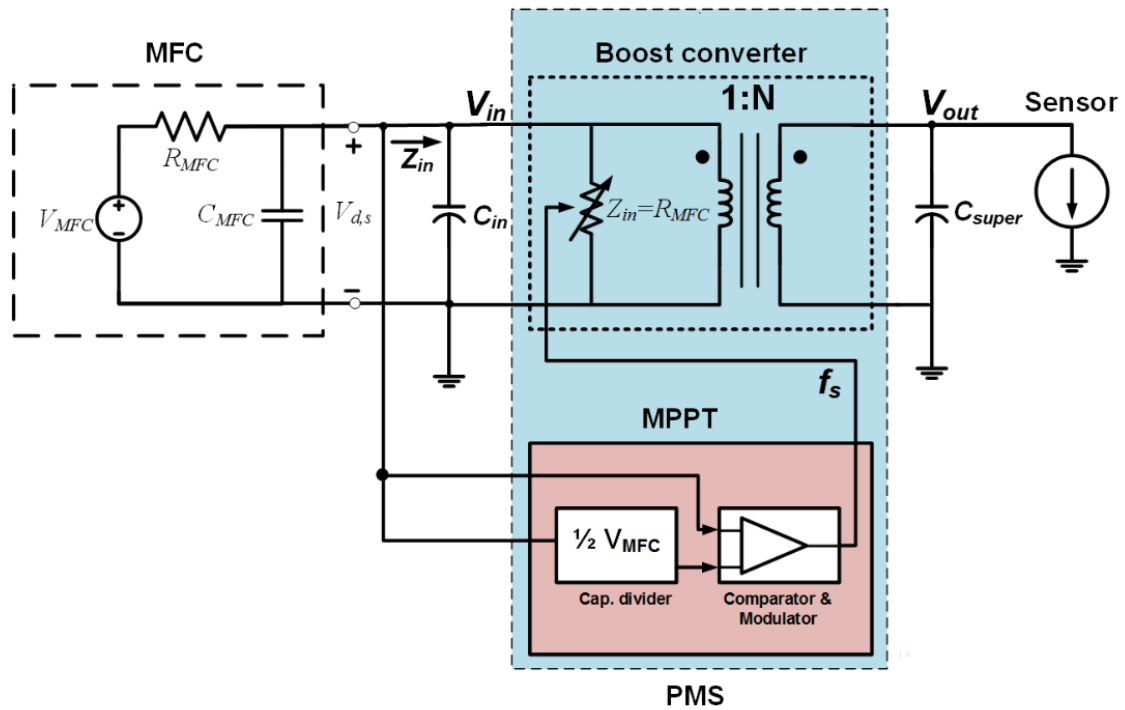
The overall system efficiency strongly depends on the amount of power extracted from the MFC. The more power available, the lower the MFC internal resistance and lower MFC internal capacitance. Since the converter typically operates in steady state, the MFC capacitance does not come into consideration.

### **7.2.3. Using the PMS-controlled MFC to power a wireless temperature sensor**

The developed PMS controlling the MFC power/voltage output was tested to power a wireless temperature sensor (Monnit, Inc.) that uses a thermistor to accurately measure the temperature. The wireless temperature sensor required an operating voltage of 2 - 3.6 V (900 MHz operating frequency for wireless transmission) and power of 85 mW. The on-board lithium battery was removed before testing so that the sensor was powered completely by the PMS-controlled MFC itself. The measured temperature is transmitted to a base station up to 250 feet away. The receiver base station was connected to a laptop computer.

#### **7.2.4. MFC construction and operation**

A two-chamber MFC was constructed from two 120 ml acrylic chambers separated with a PEM (Nafion 117<sup>TM</sup>, Ion Power Inc.). Carbon felt (Morgan, UK) was used as the anode (3 × 4 cm) and carbon cloth with Pt catalyst on one side (10wt% Pt/C, 0.5 mg Pt/cm<sup>2</sup>, ElectroChem, Inc.) was used as the cathode (3 × 4 cm). The anode chamber was inoculated with an anaerobic activated sludge (Austin Wastewater Plant). Autoclaved anaerobic nutrient mineral buffer (NMB, pH 7.0) solution[80] with acetate (1 g/L) was used as the carbon substrate containing media. To be able to test the developed PMS with MFCs showing different power output level, two MFC configurations were used. For the low-power output MFC (LPMFC) configuration, the cathode chamber was filled with phosphate buffer solution (PBS) (100 mM, pH 7.0) and continuously sparged with air. For the high-power output MFC (HPMFC) configuration, the catholyte was replaced with potassium ferricyanide (100mM) to generate higher power. During the startup phase, the MFC was connected with an external resistor (1 k $\Omega$ ) and the voltage across the resistor was monitored through a multiplexer (National Instruments) for continuous voltage measurements via a LabView<sup>TM</sup> (National Instruments) interface.[55, 57, 87] Polarization curve was obtained by varying the load resistances (100  $\Omega$ -10 k $\Omega$ ).



**Figure 7.1.** Proposed PMS for managing MFC power composed of a DC-DC boost converter block and a MPPT block. The circuit is designed by Salvador Carreon from Prof. Edgar Sanchez-Sinencio's research group at Texas A&M University [95].

### 7.3. Results

#### 7.3.1. PMS correctly determines maximum power point (MPP) of the MFC

The polarization curve from the LPMFC after 6 months of operation showed a maximum power output of 328  $\mu\text{W}$  at a current of 0.9 mA and a voltage of 360 mV (open circuit voltage of 720 mV) (Figure 7.2.A). The maximum power from the HPMFC was 512  $\mu\text{W}$  at a voltage of 400 mV (open circuit voltage of 800 mV) (Figure 7.2.B). This is in line with a typical two-chamber MFC power performance when using wastewater inoculum and acetate as the carbon substrate.[148, 149] These two MFCs were used to test how the developed PMS performs at two different MFC voltage and power levels.

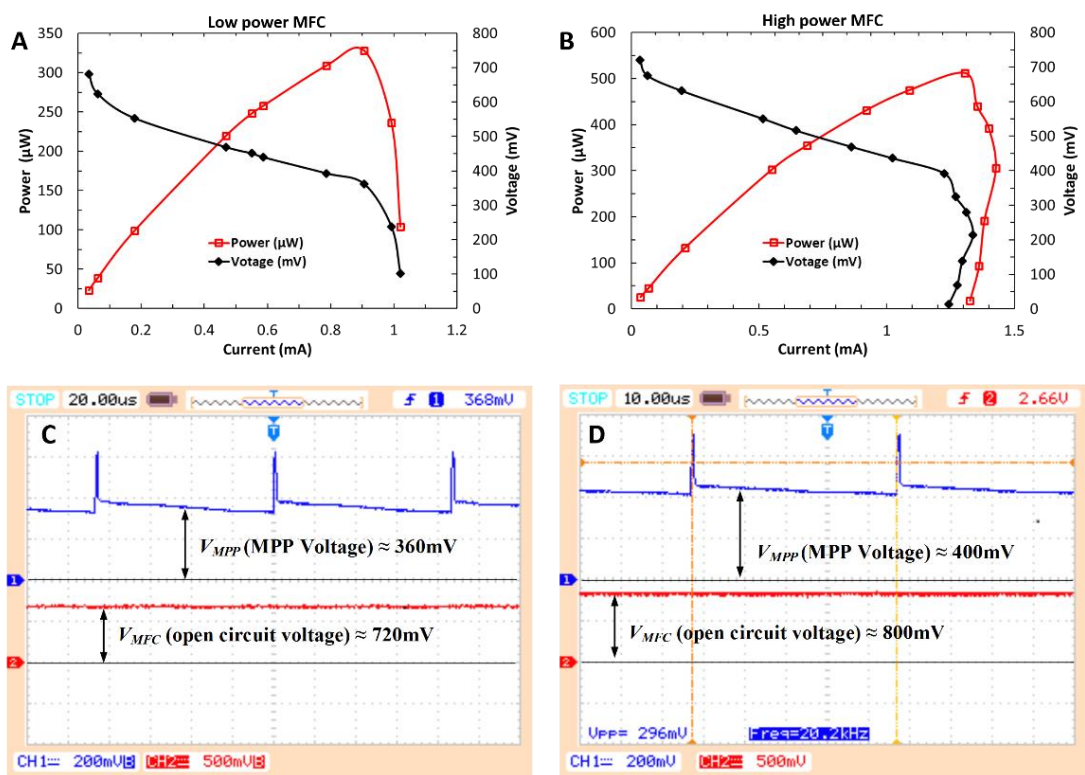
The PMS circuit successfully identified the output voltage of the LPMFC at maximum power point as 360 mV ( $V_{MPP}$ ), which was half of the LPMFC open circuit voltage (Figure 7.2.C). This identified voltage was same as the MPP voltage obtained through a polarization curve that required varying the load resistors to find the MPP. The same successful result was accomplished when connecting the PMS to the HPMFC, which detected the correct  $V_{MPP}$  of 400 mV through the PMS circuit (Figure 7.2.D). The screenshots show the MPPT capabilities of obtaining  $V_{MPP}$  when no load demand (PMS off) on the MFC is present. Once the PMS begins to extract power, the periods for  $T_x$  of 1.8 seconds and sampling periods of 200 ms are externally set through the one-shot circuit. The sensing period was made by setting a maximum ratio of disconnection to extraction period to no greater than 1/8. This limit would allow for minimum disruption on the power extraction from the PMS towards the MFC. Larger ratios would be possible but more



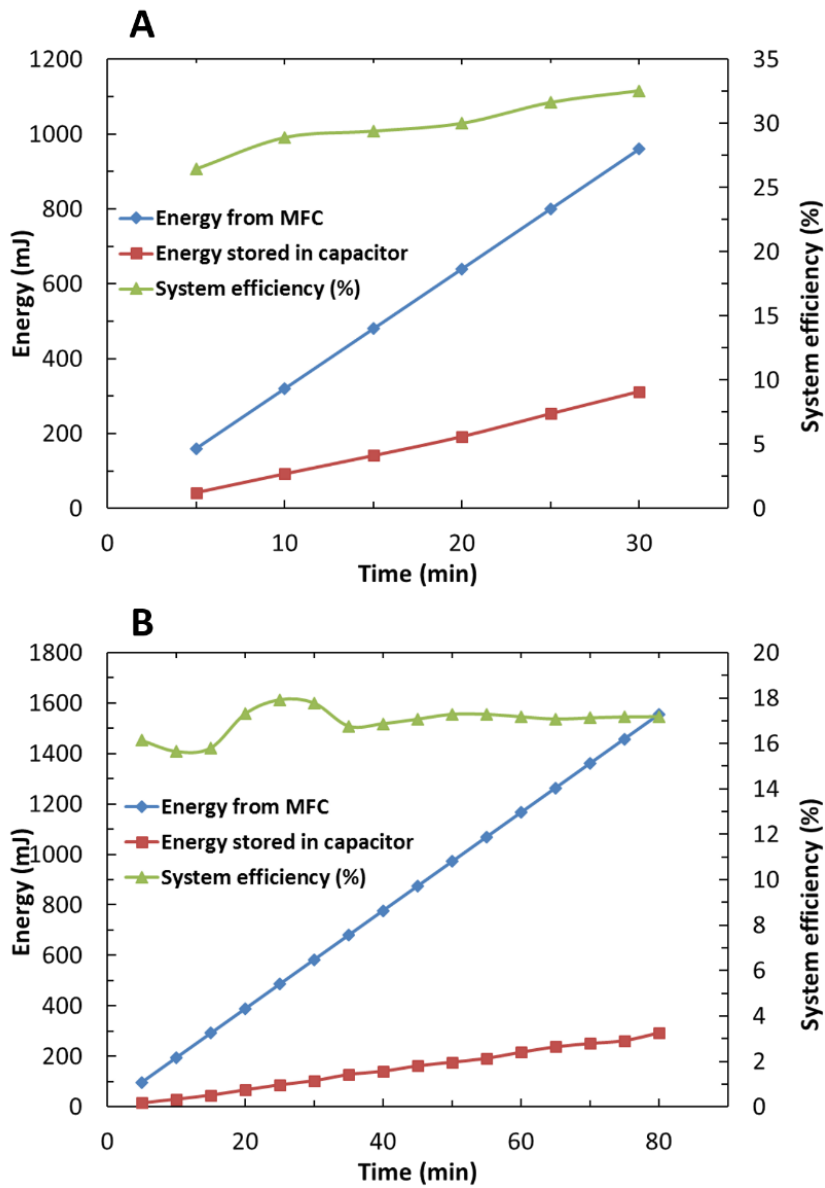
considerations would have to be taken on sampling capacitor charge leakage and input buffer capacitor size. The developed MPPT function of the PMS continuously refreshes and corrects the optimum operating point for maximum power extraction, while minimizing power consumption. Thus, this dynamic MPPT scheme would be able to take into account any power variations of the MFC over time, resulting in maximum power efficiency.

### **7.3.2. Overall system efficiency of the PMS**

The overall system efficiency ( $\eta$ ) is an important indicator to show the performance of the PMS and how much energy from the MFC is lost in the PMS circuit. The input energy ( $E_{in}$ ) from the MFC and the output energy stored in the super-capacitor were measured over time until the voltage of the super-capacitor reached 2.5 V. When using the HPMFC (512  $\mu$ W), the super-capacitor was charged to 2.5 V in 30 minutes and the average system efficiency was 30% over time (Figure 7.3.A). System efficiency was slightly lower in the beginning due to the slow charging of the super-capacitor during the initial dynamic MPPT detection, however after detecting the MPP, increased over time and reached 33%. When using the LPMFC producing 328  $\mu$ W, the system efficiency was 17% and the super-capacitor charging time to 2.5 V was initially 87.5 minutes (Figure 7.3.B). In general, the PMS system efficiency has a direct correlation to the power output level, and thus higher system efficiencies were observed when the power output of the MFCs were higher.



**Figure 7.2.** (A) Polarization curve obtained from the low-power MFC (LPMFC), showing power output of 328  $\mu\text{W}$  and voltage output of 360 mV at MPP. (B) MPP voltage of 360 mV was successfully detected by the PMS when connected to the LPMFC having an open circuit voltage of 720 mV. (C) Polarization curve obtained from high-power MFC (HPMFC), showing power output of 512  $\mu\text{W}$  and voltage output of 400 mV at MPP. (D) MPP voltage (400 mV) was detected by the PMS when connected to the HPMFC having an open circuit voltage of 800 mV.

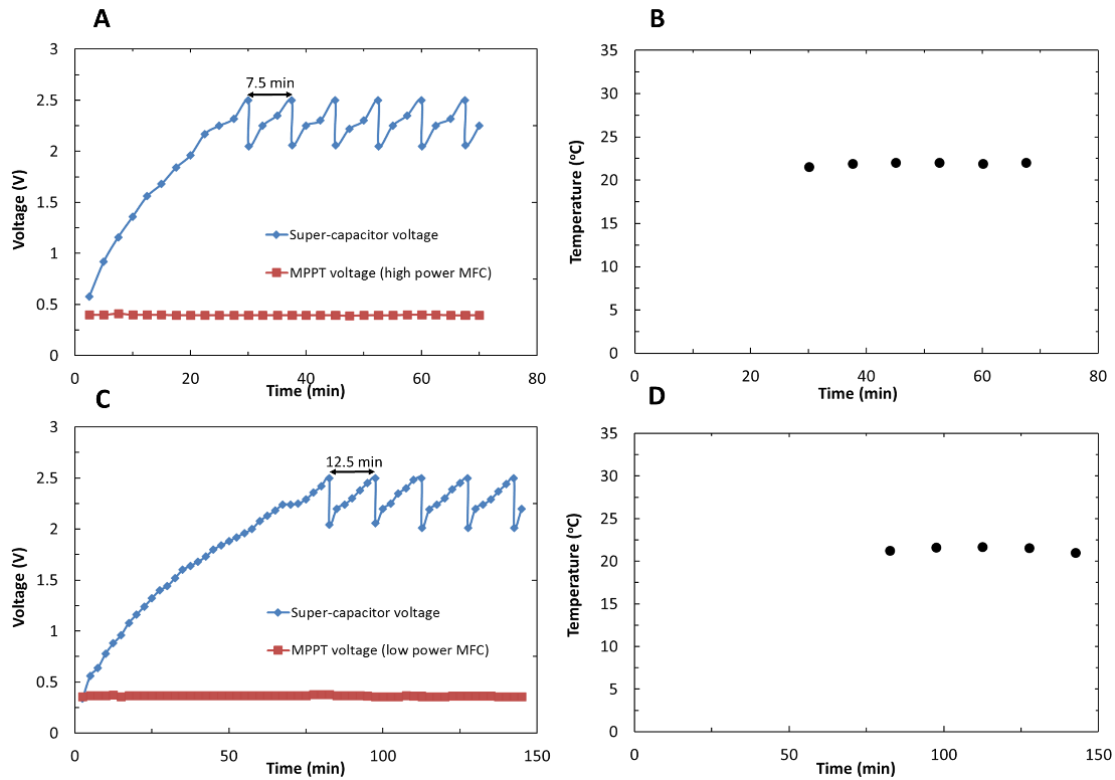


**Figure 7.3.** (A) The overall system efficiency of the PMS determined by the ratio of energy of the MFC and the energy stored in the super-capacitor (100 mF) when connected to a high-power MFC. Measurements were taken over the duration of the initial charging of the super-capacitor and periodic operating of the wireless temperature sensor. (B) System efficiency, energy from MFC, and energy stored in the super-capacitor during the initial charging stage of the super-capacitor when connected to a low-power MFC.

### **7.3.3. Demonstration with wireless sensor applications**

Due to the low power production of most small-scale MFCs, it is quite difficult to run electronic devices directly and continuously. Wireless sensors or sensor nodes are ideal electronic applications that can be powered by MFCs, however even those low-power electronic devices require a PMS for voltage boosting and maximizing the utility of the power output. The wireless temperature sensor connected to the output of the PMS was successfully powered by the MFC periodically. The super-capacitor (100 mF) was first charged to 2.5 V, and then the wireless sensor was operated and the data transmitted to a base station connected to a laptop. Charging time of the super-capacitor to 2.5 V initially took 30 minutes and the MPPT voltage (400 mV) was linear all the time as shown in Figure 7.4.A when using the HPMFC. Since the wireless sensor consumes around 85 mW, the super-capacitor voltage dropped to 2 V from 2.5 V each time a temperature reading was transmitted wirelessly. Then, it was recharged again to 2.5 V in 7.5 minutes to run the wireless temperature sensor again. Figure 7.4.B shows the periodic wireless temperature reading from our laboratory.

When testing our PMS with the LPMFC that produces lower power, it can be seen that the power production is directly related to charging time, where it took a significantly longer 87.5 minutes to initially charge the super-capacitor to 2.5 V. The time interval between measurements was 12.5 minute, almost 3 times longer compared to the case when using the HPMFC (Figure 7.4.C). The periodic wireless temperature measurement result is shown in Figure 7.4.D.



**Figure 7.4.** (A) The MPP voltage detected by the PMS and the super-capacitor voltage being charged to 2.5 V to directly power the wireless temperature sensor, when using the high-power MFC. (B) Wirelessly transmitted temperature data when using the high-power MFC. (C) Using the PMS with the low-power MFC. (D) Wireless temperature result when using the low-power MFC.

#### **7.4. Discussions**

The high efficiency of the presented PMS is directly correlated with the dynamic MPPT scheme developed here. Alaraj et al. estimated the overall system efficiency to be 33.5% and 46.1% by using diode and transformer-based boost converters, respectively.[130] However, when calculating their system efficiency, the external power required to power their PMS was not considered. Donovan et al. showed a higher maximum efficiency (~60%) using the ratio of PMS output power and input power, but in the absence of the actual load used (wireless temperature sensor)[131]. Similar measurement was also used in a dual cascaded DC-DC converter-based PMS, with efficiency was calculated to be 56.4% with fixed output loads, but again without considering the real load used for running their electronic applications.[132] Yang et al. utilized a commercially available DC-DC boost converter (LTC3108, Linear Technologies) and showed an overall system efficiency of 4.29% considering all losses due to PMS itself (thus being the most realistic case), however did not used any MPP.[133] We believe that the significantly higher overall system efficiency (7 times higher) achieved in the presented PMS (30%) under real load situation was due to the MPPT feature, integrated monolithic IC chip approach (versus commercially available discrete components), and the low-power CMOS chip design implemented in our PMS. Overall summary of efficiencies is summarized in Table 4.

**Table 4.** Comparison of properties and efficiencies of different PMSs.

Input power from MFC (mW)	MPPT	Output super-capacitor	Overall system efficiency (%)	Reference
~5.1	Yes	1 F	46.1*	[130]
~2.4	No	-	60**	[131]
~3.4	No	-	56.4**	[132]
~0.8	No	50 mF	4.29	[133]
~0.5	Yes	100 mF	30	This work

\* External power was used, however not included in efficiency calculation.

\*\* Efficiency of PMS only, not overall system efficiency.

In a similar MFC application for wireless temperature sensor operation presented by Yang et al.,[133] it took initially 2.28 hours to charge a super-capacitor (50 mF) to 3.3 V (wireless temperature sensor that consumes around 95 mW and operates at 3.3V). During each sensor data transmission, the voltage dropped to 2.5 V, after which it took 1 hour to reach back the 3.3 V. The main reason of this significantly longer charging time compared to our result can be explained by the lack of dynamically controlled MPPT, causing lower system efficiency (7 times lower than the PMS presented here). A significantly shorter charging/discharging cycle is advantageous in this kind of sensor applications.

Power consumption by the sensor is important in reducing the charge/discharge cycle time. Donovan et al. tested a wireless temperature sensor consuming only ~5mW of power during data transmission (17 times lower power requirement) with a sediment MFC (SMFC)[131]. The power production of the SMFC was 2.4 mW, which was 4.7 times higher than the MFC presented in this work. SMFC power production is normally larger than lab-scale two-chamber or one-chamber MFCs due to usage of significantly larger electrodes. Although using an MFC with significantly higher power output and using a low-power wireless temperature sensor compared to the ones used in this work, the interval of temperature measurement was ~20 minutes, longer than what the presented PMS-MFC achieved. Thus the presented low-power PMS IC circuit with dynamic MPPT feature presents a promising solution towards highly efficient MFC power management, as well as be broadly used for managing power of other low-power energy harvesting systems such as from thermoelectric or piezoelectric-based energy harvesting systems.



Although the presented PMS enable maximum power extraction from MFCs, further improvement in the absolute MFC power output by improving and optimizing the numerous factors influencing MFC power output is still necessary for MFCs to be used in practice in the future.[150, 151] While the proposed PMS here considers extracting power from a single MFC, the PMS has the potential to be used with stacks of MFCs. The MPPT in the developed PMS will only consider the equivalent resistor and equivalent capacitance from the arrayed MFC when calculating the maximum power extraction point, so array type implementations are possible with the presented PMS. A particular future work of interest is to implement a dynamically reconfigurable MFC stack, where the PMS constantly measures power production from each individual MFC units within the stack. With each sensing/measuring step, the stack can be reconfigured to deliver maximum power to the electronic load/storage unit. Another potential future works with the presented PMS is whether the MPPT scheme can be beneficial during the start-up phase of an MFC. The use of different load resistances has been shown to change the MFC start-up time [152], thus the use of MPPT that matches the internal resistance of a MFC dynamically may reduce the start-up time for MFC to reach a steady-state voltage.

## **7.5. Conclusion**

MFCs can produce only limited power and low voltages, typically not sufficient to directly power electronic systems. The monolithic PMS IC chip system presented here has the capability to boost the voltage output level to a directly usable level and continuously track the maximum power point through dynamic impedance matching circuitry to maximize

the extracted power from the MFCs. The extracted power was stored into a super-capacitor and could periodically run electronic applications such as a wireless temperature sensor with short intervals. The PMS was operated by utilizing the power from the MFC without the need for any external power, and demonstrated an overall system efficiency of 30%. We expect that the developed low-power high-efficiency PMS system will be critical in managing power output of MFCs, as well as broadly utilized in other low-power low-voltage energy harvesting systems.

## 8. OVERALL REVIEW AND CONCLUSIONS

The aim of the work is to eliminate significant limitations of microbial electrochemical cell systems and improve the overall performance with new electrode materials and analyzing tools. Here, MFC performance was improved with nanomaterial modified anodes (CNT grown SS mesh and CNT sponge) and membrane-less microfluidic MFC device was fabricated to analyze real-time biofilm anode interaction in situ. Moreover, ZnO nanowire based gas sensor was developed to detect real-time hydrogen concentration from MEC. Power management system was used to boost input voltage from MFC to run wireless temperature sensor which requires 2.5 V to transmit reading data. These improvements will help other researchers to make this technology practically available in future. The main achievements are as following:

### 8.1. Improving MFC performance with CNT modified anodes

Long and loosely packed CNTs without any amorphous carbon showed the highest power production performance. The power density was 7.4-fold higher compared to bare carbon cloth, which is the highest reported improvement for MFCs with nanomaterial-decorated electrodes. This study offers great potential for advancing the development of microbial electrochemical cell systems by providing a highly efficient nanomaterial-based electrode that delivers large surface area, high electrochemical activity, and minimum ohmic loss, as well as provide design principles for next-generation nanomaterial-based electrodes that can be broadly applicable for highly efficient microbial electrochemical cells.

Furthermore, highly-porous, light-weight, and inexpensive three-dimensional (3D) sponges consisting of interconnected carbon nanotubes (CNTs) without base materials are synthesized with a facile and scalable one-step chemical vapor deposition process as anode of microbial fuel cells (MFCs). The one-step synthesis method allowing self-assembly of 3D CNT sponges as they grow is low cost and scalable, making this a promising method for manufacturing high-performance anodes of MFCs, with broad applicability to microbial electrochemical systems in general.

### **8.2. Real-time biofilm development analytical device**

Membrane-less microfluidic laminar flow MFC was fabricated for better understanding the real-time biofilm anode interaction in situ. Biofilm development was observed under the fluorescent microscope. Both power density and biofilm impedance were measured to integrate with biofilm growth over time. The results of this study offer great potential to analyze different bacterial strains and their electrochemical properties as well as power generation in real time in a short time (~ 4 days). This tool may also help to develop anode materials based on bacterial growth properties which can be broadly applicable for MECSs.

### **8.3. Biogas monitoring device**

Hydrogen gas sensor was developed based on ZnO nanowires that responds to different hydrogen concentrations. The sensor detected the real-time hydrogen concentration from microbial electrolysis cell without additional equipment such as gas chromatography. This

sensor offer great potential to analyze biogas production with broad applicability to microbial electrochemical cell systems which generates biogas (hydrogen, methane) in general.

#### **8.4. Efficient energy harvesting from MFC with PMS**

This study presented a monolithic low-power consuming PMS integrated circuit (IC) chip capable of dynamic maximum power point tracking (MPPT) to maximize the extracted power from MFCs, regardless of the power and voltage fluctuations from MFCs over time. The developed low-power high-efficiency PMS system will be critical in managing power output of MFCs, as well as broadly utilized in other low-power and low-voltage energy harvesting systems.

## REFERENCES

- [1] *World Energy Outlook 2015*. Available:  
<http://www.worldenergyoutlook.org/weo2015/>
- [2] *The United Nations World Water Development Report 2015*. Available:  
<http://www.unwater.org/publications/world-water-development-report/en/>
- [3] *Medium-Term Renewable Energy Market Report 2015*. Available:  
[https://www.iea.org/bookshop/708-Medium-Term\\_Renewable\\_Energy\\_Market\\_Report\\_2015](https://www.iea.org/bookshop/708-Medium-Term_Renewable_Energy_Market_Report_2015)
- [4] M. C. Potter, "Electrical effects accompanying the decomposition of organic compounds.," *Royal Society (Formerly Proceedings of the Royal Society) B*, vol. 84, pp. 260-276, 1911.
- [5] B. Cohen, "The Bacterial Culture as an Electrical Half-Cell," *Journal of Bacteriology*, vol. 21, pp. 18–19, 1931.
- [6] H. P. Bennetto, "Microbial Fuel Cells, in: Life Chemistry Reports," *Harwood Acad. Press*, vol. 2, pp. 363–453, 1984.
- [7] H. P. B. S.D.Roller, G.M.Delaney, J.R.Mason, J.L.Stirling and C.F.Thurston, "Electron-transfer coupling in microbial fuel cells,1; comparison of redox mediator reduction rates and respiratory rates of bacteria," *J.Chem.Tech.Biotechnol*, vol. 34B, pp. 3–12, 1984.

- [8] P. H. Kim HJ, Hyun MS, Chang IS, Kim M, Kim BH, "A mediatorless microbial fuel cell using a metal reducing bacterium, *Shewanella putrefaciens.*," *Enzyme Microb Tech*, vol. 30, pp. 145–152, 2002.
- [9] D. R. Lovley, "Bug juice: harvesting electricity with microorganisms," *Nat Rev Micro*, vol. 4, pp. 497-508, 07//print 2006.
- [10] U. Schroder, "Anodic electron transfer mechanisms in microbial fuel cells and their energy efficiency," *Physical Chemistry Chemical Physics*, vol. 9, pp. 2619-2629, 2007.
- [11] S. M. Strycharz-Glaven, R. M. Snider, A. Guiseppi-Elie, and L. M. Tender, "On the electrical conductivity of microbial nanowires and biofilms," *Energy & Environmental Science*, vol. 4, pp. 4366-4379, 2011.
- [12] C. I. Torres, A. K. Marcus, H.-S. Lee, P. Parameswaran, R. Krajmalnik-Brown, and B. E. Rittmann, "A kinetic perspective on extracellular electron transfer by anode-respiring bacteria," *FEMS Microbiology Reviews*, vol. 34, pp. 3-17, 2010.
- [13] B. E. Logan, B. Hamelers, R. Rozendal, U. Schröder, J. Keller, S. Freguia, *et al.*, "Microbial Fuel Cells: Methodology and Technology," *Environ Sci Technol.*, vol. 40, pp. 5181-5192, 2006.
- [14] J. Wei, P. Liang, and X. Huang, "Recent progress in electrodes for microbial fuel cells," *Bioresource Technology*, vol. 102, pp. 9335-9344, 2011.
- [15] B. E. Logan, *Microbial Fuel Cells*: Wiley, 2008.

- [16] B. Logan, S. Cheng, V. Watson, and G. Estadt, "Graphite Fiber Brush Anodes for Increased Power Production in Air-Cathode Microbial Fuel Cells," *Environmental Science & Technology*, vol. 41, pp. 3341-3346, 2007.
- [17] Y. Fan, S. Xu, R. Schaller, J. Jiao, F. Chaplen, and H. Liu, "Nanoparticle decorated anodes for enhanced current generation in microbial electrochemical cells," *Biosens Bioelectron.*, vol. 26, pp. 1908-12, 2011.
- [18] W. Guo, Y. Pi, H. Song, W. Tang, and J. Sun, "Layer-by-layer assembled gold nanoparticles modified anode and its application in microbial fuel cells," *Colloids and Surfaces A: Physicochemical and Engineering Aspects*, vol. 415, pp. 105-111, 2012.
- [19] Y. Zhang, G. Mo, X. Li, W. Zhang, J. Zhang, J. Ye, *et al.*, "A graphene modified anode to improve the performance of microbial fuel cells," *Journal of Power Sources*, vol. 196, pp. 5402-5407, 2011.
- [20] J. Liu, Y. Qiao, C. X. Guo, S. Lim, H. Song, and C. M. Li, "Graphene/carbon cloth anode for high-performance mediatorless microbial fuel cells," *Bioresour Technol*, vol. 114, pp. 275-280, 2012.
- [21] H. Wang, G. Wang, Y. Ling, F. Qian, Y. Song, X. Lu, *et al.*, "High power density microbial fuel cell with flexible 3D graphene-nickel foam as anode," *Nanoscale*, vol. 5, pp. 10283-10290, 2013.
- [22] X. Xie, M. Ye, L. Hu, N. Liu, J. R. McDonough, W. Chen, *et al.*, "Carbon nanotube-coated macroporous sponge for microbial fuel cell electrodes," *Energy Environ Sci*, vol. 5, pp. 5265-5270, 2012.



- [23] C. Erbay, X. Pu, W. Choi, M.-J. Choi, Y. Ryu, H. Hou, *et al.*, "Control of geometrical properties of carbon nanotube electrodes towards high-performance microbial fuel cells," *J Power Sources*, vol. 280, pp. 347-354, 2015.
- [24] S. Ci, Z. Wen, J. Chen, and Z. He, "Decorating anode with bamboo-like nitrogen-doped carbon nanotubes for microbial fuel cells," *Electrochemistry Communications*, vol. 14, pp. 71-74, 2012.
- [25] H. Ren, S. Pyo, J.-I. Lee, T.-J. Park, F. S. Gittleson, F. C. C. Leung, *et al.*, "A high power density miniaturized microbial fuel cell having carbon nanotube anodes," *J Power Sources*, vol. 273, pp. 823-830, 2015.
- [26] H.-Y. Tsai, C.-C. Wu, C.-Y. Lee, and E. P. Shih, "Microbial fuel cell performance of multiwall carbon nanotubes on carbon cloth as electrodes," *J Power Sources*, vol. 194, pp. 199-205, 2009.
- [27] J. E. Mink, J. P. Rojas, B. E. Logan, and M. M. Hussain, "Vertically grown multiwalled carbon nanotube anode and nickel silicide integrated high performance micro-sized (1.25  $\mu$ L) microbial fuel cell," *Nano Lett.*, vol. 12, pp. 791-5, 2012.
- [28] C. Li, L. Zhang, L. Ding, H. Ren, and H. Cui, "Effect of conductive polymers coated anode on the performance of microbial fuel cells (MFCs) and its biodiversity analysis," *Biosensors and Bioelectronics*, vol. 26, pp. 4169-4176, 2011.

- [29] M. Adachi, T. Shimomura, M. Komatsu, H. Yakuwa, and A. Miya, "A novel mediator-polymer-modified anode for microbial fuel cells," *Chemical Communications*, pp. 2055-2057, 2008.
- [30] Y. Yuan, S. Zhou, Y. Liu, and J. Tang, "Nanostructured Macroporous Bioanode Based on Polyaniline-Modified Natural Loofah Sponge for High-Performance Microbial Fuel Cells," *Environ Sci Technol.*, vol. 47, pp. 14525-14532, 2013.
- [31] R. A. Rozendal, H. V. M. Hamelers, K. Rabaey, J. Keller, and C. J. N. Buisman, "Towards practical implementation of bioelectrochemical wastewater treatment," *Trends Biotechnol.*, vol. 26, pp. 450-459, 2008.
- [32] K. Ben Liew, W. R. W. Daud, M. Ghasemi, J. X. Leong, S. Su Lim, and M. Ismail, "Non-Pt catalyst as oxygen reduction reaction in microbial fuel cells: A review," *Int. J. Hydrogen Energy*, vol. 39, pp. 4870-4883, 2014.
- [33] X. Xie, M. Pasta, L. Hu, Y. Yang, J. McDonough, J. Cha, *et al.*, "Nano-structured textiles as high-performance aqueous cathodes for microbial fuel cells," *Energy Environ. Sci.*, vol. 4, pp. 1293-1297, 2011.
- [34] H. Wang, Z. Wu, A. Plaseied, P. Jenkins, L. Simpson, C. Engrakul, *et al.*, "Carbon nanotube modified air-cathodes for electricity production in microbial fuel cells," *J. Power Sources*, vol. 196, pp. 7465-7469, 2011.
- [35] K. B. Liew, W. R. Wan Daud, M. Ghasemi, K. S. Loh, M. Ismail, S. S. Lim, *et al.*, "Manganese oxide/functionalised carbon nanotubes nanocomposite as catalyst for oxygen reduction reaction in microbial fuel cell," *Int. J. Hydrogen Energy*.

- [36] G. Yang, C. Erbay, S.-i. Yi, P. de Figueiredo, R. Sadr, A. Han, *et al.*, "Bifunctional nano-sponges serving as non-precious metal catalysts and self-standing cathodes for high performance fuel cell applications," *Nano Energy*, vol. 22, pp. 607-614, 2016.
- [37] G. Reguera, K. D. McCarthy, T. Mehta, J. S. Nicoll, M. T. Tuominen, and D. R. Lovley, "Extracellular electron transfer via microbial nanowires," *Nature*, vol. 435, pp. 1098-101, 2005.
- [38] H. Rismani-Yazdi, S. M. Carver, A. D. Christy, and O. H. Tuovinen, "Cathodic limitations in microbial fuel cells: An overview," *J. Power Sources*, vol. 180, pp. 683-694, 2008.
- [39] B. Erable, D. Féron, and A. Bergel, "Microbial Catalysis of the Oxygen Reduction Reaction for Microbial Fuel Cells: A Review," *ChemSusChem*, vol. 5, pp. 975-987, 2012.
- [40] Y. Qiao, S.-J. Bao, and C. M. Li, "Electrocatalysis in microbial fuel cells-from electrode material to direct electrochemistry," *Energy Environ. Sci.*, vol. 3, pp. 544-553, 2010.
- [41] M. Rahimnejad, G. Bakeri, M. Ghasemi, and A. Zirepour, "A review on the role of proton exchange membrane on the performance of microbial fuel cell," *Polymers for Advanced Technologies*, vol. 25, pp. 1426-1432, 2014.
- [42] M. Rahimnejad, A. Adhami, S. Darvari, A. Zirepour, and S.-E. Oh, "Microbial fuel cell as new technology for bioelectricity generation: A review," *Alexandria Engineering Journal*, vol. 54, pp. 745-756, 2015.

- [43] J. R. Kim, S. Cheng, S.-E. Oh, and B. E. Logan, "Power Generation Using Different Cation, Anion, and Ultrafiltration Membranes in Microbial Fuel Cells," *Environmental Science & Technology*, vol. 41, pp. 1004-1009, 2007.
- [44] B. E. Logan, C. Murano, K. Scott, N. D. Gray, and I. M. Head, "Electricity generation from cysteine in a microbial fuel cell," *Water Research*, vol. 39, pp. 942-952, 2005.
- [45] H. Liu, S. Cheng, and B. E. Logan, "Production of Electricity from Acetate or Butyrate Using a Single-Chamber Microbial Fuel Cell," *Environmental Science & Technology*, vol. 39, pp. 658-662, 2005.
- [46] S. Cheng, H. Liu, and B. E. Logan, "Increased performance of single-chamber microbial fuel cells using an improved cathode structure," *Electrochemistry Communications*, vol. 8, pp. 489-494, 2006.
- [47] L. De Schampelaire, K. Rabaey, P. Boeckx, N. Boon, and W. Verstraete, "Outlook for benefits of sediment microbial fuel cells with two bio-electrodes," *Microbial biotechnology*, vol. 1, pp. 446-462, 2008.
- [48] T. Ewing, P. T. Ha, J. T. Babauta, N. T. Tang, D. Heo, and H. Beyenal, "Scale-up of sediment microbial fuel cells," *Journal of Power Sources*, vol. 272, pp. 311-319, 2014.
- [49] I. Ieropoulos, J. Greenman, and C. Melhuish, "Microbial fuel cells based on carbon veil electrodes: Stack configuration and scalability," *International Journal of Energy Research*, vol. 32, pp. 1228-1240, 2008.

- [50] P. Aelterman, K. Rabaey, H. T. Pham, N. Boon, and W. Verstraete, "Continuous Electricity Generation at High Voltages and Currents Using Stacked Microbial Fuel Cells," *Environmental Science & Technology*, vol. 40, pp. 3388-3394, 2006.
- [51] P. Ledezma, A. Stinchcombe, J. Greenman, and I. Ieropoulos, "The first self-sustainable microbial fuel cell stack," *Physical Chemistry Chemical Physics*, vol. 15, pp. 2278-2281, 2013.
- [52] S. Wu, H. Li, X. Zhou, P. Liang, X. Zhang, Y. Jiang, *et al.*, "A novel pilot-scale stacked microbial fuel cell for efficient electricity generation and wastewater treatment," *Water Research*, vol. 98, pp. 396-403, 2016.
- [53] S. E. Oh and B. E. Logan, "Voltage reversal during microbial fuel cell stack operation," *J Power Sources*, vol. 167, pp. 11-17, 2007.
- [54] H. Ren, C. I. Torres, P. Parameswaran, B. E. Rittmann, and J. Chae, "Improved current and power density with a micro-scale microbial fuel cell due to a small characteristic length," *Biosensors and Bioelectronics*, vol. 61, pp. 587-592, 2014.
- [55] H. Hou, L. Li, Y. Cho, P. de Figueiredo, and A. Han, "Microfabricated microbial fuel cell arrays reveal electrochemically active microbes," *PLoS One*, vol. 4, p. e6570, 2009.
- [56] H. Hou, L. Li, P. de Figueiredo, and A. Han, "Air-cathode microbial fuel cell array: A device for identifying and characterizing electrochemically active microbes," *Biosensors and Bioelectronics*, vol. 26, pp. 2680-2684, 2011.

- [57] H. Hou, L. Li, C. U. Ceylan, A. Haynes, J. Cope, H. H. Wilkinson, *et al.*, "A microfluidic microbial fuel cell array that supports long-term multiplexed analyses of electricigens," *Lab Chip*, vol. 12, pp. 4151-4159, 2012.
- [58] J. E. Mink and M. M. Hussain, "Sustainable Design of High-Performance Microsized Microbial Fuel Cell with Carbon Nanotube Anode and Air Cathode," *ACS Nano*, vol. 7, pp. 6921-6927, 2013.
- [59] J. E. Mink, R. M. Qaisi, B. E. Logan, and M. M. Hussain, "Energy harvesting from organic liquids in micro-sized microbial fuel cells," *NPG Asia Mater*, vol. 6, p. e89, 2014.
- [60] F. Qian, M. Baum, Q. Gu, and D. E. Morse, "A 1.5  $\mu$ L microbial fuel cell for on-chip bioelectricity generation," *Lab on a Chip*, vol. 9, pp. 3076-3081, 2009.
- [61] F. Qian, Z. He, M. P. Thelen, and Y. Li, "A microfluidic microbial fuel cell fabricated by soft lithography," *Bioresource Technology*, vol. 102, pp. 5836-5840, 2011.
- [62] S. Choi, "Microscale microbial fuel cells: Advances and challenges," *Biosensors and Bioelectronics*, vol. 69, pp. 8-25, 2015.
- [63] Z. Du, H. Li, and T. Gu, "A state of the art review on microbial fuel cells: A promising technology for wastewater treatment and bioenergy," *Biotechnology Advances*, vol. 25, pp. 464-482, 2007.
- [64] M. Zhou, H. Wang, D. J. Hassett, and T. Gu, "Recent advances in microbial fuel cells (MFCs) and microbial electrolysis cells (MECs) for wastewater treatment,

- bioenergy and bioproducts," *Journal of Chemical Technology & Biotechnology*, vol. 88, pp. 508-518, 2013.
- [65] H. Wang, J.-D. Park, and Z. J. Ren, "Practical Energy Harvesting for Microbial Fuel Cells: A Review," *Environmental Science & Technology*, vol. 49, pp. 3267-3277, 2015.
- [66] Y. Feng, X. Wang, B. E. Logan, and H. Lee, "Brewery wastewater treatment using air-cathode microbial fuel cells," *Applied Microbiology and Biotechnology*, vol. 78, pp. 873-880, 2008.
- [67] J. J. Fornero, M. Rosenbaum, and L. T. Angenent, "Electric Power Generation from Municipal, Food, and Animal Wastewaters Using Microbial Fuel Cells," *Electroanalysis*, vol. 22, pp. 832-843, 2010.
- [68] B. Min, J. Kim, S. Oh, J. M. Regan, and B. E. Logan, "Electricity generation from swine wastewater using microbial fuel cells," *Water Research*, vol. 39, pp. 4961-4968, 2005.
- [69] B. E. Logan, D. Call, S. Cheng, H. V. Hamelers, T. H. Sleutels, A. W. Jeremiasse, *et al.*, "Microbial electrolysis cells for high yield hydrogen gas production from organic matter," *Environ Sci Technol*, vol. 42, pp. 8630-40, 2008.
- [70] Y. Zhang and I. Angelidaki, "Microbial electrolysis cells turning to be versatile technology: recent advances and future challenges," *Water Res*, vol. 56, pp. 11-25, 2014.

- [71] M. Zhou, J. Yang, H. Wang, T. Jin, D. Xu, and T. Gu, "Microbial fuel cells and microbial electrolysis cells for the production of bioelectricity and biomaterials," *Environ Technol*, vol. 34, pp. 1915-28, 2013.
- [72] A. Kadier, Y. Simayi, P. Abdeshahian, N. F. Azman, K. Chandrasekhar, and M. S. Kalil, "A comprehensive review of microbial electrolysis cells (MEC) reactor designs and configurations for sustainable hydrogen gas production," *Alexandria Engineering Journal*, vol. 55, pp. 427-443, 2016.
- [73] X. Cao, X. Huang, P. Liang, K. Xiao, Y. Zhou, X. Zhang, *et al.*, "A New Method for Water Desalination Using Microbial Desalination Cells," *Environmental Science & Technology*, vol. 43, pp. 7148-7152, 2009.
- [74] H. M. Saeed, G. A. Hussein, S. Yousef, J. Saif, S. Al-Asheh, A. Abu Fara, *et al.*, "Microbial desalination cell technology: A review and a case study," *Desalination*, vol. 359, pp. 1-13, 2015.
- [75] J.-J. Sun, H.-Z. Zhao, Q.-Z. Yang, J. Song, and A. Xue, "A novel layer-by-layer self-assembled carbon nanotube-based anode: Preparation, characterization, and application in microbial fuel cell," *Electrochimica Acta*, vol. 55, pp. 3041-3047, 2010.
- [76] N. Thepsuparungsikul, N. Phonthamachai, and H. Y. Ng, "Multi-walled carbon nanotubes as electrode material for microbial fuel cells," *Water Sci Technol*, vol. 65, pp. 1208-14, 2012.



- [77] X. Xie, L. Hu, M. Pasta, G. F. Wells, D. Kong, C. S. Criddle, *et al.*, "Three-dimensional carbon nanotube-textile anode for high-performance microbial fuel cells," *Nano Lett.*, vol. 11, pp. 291-6, 2011.
- [78] Y. Zhao, K. Watanabe, and K. Hashimoto, "Hierarchical micro/nano structures of carbon composites as anodes for microbial fuel cells," *Phys. Chem. Chem. Phys.*, vol. 13, pp. 15016-21, 2011.
- [79] T. Sharma, A. L. Mohana Reddy, T. S. Chandra, and S. Ramaprabhu, "Development of carbon nanotubes and nanofluids based microbial fuel cell," *Int J Hydrogen Energ.*, vol. 33, pp. 6749-6754, 2008.
- [80] K. J. Chae, M. Choi, F. F. Ajayi, W. Park, I. S. Chang, and I. S. Kim, "Mass Transport through a Proton Exchange Membrane (Nafion) in Microbial Fuel Cells," *Energy Fuels*, vol. 22, pp. 169-176, 2007.
- [81] D. Tasis, N. Tagmatarchis, A. Bianco, and M. Prato, "Chemistry of carbon nanotubes," *Chem Rev*, vol. 106, pp. 1105-36, 2006.
- [82] K. M. Leung, G. Wanger, M. Y. El-Naggar, Y. Gorby, G. Southam, W. M. Lau, *et al.*, "Shewanella oneidensis MR-1 bacterial nanowires exhibit p-type, tunable electronic behavior," *Nano Lett*, vol. 13, pp. 2407-11, 2013.
- [83] X. Jiang, J. Hu, L. A. Fitzgerald, J. C. Biffinger, P. Xie, B. R. Ringeisen, *et al.*, "Probing electron transfer mechanisms in Shewanella oneidensis MR-1 using a nanoelectrode platform and single-cell imaging," *Proc Natl Acad Sci U S A*, vol. 107, pp. 16806-10, 2010.

- [84] N. S. Malvankar, M. Vargas, K. P. Nevin, A. E. Franks, C. Leang, B. C. Kim, *et al.*, "Tunable metallic-like conductivity in microbial nanowire networks," *Nat Nanotechnol*, vol. 6, pp. 573-9, 2011.
- [85] N. S. Malvankar, M. T. Tuominen, and D. R. Lovley, "Comment on "on electrical conductivity of microbial nanowires and biofilms" by S. M. Strycharz-Glaven, R. M. Snider, A. Guiseppi-Elie and L. M. Tender, *Energy Environ. Sci.*, 2011, 4, 4366," *Energy and Environmental Science*, vol. 5, pp. 6247-6249, 2012.
- [86] Y. Ryu, L. Yin, and C. Yu, "Dramatic electrical conductivity improvement of carbon nanotube networks by simultaneous de-bundling and hole-doping with chlorosulfonic acid," *Journal of Materials Chemistry*, vol. 22, pp. 6959-6964, 2012.
- [87] M. Zhou, M. Chi, J. Luo, H. He, and T. Jin, "An overview of electrode materials in microbial fuel cells," *J Power Sources*, vol. 196, pp. 4427-4435, 2011.
- [88] Y. Zhang, G. Mo, X. Li, W. Zhang, J. Zhang, J. Ye, *et al.*, "A graphene modified anode to improve the performance of microbial fuel cells," *J Power Sources*, vol. 196, pp. 5402-5407, 7/1/ 2011.
- [89] A. J. Hutchinson, J. C. Tokash, and B. E. Logan, "Analysis of carbon fiber brush loading in anodes on startup and performance of microbial fuel cells," *J Power Sources*, vol. 196, pp. 9213-9219, 2011.
- [90] W. Chen, Y.-X. Huang, D.-B. Li, H.-Q. Yu, and L. Yan, "Preparation of a macroporous flexible three dimensional graphene sponge using an ice-template

- as the anode material for microbial fuel cells," *RSC Adv*, vol. 4, pp. 21619-21624, 2014.
- [91] X. Xie, G. Yu, N. Liu, Z. Bao, C. S. Criddle, and Y. Cui, "Graphene-sponges as high-performance low-cost anodes for microbial fuel cells," *Energy Environ Sci*, vol. 5, pp. 6862-6866, 2012.
- [92] V. Gadhamshetty and N. Koratkar, "Nano-engineered biocatalyst-electrode structures for next generation microbial fuel cells," *Nano Energy*, vol. 1, pp. 3-5, 2012.
- [93] Y. C. Yong, X. C. Dong, M. B. Chan-Park, H. Song, and P. Chen, "Macroporous and monolithic anode based on polyaniline hybridized three-dimensional graphene for high-performance microbial fuel cells," *ACS Nano*, vol. 6, pp. 2394-400, 2012.
- [94] C. Erbay, G. Yang, P. de Figueiredo, R. Sadr, C. Yu, and A. Han, "Three-dimensional porous carbon nanotube sponges for high-performance anodes of microbial fuel cells," *Journal of Power Sources*, vol. 298, pp. 177-183, 2015.
- [95] C. Erbay, S. Carreon-Bautista, E. Sanchez-Sinencio, and A. Han, "High Performance Monolithic Power Management System with Dynamic Maximum Power Point Tracking for Microbial Fuel Cells," *Environ Sci Technol.*, vol. 48, pp. 13992-13999, 2014.
- [96] X. C. Gui, J. Q. Wei, K. L. Wang, A. Y. Cao, H. W. Zhu, Y. Jia, *et al.*, "Carbon Nanotube Sponges," *Adv Mater*, vol. 22, pp. 617-621, 2010.

- [97] H. Wang, Z. Wu, A. Plaseied, P. Jenkins, L. Simpson, C. Engtrakul, *et al.*, "Carbon nanotube modified air-cathodes for electricity production in microbial fuel cells," *J Power Sources*, vol. 196, pp. 7465-7469, 9/15/ 2011.
- [98] X. C. Gui, Z. P. Zeng, Y. Zhu, H. B. Li, Z. Q. Lin, Q. M. Gan, *et al.*, "Three-Dimensional Carbon Nanotube Sponge-Array Architectures with High Energy Dissipation," *Adv Mater*, vol. 26, pp. 1248-1253, 2014.
- [99] Z. P. Zeng, X. C. Gui, Z. Q. Lin, L. H. Zhang, Y. Jia, A. Y. Cao, *et al.*, "Carbon Nanotube Sponge-Array Tandem Composites with Extended Energy Absorption Range," *Adv Mater*, vol. 25, pp. 1185-1191, 2013.
- [100] Q. Y. Peng, Y. B. Li, X. D. He, X. C. Gui, Y. Y. Shang, C. H. Wang, *et al.*, "Graphene Nanoribbon Aerogels Unzipped from Carbon Nanotube Sponges," *Adv Mater*, vol. 26, pp. 3241-3247, 2014.
- [101] X. Pu, G. Yang, and C. Yu, "Liquid-Type Cathode Enabled by 3D Sponge-Like Carbon Nanotubes for High Energy Density and Long Cycling Life of Li-S Batteries," *Adv Mater*, vol. 26, pp. 7456-7461, 2014.
- [102] K. Rabaey, J. Rodriguez, L. L. Blackall, J. Keller, P. Gross, D. Batstone, *et al.*, "Microbial ecology meets electrochemistry: electricity-driven and driving communities," *ISME J*, vol. 1, pp. 9-18, 0000.
- [103] H. Ren, H.-S. Lee, and J. Chae, "Miniaturizing microbial fuel cells for potential portable power sources: promises and challenges," *Microfluidics and Nanofluidics*, vol. 13, pp. 353-381, 2012.

- [104] Z. Li, A. Venkataraman, M. A. Rosenbaum, and L. T. Angenent, "A laminar-flow microfluidic device for quantitative analysis of microbial electrochemical activity," *ChemSusChem*, vol. 5, pp. 1119-23, 2012.
- [105] H. Y. Wang and J. Y. Su, "Membraneless microfluidic microbial fuel cell for rapid detection of electrochemical activity of microorganism," *Bioresour Technol*, vol. 145, pp. 271-4, 2013.
- [106] L. Yang, Y. Li, C. L. Griffis, and M. G. Johnson, "Interdigitated microelectrode (IME) impedance sensor for the detection of viable *Salmonella typhimurium*," *Biosensors and Bioelectronics*, vol. 19, pp. 1139-1147, 2004.
- [107] M. Varshney and Y. Li, "Interdigitated array microelectrode based impedance biosensor coupled with magnetic nanoparticle-antibody conjugates for detection of *Escherichia coli* O157:H7 in food samples," *Biosensors and Bioelectronics*, vol. 22, pp. 2408-2414, 2007.
- [108] R. F. Ismagilov, A. D. Stroock, P. J. A. Kenis, G. Whitesides, and H. A. Stone, "Experimental and theoretical scaling laws for transverse diffusive broadening in two-phase laminar flows in microchannels," *Applied Physics Letters*, vol. 76, pp. 2376-2378, 2000.
- [109] A. Fraiwan, D. F. Call, and S. Choi, "Bacterial growth and respiration in laminar flow microbial fuel cells," *Journal of Renewable and Sustainable Energy*, vol. 6, p. 023125, 2014.
- [110] A. Fraiwan, S. P. Adusumilli, D. Han, A. J. Steckl, D. F. Call, C. R. Westgate, *et al.*, "Microbial Power-Generating Capabilities on Micro-/Nano-Structured

- Anodes in Micro-Sized Microbial Fuel Cells," *Fuel Cells*, vol. 14, pp. 801-809, 2014.
- [111] D. Vigolo, T. T. Al-Housseiny, Y. Shen, F. O. Akinlawon, S. T. Al-Housseiny, R. K. Hobson, *et al.*, "Flow dependent performance of microfluidic microbial fuel cells," *Physical Chemistry Chemical Physics*, vol. 16, pp. 12535-12543, 2014.
- [112] B. E. Rittman, "The effect of shear stress on biofilm loss rate," *Biotechnol Bioeng*, vol. 24, pp. 501-6, 1982.
- [113] Z. Li, Y. Zhang, P. R. LeDuc, and K. B. Gregory, "Microbial electricity generation via microfluidic flow control," *Biotechnol Bioeng*, vol. 108, pp. 2061-9, 2011.
- [114] K. P. Nevin, H. Richter, S. F. Covalla, J. P. Johnson, T. L. Woodard, A. L. Orloff, *et al.*, "Power output and columbic efficiencies from biofilms of *Geobacter sulfurreducens* comparable to mixed community microbial fuel cells," *Environmental Microbiology*, vol. 10, pp. 2505-2514, 2008.
- [115] J. Paredes, S. Becerro, F. Arizti, A. Aguinaga, J. L. Del Pozo, and S. Arana, "Interdigitated microelectrode biosensor for bacterial biofilm growth monitoring by impedance spectroscopy technique in 96-well microtiter plates," *Sensors and Actuators B: Chemical*, vol. 178, pp. 663-670, 2013.
- [116] J. Paredes, S. Becerro, F. Arizti, A. Aguinaga, J. L. Del Pozo, and S. Arana, "Real time monitoring of the impedance characteristics of Staphylococcal

- bacterial biofilm cultures with a modified CDC reactor system," *Biosensors and Bioelectronics*, vol. 38, pp. 226-232, 2012.
- [117] J. Paredes, S. Becerro, and S. Arana, "Label-free interdigitated microelectrode based biosensors for bacterial biofilm growth monitoring using Petri dishes," *Journal of Microbiological Methods*, vol. 100, pp. 77-83, 2014.
- [118] A. E. Franks, K. P. Nevin, H. Jia, M. Izallalen, T. L. Woodard, and D. R. Lovley, "Novel strategy for three-dimensional real-time imaging of microbial fuel cell communities: monitoring the inhibitory effects of proton accumulation within the anode biofilm," *Energy & Environmental Science*, vol. 2, pp. 113-119, 2009.
- [119] J. S. McLean, G. Wanger, Y. A. Gorby, M. Wainstein, J. McQuaid, S. i. Ishii, *et al.*, "Quantification of Electron Transfer Rates to a Solid Phase Electron Acceptor through the Stages of Biofilm Formation from Single Cells to Multicellular Communities," *Environmental Science & Technology*, vol. 44, pp. 2721-2727, 2010.
- [120] A. E. Inglesby, K. Yunus, and A. C. Fisher, "In situ fluorescence and electrochemical monitoring of a photosynthetic microbial fuel cell," *Physical Chemistry Chemical Physics*, vol. 15, pp. 6903-6911, 2013.
- [121] R. Gupta, W. Bekele, and A. Ghatak, "Harvesting energy of interaction between bacteria and bacteriophage in a membrane-less fuel cell," *Bioresource Technology*, vol. 147, pp. 654-657, 2013.

- [122] S. Cheng and B. E. Logan, "High hydrogen production rate of microbial electrolysis cell (MEC) with reduced electrode spacing," *Bioresour Technol*, vol. 102, pp. 3571-4, 2011.
- [123] H. Gu, Z. Wang, and Y. Hu, "Hydrogen gas sensors based on semiconductor oxide nanostructures," *Sensors (Basel)*, vol. 12, pp. 5517-50, 2012.
- [124] T. Quan, L. Liming, and L. Guangyong, "Selective manipulation of ZnO nanowires by controlled dielectrophoretic force," in *Nanotechnology (IEEE-NANO), 2011 11th IEEE Conference on*, 2011, pp. 1106-1109.
- [125] D. R. Lovley, "The microbe electric: conversion of organic matter to electricity," *Curr Opin Biotechnol*, vol. 19, pp. 564-71, 2008.
- [126] Z. He, S. D. Minteer, and L. T. Angenent, "Electricity Generation from Artificial Wastewater Using an Upflow Microbial Fuel Cell," *Environ Sci Technol*, vol. 39, pp. 5262-5267, 2005.
- [127] H. Liu, S. Cheng, L. Huang, and B. E. Logan, "Scale-up of membrane-free single-chamber microbial fuel cells," *J Power Sources*, vol. 179, pp. 274-279, 2008.
- [128] Y. Kim, M. C. Hatzell, A. J. Hutchinson, and B. E. Logan, "Capturing power at higher voltages from arrays of microbial fuel cells without voltage reversal," *Environ Sci Technol*, vol. 4, pp. 4662-4667, 2011.
- [129] J.-D. Park and Z. Ren, "Hysteresis controller based maximum power point tracking energy harvesting system for microbial fuel cells," *J Power Sources*, vol. 205, pp. 151-156, 2012.



- [130] M. Alaraj, Z. J. Ren, and J.-D. Park, "Microbial fuel cell energy harvesting using synchronous flyback converter," *J Power Sources*, vol. 247, pp. 636-642, 2014.
- [131] C. Donovan, A. Dewan, D. Heo, and H. Beyenal, "Batteryless, wireless sensor powered by a sediment microbial fuel cell," *Environ Sci Technol*, vol. 42, pp. 8591-6, 2008.
- [132] C. Donovan, A. Dewan, H. Peng, D. Heo, and H. Beyenal, "Power management system for a 2.5 W remote sensor powered by a sediment microbial fuel cell," *J Power Sources*, vol. 196, pp. 1171-1177, 2011.
- [133] F. Yang, D. Zhang, T. Shimotori, K.-C. Wang, and Y. Huang, "Study of transformer-based power management system and its performance optimization for microbial fuel cells," *J Power Sources*, vol. 205, pp. 86-92, 2012.
- [134] J.-D. Park and Z. Ren, "High efficiency energy harvesting from microbial fuel cells using a synchronous boost converter," *J Power Sources*, vol. 208, pp. 322-327, 2012.
- [135] Y. R. J. Thomas, M. Picot, A. Carer, O. Berder, O. Sentieys, and F. Barrière, "A single sediment-microbial fuel cell powering a wireless telecommunication system," *J Power Sources*, vol. 241, pp. 703-708, 2013.
- [136] D. Zhang, F. Yang, T. Shimotori, K.-C. Wang, and Y. Huang, "Performance evaluation of power management systems in microbial fuel cell-based energy harvesting applications for driving small electronic devices," *J Power Sources*, vol. 217, pp. 65-71, 2012.

- [137] A. Meehan, G. Hongwei, and Z. Lewandowski, "Energy Harvesting With Microbial Fuel Cell and Power Management System," *IEEE Trans Power Electron*, vol. 26, pp. 176-181, 2011.
- [138] S. Carreon-Bautista, A. Eladawy, A. Nadar Mohieldin, and E. Sanchez-Sinencio, "Boost Converter with Dynamic Input Impedance Matching for Energy Harvesting with Multi-Array Thermoelectric Generators," *IEEE Trans Ind Electron*, vol. PP, pp. 1-1, 2014.
- [139] E. J. Carlson, K. Strunz, and B. P. Otis, "A 20 mV Input Boost Converter With Efficient Digital Control for Thermoelectric Energy Harvesting," *IEEE J Solid-State Circuits*, vol. 45, pp. 741-750, 2010.
- [140] I. Jong-Pil, W. Se-Won, R. Seung-Tak, and C. Gyu-Hyeong, "A 40 mV Transformer-Reuse Self-Startup Boost Converter With MPPT Control for Thermoelectric Energy Harvesting," *IEEE J Solid-State Circuits*, vol. 47, pp. 3055-3067, 2012.
- [141] K. R. Elizabeth, B. Fred, F. Romy, and W. Paul, "Powering a wireless sensor node with a vibration-driven piezoelectric energy harvester," *Smart Mater Struct*, vol. 20, p. 125006, 2011.
- [142] Y. K. Ramadass and A. P. Chandrakasan, "An Efficient Piezoelectric Energy Harvesting Interface Circuit Using a Bias-Flip Rectifier and Shared Inductor," *IEEE J Solid-State Circuits*, vol. 45, pp. 189-204, 2010.

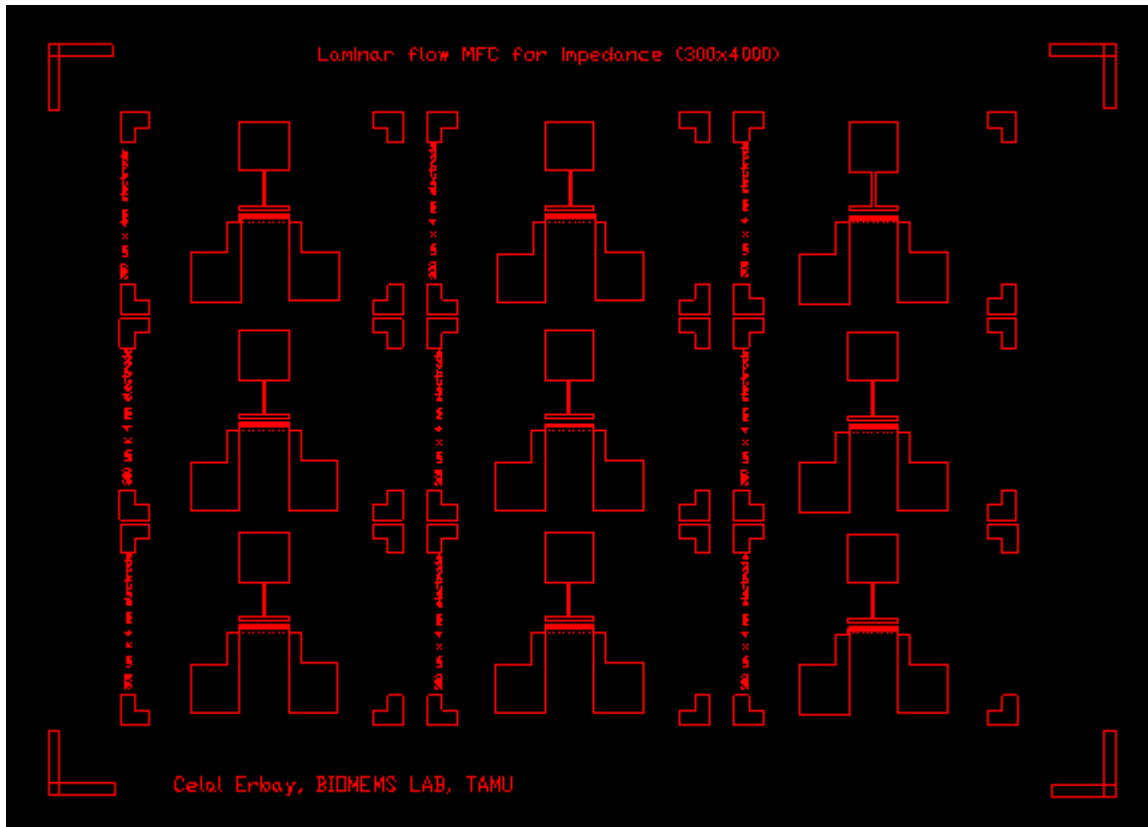
- [143] R. Yuan and D. P. Arnold, "An Input-Powered Vibrational Energy Harvesting Interface Circuit With Zero Standby Power," *IEEE Trans Power Electron*, vol. 26, pp. 3524-3533, 2011.
- [144] L. Woodward, M. Perrier, B. Srinivasan, R. P. Pinto, and B. Tartakovsky, "Comparison of real-time methods for maximizing power output in microbial fuel cells," *AIChE J*, vol. 56, pp. 2742-2750, 2010.
- [145] G. S. Jadhav and M. M. Ghangrekar, "Performance of microbial fuel cell subjected to variation in pH, temperature, external load and substrate concentration," *Bioresour Technol*, vol. 100, pp. 717-723, 2009.
- [146] A. P. Borole, D. Aaron, C. Y. Hamilton, and C. Tsouris, "Understanding Long-Term Changes in Microbial Fuel Cell Performance Using Electrochemical Impedance Spectroscopy," *Energy Environ Sci*, vol. 44, pp. 2740-2745, 2010.
- [147] M. Winter and R. J. Brodd, "What Are Batteries, Fuel Cells, and Supercapacitors?," *Chem Rev*, vol. 104, pp. 4245-4270, 2004.
- [148] Y. Fan, E. Sharbrough, and H. Liu, "Quantification of the Internal Resistance Distribution of Microbial Fuel Cells," *Environ Sci Technol*, vol. 42, pp. 8101-8107, 2008.
- [149] S.-E. Oh and B. Logan, "Proton exchange membrane and electrode surface areas as factors that affect power generation in microbial fuel cells," *Appl Microbiol Biotechnol*, vol. 70, pp. 162-169, 2006.
- [150] P. Aelterman, M. Versichele, M. Marzorati, N. Boon, and W. Verstraete, "Loading rate and external resistance control the electricity generation of

microbial fuel cells with different three-dimensional anodes," *Bioresour Technol*, vol. 99, pp. 8895-8902, 2008.

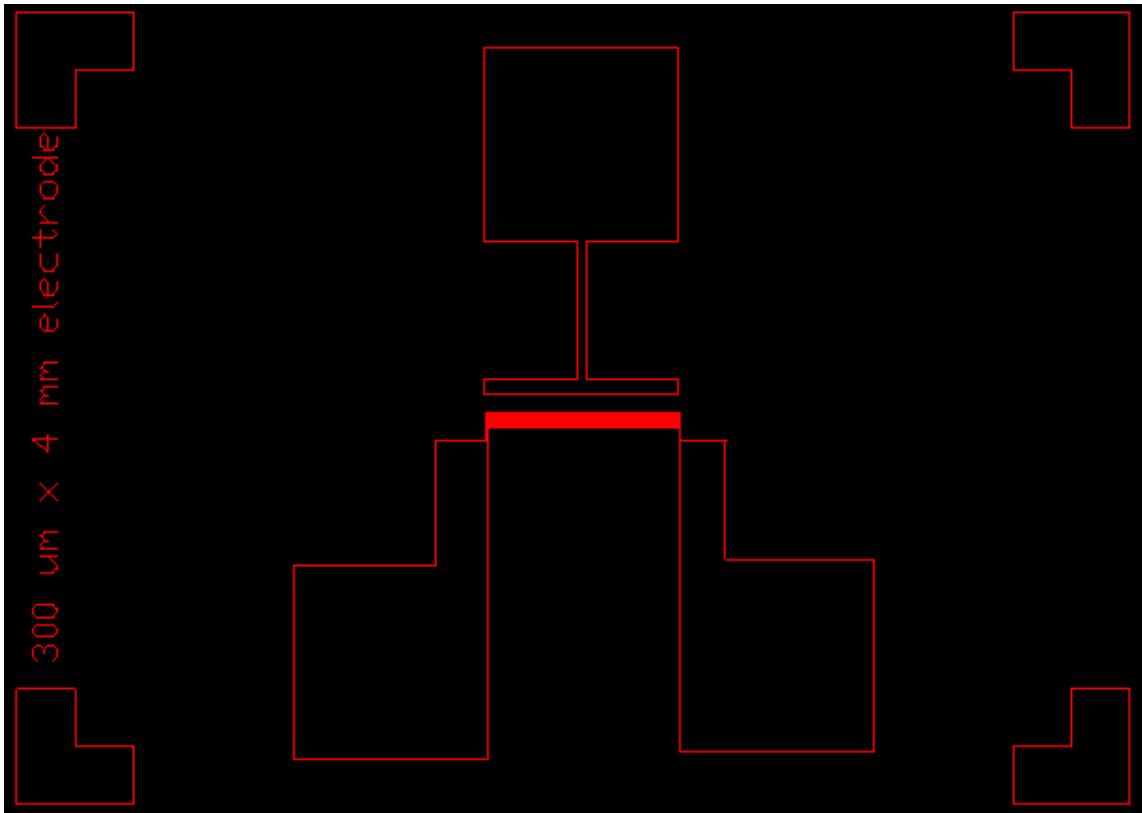
- [151] A. P. Borole, G. Reguera, B. Ringeisen, Z.-W. Wang, Y. Feng, and B. H. Kim, "Electroactive biofilms: Current status and future research needs," *Energy Environ Sci*, vol. 4, pp. 4813-4834, 2011.
- [152] K. P. Katuri, K. Scott, I. M. Head, C. Picioreanu, and T. P. Curtis, "Microbial fuel cells meet with external resistance," *Bioresour Technol*, vol. 102, pp. 2758-2766, 2011.

## APPENDIX A

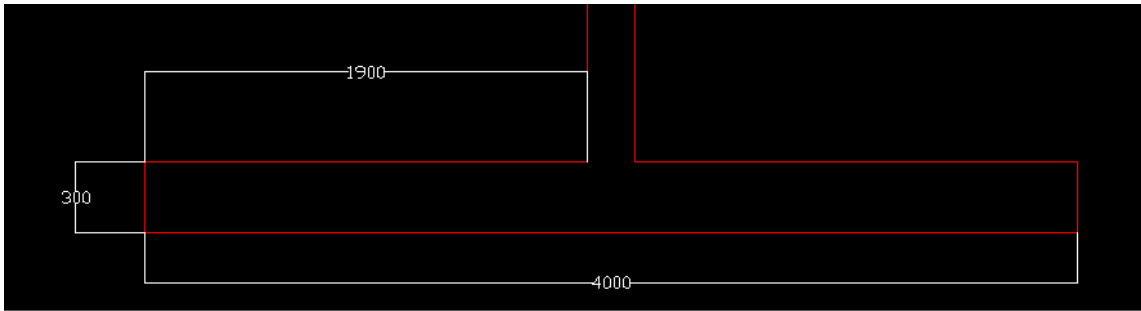
### Film Masks



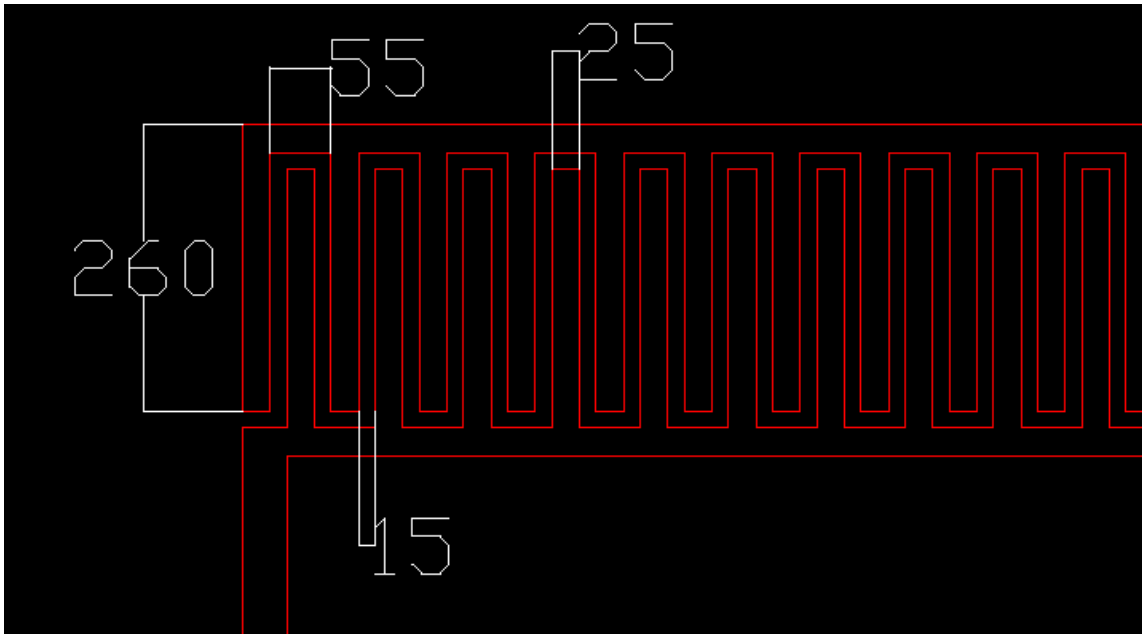
**Figure 1.** Laminar flow MFC microelectrode film mask. 5 x 7.5 cm design includes 9 device.



**Figure 2.** Single laminar flow MFC design.

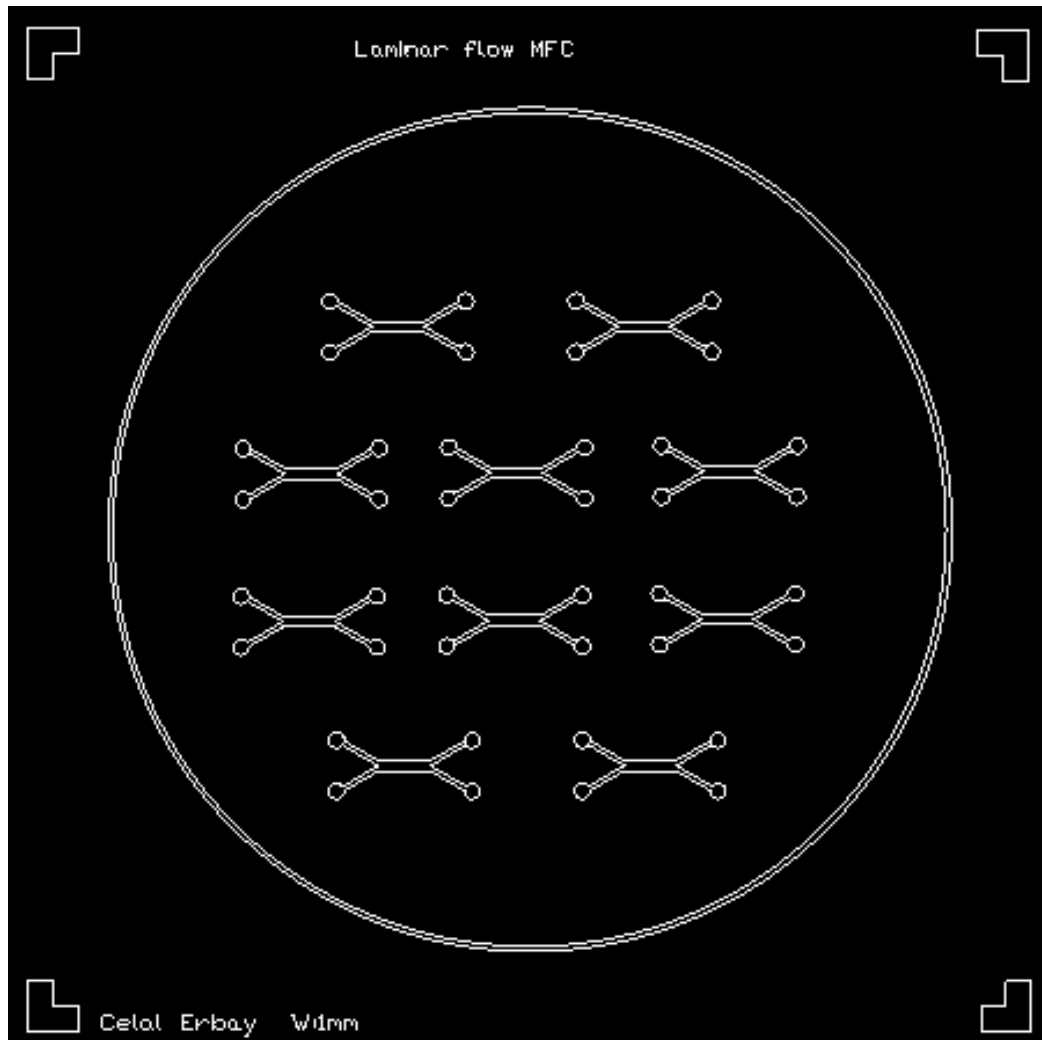


**Figure 3.** Laminar flow MFC cathode design.

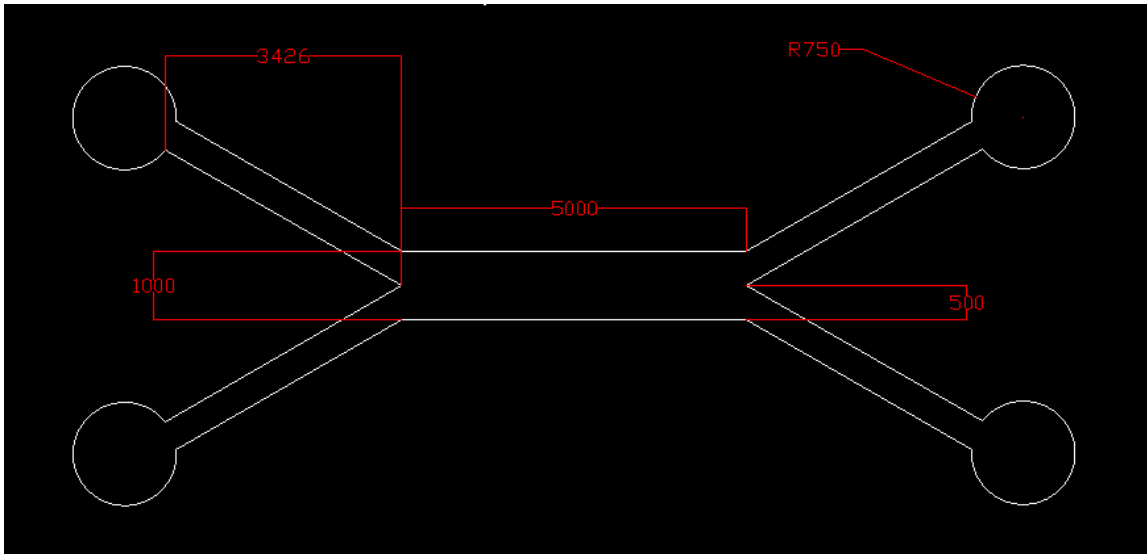


**Figure 4.** Laminar flow MFC interdigitated anode design.





**Figure 5.** Laminar flow MFC microchannel design.



**Figure 6.** Laminar flow MFC single microchannel design.

## **APPENDIX B**

### **Protocols**

#### **1) Priranha cleaning**

- Mix sulfuric acid with hydrogen peroxide (ratio of 3:1)
- Place 5 x 7.5 cm glass slides into mixed solution with Teflon wafer holder
- After keeping inside for 15 min, remove them to clean with DI water
- Dry with N<sub>2</sub> gas

#### **2) Laminar flow MFC electrode fabrication**

- Ti/Au deposition on cleaned glass slides (Ti:20 nm, Au:200 nm)
- Spin coating on deposited glass slide with Shipley 1818 (4000 rpm for 30 seconds with 10 acceleration)
- Soft baking for 10 minute on hot plate (95 °C)
- Exposure (85 mJ) with mask aligner
- Developing for 30 seconds with MF 319
- Au etching for 30 seconds with gold etchant
- Ti etching for 30 seconds with mixture of HF and DI water (ratio of 1:200)
- Photoresist removal with acetone, IPA, DI water and N<sub>2</sub> gas

### **3) Laminar flow MFC microchannel silicon master mold fabrication**

- Clean the wafer with acetone, IPA, DI water and N<sub>2</sub> gas
- Spin coating on wafer with SU-8 2050 (3000 rpm for 30 seconds with 10 acceleration)
- Soft baking for 10 minute on hot plate (65 °C) + 20 minute on hot plate (95 °C)
- Exposure (150 mJ) with mask aligner
- Post exposure baking for 10 minute on hot plate (65 °C) + 20 minute on hot plate (95 °C)
- Developing in Thinner P

### **4) Silicon master mold surface coating**

- Coating PDMS soft-lithography master mold with trichlorosilane (tridecafluoro-1,1,2,2-tetrahydrooctyl) inside a vacuum chamber for 15 min.
- Rinse the coated sample with IPA and dry with N<sub>2</sub> gas.

### **5) Laminar flow MFC PDMS microchannel fabrication**

- Mix PDMS base with curing agent (ratio of 10:1)
- Pour PDMS mixture over the silicon master mold
- Remove bubbles by degassing inside a vacuum chamber
- Place the degassed PDMS into oven (80 °C) for an hour
- Peel of the PDMS that has microchannel structure from silicon master mold

## 6) Preparing bacterial glycerol stocks

- Reagent
  - *Shewanella oneidensis* MR-1
- Equipment:
  - TSA  
(<http://www.sigmaaldrich.com/catalog/product/fluka/22091?lang=en&region=US>)
  - TSB  
(<http://www.sigmaaldrich.com/catalog/product/fluka/22092?lang=en&region=US>)
  - Glycerol  
(<http://www.sigmaaldrich.com/catalog/product/sigma/g5516?lang=en&region=US>)
  - Petridish  
(<http://www.sigmaaldrich.com/catalog/product/sigma/p5606?lang=en&region=US>)
- Pick a single colony of a plate and grow an overnight in the appropriate selectable liquid medium (TSB) (3-5ml).
- Add 0.4 ml of 50% glycerol in H<sub>2</sub>O (100% glycerol is near the weighing balance, add water to it in equal amount, vortex to get 50% glycerol) to a cryogenic vial and autoclave.
- Add 0.8 ml sample from the culture of bacteria to be stored.

- Gently vortex the cryogenic vial to ensure the culture and glycerol is well-mixed.
- Freeze glycerol stock in liquid nitrogen and store in a -80 °C freezer.

### **7) Preparing bacterial culture solution**

- Cells are streaked onto a TSA plate from storage. Then grown in incubator (30 °C) for a day.
- Inoculate the colonies into 5 ml of TSB liquid medium, and then shaken at 180 rpm for 24 h at 30 °C.
- If large amount is needed, inoculate 1 ml of bacterial solution into 100 mL (or desired amount) of TSB liquid medium, and then shaken at 180 rpm for 24 h at 30 °C.
- Adjust the optical densities ( $OD_{600}$ ) to 1 by measuring from cell density meter (or desired) before using.

### **8) Preparing TSB solution**

- Place 15 gram of TSB powder in 1 L flask and add 0.5 L DI water.
- Mix by using magnetic stirrer for 10 min.
- Cover the flask with aluminum foil.
- Autoclave for 15 min at 121 °C.
- After autoclave is over, keep in waterbath to cool it down.

### **9) Preparing TSA plate**

- Place 20 gram of TSA powder in 1 L flask and add 0.5 L DI water.
- Mix by using magnetic stirrer for 10 min.
- Cover the flask with aluminum foil.
- Autoclave for 15 min at 121 °C.
- After autoclave is over, allow the flask to cool in the 50 degree bath for 30 minutes before pouring.
- Pour it gently inside the plates.

## APPENDIX C

### Nutrient/Mineral/Buffer preparation [1]

The NMB solution as an anode growth medium consisted of 10 mL each of Mineral Base I, Mineral Base II, and Nutrient Base stock solution of Table A.1 to 1 L of phosphate buffer solution. This leads to the final concentration as shown in Table A.2.

Table A.1. Nutrient Mineral Buffer (NMB) stock solution

Nutrient and Buffer	Compositions			
Mineral Base I	a. Add the following to 600 mL of distilled water			
	$\text{CoCl}_2 \cdot 6\text{H}_2\text{O}$	0.25 g	$\text{NaMoO}_4 \cdot 2\text{H}_2\text{O}$	0.005 g
	$\text{FeCl}_2 \cdot 4\text{H}_2\text{O}$	2.0 g	$\text{NiCl}_2 \cdot 6\text{H}_2\text{O}$	0.025 g
	$\text{MnCl}_2 \cdot 4\text{H}_2\text{O}$	0.05 g	$\text{NaSeO}_4$	0.025g
	$\text{H}_3\text{BO}_3$	0.05 g	$\text{ZnCl}_2$	0.025 g
	$\text{CuCl}_2$	0.015 g	$\text{NaVO}_3 \cdot 4\text{H}_2\text{O}$	0.005 g
	b. Dilute to 1.0 L (this mixture may form a light precipitate and should be agitated vigorously before transferring)			
Mineral Base II	a. Add the following to 600 mL distilled water			
	$\text{CaCl}_2$	15 g		
	$\text{MgCl}_2 \cdot 6\text{H}_2\text{O}$	20 g		
b. Dilute to 1.0 L				
Nutrient Base	a. Add the following to 600 mL distilled water			
	$\text{NH}_4\text{Cl}$	53 g		
b. Dilute to 1.0 L				
Buffer	a. Add the following to 900 mL distilled water			
	$\text{NaH}_2\text{PO}_4$	6 g		
	b. Titrate to pH 6.99 with monovalent strong base or acid			
c. Dilute to 1.0 L				



Table A.2. Nutrient Mineral Buffer composition in final concentration for anodic microorganism growth medium

Nutrient and Buffer	Compound	Concentration (mg/L)
Mineral Base I	CoCl <sub>2</sub> · 6H <sub>2</sub> O	2.5
	NaMoO <sub>4</sub> · 2H <sub>2</sub> O	0.05
	FeCl <sub>2</sub> · 4H <sub>2</sub> O	20
	NiCl <sub>2</sub> · 6H <sub>2</sub> O	0.25
	MnCl <sub>2</sub> · 4H <sub>2</sub> O	0.5
	NaSeO <sub>4</sub>	0.25
	H <sub>3</sub> BO <sub>3</sub>	0.25
	ZnCl <sub>2</sub>	0.25
	CuCl <sub>2</sub>	0.15
	NaVO <sub>3</sub> · 4H <sub>2</sub> O	0.05
Mineral Base II	CaCl <sub>2</sub>	150
	MgCl <sub>2</sub> · 6H <sub>2</sub> O	200
Nutrient Base	NH <sub>4</sub> Cl	530
Buffer Base	NaH <sub>2</sub> PO <sub>4</sub>	6000

[1] Chae, K.J. et al. Mass Transport through a Proton Exchange Membrane (Nafion) in Microbial Fuel Cells. *Energy Fuels* 22, 169-176 (2008).

Wastewater and NMB solution mix with each other (ratio of 1:5 v) to use as startup solution to grow bacteria on anode in conventional MFCs.